POLITECNICO DI TORINO

Master's Degree Programme in
Energy and Nuclear Engineering

Academic Year 2025/2026









Electromagnetic Interference in Underground Cable–Pipeline Corridors under Earth-Fault Conditions: Analytical and Numerical Assessment of the La Spezia 132 kV Connection

---

Supervisor

Prof. Aldo Canova

Co-supervisors

Prof. Guido Ala, University of Palermo
Eng. Luca Buono, Terna S.p.A.
Eng. Giovanni Filippone, Terna S.p.A.

Candidate

Edoardo Di Liberto

“Great works are performed, not by strength, but perseverance.”
— Samuel Johnson, The History of Rasselas, Prince of Abissinia (1759)

ABSTRACT

The adoption of single-core underground cable systems for electric power transmission is becoming increasingly common, driven by the higher level of public acceptance of underground infrastructure and by the typically faster permitting process compared to overhead transmission lines. Italy's geographical configuration, characterised by a long and predominantly mountainous peninsula, has a direct impact on the planning of energy corridors and on the management of interactions with existing utility infrastructures. Interactions between utility networks shall be considered during the design, installation, and maintenance phases of electrical infrastructure projects. Depending on the nature of the interaction, they may be classified as physical or electromagnetic. Electromagnetic interactions between high- and extra-high-voltage electrical installations and utility networks present a greater degree of analytical and regulatory complexity.

The objective of this thesis is to investigate the electromagnetic interaction phenomena between underground power cable systems and buried pipelines, providing an overview of the underlying physical mechanisms, the applicable regulatory framework, and the mathematical models adopted for the assessment of electromagnetic interference. Attention is devoted to the inductive and conductive coupling phenomena occurring under single-phase-to-earth fault conditions, as well as to the mitigation effects provided by metallic cable screens and earth continuity conductors (ECCs).

Furthermore, the thesis presents a real-case investigation of electromagnetic interference between a 132 kV underground cable system, whose metallic screens are connected in a middle solid bonding arrangement, and two buried natural gas pipelines operating at low- and medium-pressure levels in La Spezia. A sensitivity analysis has been conducted by increasing the number of earth continuity conductors from one to two. The results demonstrate the mitigation of both the inducing current and the fault current injected into the grounding system, leading to a reduction in the interference levels.

The inductive coupling analysis has been performed by means of the open-source software ATP-EMTP and a dedicated computational algorithm developed by the author in GNU Python, implementing the differential equations described in CIGRE Technical Brochure No. 95. Simulation results evidence that induced voltage in case of single phase to ground fault are below the permissible value both for the infrastructure and worker/general-public safety, according to the fault duration. Furthermore, the conductive coupling mechanisms between the pipelines and the cable joint-bay grounding systems have been analysed. The simulation results have showed that the earth potential rises (EPRs) occurring under fault conditions remain within the permissible limits prescribed by the relevant standards.

Future work should incorporate field-verified pipeline and soil data, analyse the permanent network configuration, improve surge-arrester and coating-defect representation, and compare the results with field measurements.

CONTENTS

1. Introduction 1
2. Classification of electromagnetic interference 4
2.1 Conductive interference 4
2.2 Inductive coupling 5
2.3 Capacitive coupling 6
3. Comparison between OHL and UGC coupling in power lines 8
3.1 Coupling in Overhead Lines (OHL) 9
3.2 Coupling in Underground Cable Systems (UGC) 11
4. Underground cable systems: structure, laying configurations and sheath bonding 15
4.1 Structure of Single-Core HV Cables 15
4.2 Laying configurations 18
4.3 Sheath bonding arrangement 20
4.4 Joint bays and earthing systems 27
4.4.1 Typical Joint Bay Configuration 28
4.4.2 Earthing resistance of joint-bay grounding systems 30
4.4.3 Parametric analysis in two-layer soil 31
5. Interfered metallic pipelines and auxiliary systems 36
5.1 Pipeline structure 36
5.2 Cathodic Protection, Measurement Points and Telecontrol Systems 40
5.3 Insulating Joints, Surge Protection Devices and Accessible Parts 40
5.4 Modelling Implications for the Interfered Infrastructure 42
6. Electromagnetic modelling of cable–pipeline systems 45
6.1 Modelling Approach and Distributed-Parameter Representation 45
6.2 Ametani Formulation for Underground Cable Systems 46
6.2.1 Series-Impedance Matrix: Internal and Earth-Return Contributions 46
6.2.2 Potential-Coefficient and Admittance Matrix 48
6.2.3 Mutual Earth-Return Impedance Formulations 49
6.3 Comparison of earth-return impedance formulations 52
6.3.1 Frequency-dependent comparison of Pollaczek, Ametani and Wedepohl formulations 52
6.3.2 Parametric assessment of mutual earth-return impedance formulations 57
7. Regulatory framework and acceptance criteria 62
7.1 General Legislative Requirements 64
7.2 Power-System-Side Standards and Technical References 65
7.3 Pipeline-Side Criteria: Cathodic Protection and AC Corrosion 69
7.4 Limitations of Standard Assessment Criteria 71
7.5 Simplified Screening Calculations for Cable–Pipeline Interference 73
7.5.1 K68-Based Inductive Interference Distance 73
7.5.2 Simplified GPR Assessment with Equivalent Hemispherical Electrode 77
8. ATP-EMTP modelling and analysis of earth-fault interference in the la spezia cable–pipeline corridor 80
8.1 Project framework and analysed configuration 80
8.1.1 Temporary and permanent network configurations 80
8.1.2 Modelled cable–pipeline corridor 82
8.1.3 Analysed fault condition and modelling scope 85

8.2 ATP-EMTP model implementation 86
8.2.1 Upstream-network equivalent 86
8.2.2 Cable system and earthing representation 87
8.2.3 Pipeline route and terminal representation 88
8.3 Influence of the ECC arrangement on fault-current return and pipeline voltage 89
8.3.1 Current definitions and route segmentation 90
8.3.2 Effect of the ECC arrangement on current return and pipeline voltage 91
8.4 Pipeline boundary-condition sensitivity and surge-arrester response 92
8.4.1 Open–Open pipeline-terminal screening 93
8.4.2 Pipeline response after surge-arrester operation 95
8.4.3 Sensitivity to the conducting-state terminal resistance 98
8.5 Touch-voltage and conductive-coupling assessment 99
8.5.1 Touch-voltage assessment of accessible pipeline-connected components 99
8.5.2 Conductive-coupling assessment at the joint bay 100
9. Analytical pipeline–earth modelling and verification using CIGRé technical brochure 95 102
9.1 Method based on Appendix H of CIGRÉ Technical Brochure 95 102
9.1.1 Governing equations of the pipeline–earth circuit 102
9.1.2 Uniform exposure and terminal conditions 103
9.1.3 Extension to non-uniform routes 105
9.2 Numerical implementation of the sectional model 105
9.2.1 Route discretisation and sectional parameters 105
9.2.2 Reconstruction of the distributed induced electromotive force 106
9.2.3 Assembly and solution of the nodal system 107
9.3 Numerical verification against ATP-EMTP 109
9.3.1 Verification Setup and Comparison Criteria 109
9.3.2 Verification Results and Assessment 111
10. Conclusions 113
References 116

LIST OF FIGURES

Figure 4.1: Examples of construction configurations for single-core HV land cables with XLPE insulation, graphically developed in this work based on the technical and constructional data reported in the Prysmian catalogue [39]. 16

Figure 4.2: Schematic representation developed in this work of typical arrangements for single-core HV underground cables: horizontal, triangular and trefoil configurations. 18

Figure 4.3: Typical trench cross-section for an HV underground XLPE cable system in an L-shaped arrangement, showing cable ducts, auxiliary pipes, protection layers, warning tape, backfilling materials and road pavement layers, from an internal Terna technical document [45]. 19

Figure 4.4: Qualitative cross-sectional representation developed in this work of a single-core HV cable, showing the conductor current, the induced longitudinal current in the metallic sheath and the associated magnetic fields. The figure is intended for explanatory purposes; the actual sheath current distribution depends on the bonding arrangement, grounding conditions, cable geometry and surrounding return paths. 21

Figure 4.5: Solid bonding configuration developed in this work for single-core HV cable systems, in which the metallic sheaths are connected together and earthed at both ends of the section. 22

Figure 4.6: Single-point bonding arrangements for single-core HV cable systems: (A) conventional end-point bonding; (B) sectionalised single-point bonding with sheath sectioning insulators and surge arresters. 24

Figure 4.7: Cross-bonding configurations developed in this work for single-core HV cable systems: (A) cross-bonded system without cable transposition, typically associated with compact arrangements; (B) cross-bonded system with cable transposition, where the phase cables are physically transposed and the metallic sheaths are cross-connected through link boxes to balance the induced sheath voltages. 26

Figure 4.8: Field view of an HV underground-cable joint bay during installation, showing the incoming and outgoing single-core cables and the prepared jointing area [49]. 28

Figure 4.9: Typical cable-sheath link-box configurations used in HV cable systems: (A) cross-bonding link box, (B) single-point-bonding link box, and (C) link box equipped with three surge arresters connected between the cable sheaths and earth for overvoltage protection [50], [51]. 29

Figure 4.10: Simplified CAD layout developed in this work for the reference 150 kV joint-bay grounding system, showing the buried perimeter conductor and the vertical earth electrodes. 29

Figure 4.11: Grounding resistance Rg computed in this work for the reference 150 kV joint-bay grounding system as a function of the upper-layer resistivity $\rho 1$and lower-layer resistivity $\rho 2$in a two-layer soil model. Results are reported for two representative upper-layer thicknesses ($h = 0.5$ m and $h = 2$m). 32

Figure 4.12: Design chart computed in this work for the reference 150 kV joint-bay grounding system. Grounding resistance Rg is plotted as a function of the soil resistivity ratio $\rho 2/\rho 1$ for different upper-layer thicknesses h, assuming $\rho 1 = 100\ \Omega m$. 33

Figure 5.1: Indicative geographical distribution of effective ground conductivity classes in Italy, extracted and graphically adapted in this work from ITU-R P.832-3 [61]. Conductivity values are expressed in mS/m. 38

Figure 5.2: Schematic representation developed in this work of an interfered pipeline including insulating joints, surge arresters (SAs), cathodic protection system, grounding connections, accessible parts and a coating defect. The figure also highlights possible current return paths through the soil and the interaction between the pipeline and the surrounding environment under interference conditions. 41

Figure 5.3: Distributed-parameter equivalent model developed in this work for an interfered buried pipeline including coating-to-ground coupling, insulating joints and localized coating defects. 43

Figure 6.1: Geometrical definition developed in this work for two buried conductors, showing the burial depths hi and hj, the horizontal separation xij, and the direct distance dij. 50

Figure 6.2: Relative error of the equivalent inductive component of the mutual earth-return impedance, computed in this work with respect to the Pollaczek reference formulation. 54

Figure 6.3: Relative error of the resistive component of the mutual earth-return impedance, computed in this work with respect to the Pollaczek reference formulation. 54

Figure 6.4: Mutual earth-return impedance versus horizontal separation for different soil resistivity values, developed in this work. Pollaczek, Ametani/ATP and Wedepohl formulations are compared. 56

Figure 6.5: Relative error of the mutual impedance magnitude $Z0ij$ with respect to the Pollaczek reference for the considered formulations, developed in this work. The colour scale is logarithmic to improve the readability of both low- and high-error regions. 60

Figure 7.1: K.68-inspired inductive screening chart obtained in this work using the compact Wedepohl approximation for the mutual earth-return impedance. The black curves represent constant values of the normalised induced voltage, while the red dashed curve indicates the formal validity limit of the approximation. 75

Figure 7.2: K.68-inspired inductive screening chart obtained in this work using the complete Pollaczek formulation for the mutual earth-return impedance. The chart relates soil resistivity, horizontal cable–pipeline separation and normalised induced voltage. 75

Figure 7.3: Simplified GPR screening chart obtained in this work using the equivalent hemispherical-electrode model and the admissible voltage limits derived from CEI EN 50443 [4]. 78

Figure 8.1: Schematic comparison developed in this work of the first and second temporary configurations of the 132 kV connection serving the La Spezia port area. 81

Figure 8.2: Field view of the SCRI forming the mobile user substation in the analysed temporary configuration of the 132 kV connection serving the La Spezia port area [73]. 82

Figure 8.3: Schematic representation developed in this work of the representative TOC installation arrangement with the documented ECC1 and the candidate ECC2. 84

Figure 8.4: Maximum terminal pipeline-to-earth voltages under the Open–Open condition as functions of the sending- and ending-side continuation lengths. Green annotations identify terminals at which the $70\ VRMS$ operating threshold is exceeded; red annotations indicate that no arrester operation is required. 94

Figure 8.5: Envelope of the longitudinal pipeline-to-earth voltage profiles under the Open–Open condition, together with the governing profile for each pipeline. 94

Figure 8.6: Maximum longitudinal pipeline-to-earth voltages in the intermediate state, where present, and in the final state after all required surge-arrester operations. Green annotations identify the required or active arrester condition, while red annotations indicate that no operation occurs. The equal-length LP cases pass directly to the final state with both arresters conducting. All panels use the same voltage scale. 96

Figure 8.7: Longitudinal pipeline-to-earth voltage profiles for the governing final configuration under the Open–Open condition, after the first arrester operation and after operation of both terminal arresters. 97

Figure 9.1: Pipeline-to-earth voltage-magnitude profiles calculated using the complete Appendix H model for the CC, CO and GC terminal configurations: (a) LP pipeline and (b) MP pipeline. The same distributed induced-electromotive-force profile is applied in all three cases, and the longitudinal coordinate is normalised over the reconstructed interference zone. 109

LIST OF TABLES

Table 3.1: Order-of-magnitude comparison compiled in this work of the characteristic distance between phase conductors and metallic return or shielding paths in representative Terna OHL and UGC configurations [27], [28], [29], [30], [31]. 12

Table 3.2: Indicative reduction factors for typical overhead-line and underground-cable configurations at power frequency, summarised in this work from the indicative ranges reported in EN 50522 Annex I. EN 60909-3 is used as a methodological reference for calculating reduction factors [8], [20]..... 13

Table 4.1: Typical conductor cross-sections used in Terna high-voltage underground cable systems according to the voltage level and conductor material. The listed values refer to nominal conductor cross-sections commonly adopted in transmission applications. For 380 kV systems, different cable designs may be available for the same nominal conductor cross-section (2000 mm² and 2500 mm²) [40], [41], [42]..... 17

Table 4.2: Geometrical characteristics adopted in this work for the reference 150 kV joint-bay grounding system. 30

Table 4.3: Validation performance metrics obtained in this work for the proposed double soft-transition interpolation model. 35

Table 5.1: Conversion performed in this work of the effective ground-conductivity classes reported for Italy in ITU-R P.832-3 into equivalent resistivity values [61]. 39

Table 5.2: Representative pipeline, coating and geometrical parameters used for electromagnetic interference modelling [55], [56], [59]. 39

Table 5.3: Elements of the interfered infrastructure relevant to electromagnetic interference modelling. 44

Table 6.1: Input parameters adopted for the mutual earth-return impedance verification. 53

Table 6.2: Summary of the relative errors computed in this work for the mutual earth-return impedance verification. Negative values indicate an underestimation with respect to the Pollaczek reference. 55

Table 6.3: Input data adopted for the comparison of mutual earth-return impedance formulations. 57

Table 6.4: Summary of the relative errors of the considered formulations with respect to the Pollaczek reference for the mutual impedance magnitude $Z0ij$. 59

Table 7.1: Main legislative, regulatory, and technical references for the assessment of electromagnetic interference between AC power systems and buried metallic pipelines. 63

Table 7.2: Main legislative and installation requirements concerning the coexistence of underground cable systems and buried infrastructures, with particular reference to minimum separation distances, crossings, and installation conditions. 65

Table 7.3: Pipe-to-soil voltage limits under fault conditions as a function of fault duration, adopted in this work for personnel safety assessment and based on CEI EN 50443 [4]..... 66

Table 7.4: Main operational checks from the power-system perspective for the assessment of electromagnetic interference. 67

Table 7.5: Main operational checks from the pipeline perspective for cathodic protection and AC corrosion assessment. 70

Table 7.6: Main applicability and interpretation limitations of the criteria adopted for AC corrosion assessment. 72

Table 7.7: Error of the Wedepohl compact approximation with respect to the Pollaczek reference formulation outside the formal validity range..... 76

Table 8.1: Main characteristics of the modelled underground cable system. 83

Table 8.2: Main characteristics of the metallic pipelines included in the electromagnetic model. 85

Table 8.3: Fault condition and numerical settings adopted in the ATP-EMTP simulations. 86

Table 8.4: Equivalent earthing connections adopted in the ATP-EMTP model of the second temporary configuration. . 88

Table 8.5: Phase-current sum, total ECC return current and residual inducing current in the two cable sections for the one- and two-ECC configurations under the representative L2-to-earth fault. 91

Table 8.6: Maximum pipeline-to-earth voltages for the LP and MP pipelines for the one- and two-ECC configurations under the representative L2-to-earth fault..... 92

Table 8.7: Sensitivity of the maximum pipeline-to-earth voltages to the equivalent conducting-state resistance for the governing final-state configuration $LS = 2000\ m$, $LE = 0$ m. 98

Table 8.8: Touch-voltage assessment of accessible metallic components connected to the MP pipeline. 99

Table 8.9: Conductive-coupling assessment between the joint-bay earthing system and the MP pipeline. 100

Table 9.1: Equivalent series components used in ATP-EMTP to reproduce the characteristic impedance Zc at 50 Hz. 110

Table 9.2: Numerical verification of the Appendix H implementation against ATP-EMTP for the CC, CO and GC terminal configurations. 111

1. INTRODUCTION

The development of modern power systems increasingly requires electrical infrastructure to coexist with gas pipelines and other buried utilities within the same urban and industrial corridors. High-voltage underground cables reduce visual impact and facilitate installation in areas subject to territorial constraints, but their burial does not eliminate electromagnetic interaction with nearby metallic structures. These interactions must be assessed to protect personnel, preserve pipeline integrity and ensure the operational continuity of both infrastructures [1], [2].

In underground cable systems equipped with metallic screens, the electric field is largely confined within the cable structure by the insulation and metallic screens, while the surrounding soil further contributes to field attenuation, leading to negligible external electric field exposure. Capacitive coupling with directly buried pipelines is, therefore, generally secondary. The main mechanisms are inductive coupling, produced by the magnetic field associated with the conductor and return currents, and conductive coupling, caused by fault current injected into the soil through the earthing systems of cable joints. Single-phase-to-earth faults are particularly relevant because the resulting unbalanced current may return through cable screens, earth-continuity conductors, earthing systems and the soil, producing both longitudinal pipeline voltages and local earth-potential rise [3], [4].

The pipeline response depends not only on the fault current and cable–pipeline separation, but also on the complete electrical configuration of the corridor. Cable layout, screen bonding, earth-continuity conductors, joint-bay earthing systems, coating and terminal conditions of pipeline determine the distribution of current and voltage along the two infrastructures. Insulating joints, cathodic-protection systems and surge arresters may introduce discontinuities or alternative paths to earth and must therefore be considered when defining the pipeline boundary conditions [3].

This thesis develops an integrated framework for assessing electromagnetic interference between high-voltage underground cable systems and buried metallic gas pipelines. The work combines the physical description of the coupling mechanisms, the applicable regulatory criteria, analytical earth-return formulations, simplified screening methods and detailed numerical models. The principal objective is to determine how fault-current return paths, earthing systems and pipeline terminal conditions affect the induced pipeline voltage and the associated safety assessment. Steady-state interference, cathodic protection and AC-corrosion criteria are included in the general framework, whereas the detailed case study focuses on the more severe power-frequency earth-fault condition.

The modelling framework is developed progressively. The mutual earth-return impedance is examined using Pollaczek's formulation as the analytical reference and comparing it with the

Ametani/ATP [5], Wedepohl [6], CIGRE [3] and ITU-T K.68 [7] approximations. This comparison establishes the accuracy and applicability of the formulations used in the subsequent calculations. Supporting analyses are also developed for joint-bay earthing systems in homogeneous and two-layer soils and for preliminary screening of inductive and conductive interference. These tools provide order-of-magnitude assessments before construction of the complete distributed model.

The numerical application concerns the second temporary configuration of the 132 kV underground connection serving the La Spezia port area and two nearby low- and medium-pressure gas pipelines. A sectional ATP-EMTP model reproduces the phase conductors, metallic screens, earth-continuity conductors, earthing systems, non-uniform cable–pipeline geometry and pipeline terminal conditions. The reference condition is an single phase to ground fault at the Mobile User Substation. The documented one-ECC arrangement is compared with a candidate two-ECC solution, after which the analysis evaluates the influence of the unknown external pipeline boundary, the successive operation of terminal surge arresters and their equivalent conducting-state resistance. Touch-voltage and conductive-coupling checks are performed separately using the applicable CEI EN 50443 and CEI EN 50522 criteria [4], [8].

The results show that the second ECC provides an effective additional metallic return path. It reduces the residual inducing current by approximately 28% and the maximum pipeline-to-earth voltages by 26–29% for the analysed boundary conditions. The pipeline response is strongly affected by terminal conditions before surge-arrester operation, whereas the operated arresters substantially reduce its sensitivity to the assumed continuation lengths. The touch-voltage and conductive-coupling assessments are satisfied under conservative assumptions.

An independent frequency-domain model based on Appendix H of CIGRE Technical Brochure No. 95 is finally applied to the same non-uniform pipeline routes [3]. The conductor-current phasors obtained from ATP-EMTP are used to reconstruct the distributed induced electromotive force and solve the pipeline–earth circuit analytically. Comparison with ATP-EMTP gives a maximum normalised error of 0.24%, supporting the adopted sectional implementation. For the investigated route and coating properties, including the coating conductance changes the maximum voltages by less than approximately 0.30%.

The thesis is organised as follows. Chapters 2 and 3 introduce the coupling mechanisms and compare the electromagnetic behaviour of overhead lines and underground cable systems. Chapters 4 and 5 describe the cable, earthing and pipeline components required for interference modelling. Chapter 6 develops and compares the earth-return impedance formulations. Chapter 7 presents the regulatory framework, acceptance criteria and simplified screening methods. Chapter 8 develops the ATP-EMTP model and applies it to the La Spezia case study. Chapter 9 presents the CIGRE Appendix

H sectional model and its verification against ATP-EMTP. Chapter 10 summarises the main conclusions.

2. CLASSIFICATION OF ELECTROMAGNETIC INTERFERENCE

After introducing the general framework of the problem, it is useful to distinguish the main physical mechanisms through which an AC power system can interfere with a nearby metallic structure. In electrical transmission systems, electromagnetic interference phenomena can generally be classified into three main categories: conductive (galvanic) coupling, inductive coupling and capacitive coupling [1].

This classification makes it possible to separate physically different phenomena that may nevertheless coexist within the same real configuration. In the case of power lines and buried metallic pipelines, inductive coupling is generally the dominant mechanism along parallel exposure sections, whereas conductive coupling becomes particularly significant near locations where current is dispersed into the ground. Capacitive coupling, on the other hand, is usually of secondary importance for directly buried metallic pipelines, although it remains relevant for a complete physical interpretation of the interference phenomenon [9].

2.1 Conductive interference

Conductive interference occurs when a direct current transfer exists between the electrical system and the interfered structure through the soil, which acts both as a common conductive medium and as the return path for fault current. This phenomenon becomes particularly significant under fault conditions, when high currents dispersed into the ground generate substantial potential gradients. These gradients may cause ground potential rise (GPR), circulating currents in nearby metallic pipelines, hazardous touch and step voltages and, in some cases, accelerated corrosion phenomena in buried infrastructures. Unlike electromagnetic coupling mechanisms in the strict sense, in conductive interference the fault current returns to the source involving the buried metallic structures themselves [1], [2].

From a modelling perspective, this phenomenon is generally represented through network models that include grounding impedances and the distribution of return currents in the soil.

In interference studies involving power lines and nearby metallic infrastructures, conductive coupling becomes particularly important under earth-fault conditions and is typically evaluated together with inductive coupling effects.

2.2 Inductive coupling

Inductive coupling originates from the time-varying magnetic field generated by the currents flowing in the interfering line. According to the Faraday–Neumann–Lenz law, this magnetic field links nearby metallic circuits and induces an electromotive force proportional to the time variation of the magnetic flux linkage:

$$e = -\frac{d\lambda}{dt} \tag{2.1}$$

where:

- e is the induced electromotive force [V];
- λ is the flux linkage [Wb];
- t is time [s].

Since the flux linkage can be expressed as:

$$\lambda = MI \tag{2.2}$$

where:

- M is the mutual inductance between the source and the target system [H];
- I is the current flowing in the disturbing source [A];

assuming a constant mutual inductance, the induced voltage becomes:

$$e = -M\frac{dI}{dt} \tag{2.3}$$

The induced voltage therefore depends both on the time variation of the source current and on the magnetic coupling between the infrastructures. The coupling level is influenced by system geometry, separation distance between the power line and the pipeline, parallel exposure length, phase arrangement and the characteristics of the current return path through the soil [9], [10].

From a modelling perspective, inductive coupling is commonly represented through distributed-parameter models or equivalent circuits based on self and mutual impedances. Within these formulations, the soil is not merely the physical medium separating the infrastructures, but an active part of the return-current path contributing directly to the longitudinal and mutual impedances of the system. Carson's and Pollaczek's formulations constitute the classical theoretical framework for describing earth-return currents and the resulting electromagnetic coupling between parallel conductors [10].

In a more general circuit representation, the magnetic coupling between the interfering system and the buried metallic structure is described through self and mutual impedances per unit length. The induced longitudinal voltage along the pipeline can therefore be expressed as:

$$\frac{dV_{ind}}{dx} = Z_m I \tag{2.4}$$

where:

- V_{ind} is the induced longitudinal voltage on the pipeline [V];
- x is the longitudinal coordinate along the pipeline route [m];
- Z_m is the distributed mutual impedance between the interfering conductor and the pipeline [Ω/m];
- I is the current flowing in the interfering conductor [A].

The term Z_m accounts for both conductor geometry and the earth-return path. Within this framework, Carson's and Pollaczek's formulations provide the basis for evaluating earth-return impedances, while later developments, including those proposed by Ametani, extend the formulation to more general overhead and underground conductor systems. These approaches are particularly relevant for underground cable–pipeline interference studies, where the soil, metallic sheaths, earth continuity conductors and the pipeline itself must be represented as mutually coupled conductors rather than isolated elements [11], [12].

Under earth-fault conditions, and especially during single line-to-earth faults, the current becomes both high and strongly unbalanced. As a consequence, inductive coupling may increase significantly and often represent the dominant contribution in the estimation of induced voltages on buried metallic pipelines [1], [2].

2.3 Capacitive coupling

Capacitive, or electrostatic, coupling is associated with the electric field produced by the voltage of the line conductors. This field induces a charge distribution on nearby metallic structures and therefore affects their electric potential. In this mechanism, the interfered structure interacts with the conductor system through distributed mutual capacitances, acquiring induced charges and a voltage that depend on the overall geometrical configuration of the system [13].

The magnitude of capacitive coupling mainly depends on the voltage level of the electrical system, conductor geometry, lateral separation between the line and the interfered infrastructure, the position of the pipeline with respect to the ground, phase arrangement and the presence of any earth wires or shielding elements [14], [15].

Although capacitive coupling is generally less critical than inductive coupling in fault-condition interference studies, it may still be relevant under steady-state operating conditions and is required for a complete physical description of the electromagnetic interaction between coexisting infrastructures [13], [14], [15]. However, in the case of buried pipelines, the capacitive effect is usually attenuated by the surrounding soil, which acts as an electric-field shielding medium. As a result, this contribution is generally secondary compared with inductive coupling, especially in fault-condition analyses [16].

3. COMPARISON BETWEEN OHL AND UGC COUPLING IN POWER LINES

Electromagnetic interference generated by high- and extra-high-voltage systems can be classified as follows:

- Inductive coupling, related to longitudinal currents;
- Capacitive coupling (or electrostatic coupling), related to displacement currents;
- Conductive coupling, related to transverse currents.

The severity of the disturbance depends on the operating conditions of the electrical system; in particular, the stresses of the interfering system are generally:

- short-duration and high-intensity under fault conditions;
- long-duration and low-intensity under normal operating conditions.

In general, the former can pose a danger to people and/or cause damage to infrastructure, while the latter can lead to long-term degradation of the infrastructure (e.g., pipe corrosion).

Furthermore, at power frequency, capacitive coupling is significant mainly when both the source and the interfered system are installed in air. In underground configurations, the presence of a lossy conductive earth provides a strong shielding effect, so that capacitive coupling is generally neglected in underground cable systems. Conductive coupling is present in both overhead lines and underground cables; the phenomenon is related to earth currents flowing through the grounding systems of overhead line towers or cable joints [2].

The electromagnetic behaviour of power lines is strongly influenced by the physical configuration of the interfering system. Overhead lines and underground cable systems have different geometrical and electrical characteristics, which affect the coupling mechanisms towards nearby metallic infrastructures.

The following sections therefore analyse the main differences between OHL and UGC systems for the assessment of electromagnetic interference towards buried metallic utilities.

3.1 Coupling in Overhead Lines (OHL)

Overhead transmission lines represent a source of electromagnetic interference in which both capacitive coupling, associated with the electric field produced by energized conductors, and inductive coupling, associated with the magnetic field generated by load or fault currents, may coexist [2].

This dual behaviour distinguishes overhead lines from underground cable systems, where capacitive coupling with external metallic infrastructures is generally neglected. From an equivalent-circuit perspective, the lossy conductive soil introduces a finite conductance in parallel with the mutual capacitance that would otherwise exist between buried conductors. This conductive path strongly shunts the capacitive branch, making capacitive coupling negligible at power frequency. This differs from overhead-line systems, where air behaves as an insulating medium and mutual capacitances between energized conductors and nearby metallic structures may remain relevant. In addition, the electric field generated by the cable core is largely confined within the cable insulation and terminated on the metallic screen or sheath, which is normally bonded to earth. Consequently, electromagnetic interference from underground cable systems is mainly governed by inductive and conductive coupling mechanisms.

Capacitive coupling in overhead lines originates from the electric field generated by the phase conductors. In the presence of nearby metallic structures, the line conductors and the interfered structure form a system of distributed mutual capacitances, through which induced charges and potentials may arise. This phenomenon mainly depends on the system voltage, conductor geometry, lateral separation, the position of the interfered structure with respect to the ground, and the presence of earth wires or shielding elements [13], [14], [15]. For directly buried pipelines, however, the soil tends to attenuate the electric field, making capacitive coupling generally less critical than magnetic coupling, especially under fault conditions [17], [18].

Inductive coupling is instead associated with the magnetic field produced by currents flowing in the phase conductors. The time-varying magnetic flux may link with nearby metallic structures, inducing a longitudinal electromotive force and, consequently, distributed voltages along the pipeline. The magnitude of this phenomenon depends on the line current, the length of parallel exposure, the separation distance, the relative geometry between the source and the interfered infrastructure, and the characteristics of the current return path through the soil [1], [10], [18], [19].

In overhead lines, earth wires are installed at the top of the towers and connected to the tower grounding system; they can be subjected to induced voltages and currents due to inductive coupling with the phase conductors. These currents can generate a magnetic field partially opposite to that produced by the phase conductors, thereby contributing to the reduction of the resulting magnetic

field. This effect can be interpreted through the concept of reduction factor, which is related to the inductive coupling between earth wires and phase conductor, including the earth return path. Such distribution depends on the self-impedances of the earth wires and on the mutual impedances with the phase conductors and earth wires [8], [20].

However, in OHL systems the effectiveness of this compensation is limited by the geometry of the line. The distance between the phase conductors and the earth wires is relatively large and tends to increase with the voltage level, since larger insulation clearances must be guaranteed. As a result, the mutual impedances between phase conductors and earth wires are generally less favourable than in underground cable systems, where the metallic screen is much closer to the core conductor [8], [20]. Conductive coupling may also arise in overhead transmission systems due to the earthing systems of the towers. Under asymmetrical fault conditions, and particularly during single line-to-earth faults, part of the fault current is dispersed into the soil through the tower grounding systems, producing a local ground potential rise. This phenomenon may generate transferred potentials and conductive interference towards nearby infrastructures [4], [8].

For buried metallic utilities, such as pipelines or grounding systems of nearby installations, conductive coupling is associated with the current exchanged through the surrounding soil and with the resulting pipe-to-soil potential rise. For above-ground or electrically isolated metallic infrastructures, the ground potential rise may instead produce dielectric stresses and hazardous touch voltages [4], [8].

In overhead transmission lines, due to the lower shielding effectiveness of overhead earth wires compared with cable metallic screens or earth continuity conductors, a significant portion of the single line-to-earth fault current may return through the soil. Consequently, the currents dispersed by tower grounding systems may reach values of the order of kiloamperes under fault conditions [8], [20].

Under earth-fault conditions, and particularly in the case of a single line-to-earth fault, inductive coupling may become the dominant contribution for nearby metallic infrastructures.

The strongly unbalanced fault current returns through the soil, earth wires, tower earthing systems, and other available conductive paths. This may increase both the longitudinal induced voltages and the local transferred potentials on the pipeline, especially along parallel sections or close to points where the fault current is dispersed into the ground [18], [21].

Therefore, when assessing interference from an overhead line, the phase conductors alone are not sufficient to describe the source of interference. Under fault conditions, the return-current paths must also be represented, including overhead earth wires, tower earthing systems and the soil. These elements influence both the magnetic field associated with inductive coupling and the ground potential rise associated with conductive coupling [8], [18], [20], [21].

3.2 Coupling in Underground Cable Systems (UGC)

Compared with overhead lines, underground cable systems exhibit a different electromagnetic behaviour, mainly due to their compact geometry and to the presence of metallic screens. As discussed, underground cables can induce voltage and currents on interfered infrastructure due to only inductive and conductive couplings; capacitive coupling is assumed to be negligible due to the shielding effects of conductive losses earth [22], [23], [24], [25].

Interference towards nearby metallic utilities is therefore mainly governed by the magnetic field generated by the currents flowing in the phase conductors (i.e. core circuits) and by the associated return paths (i.e. metallic screen or earth continuity conductors). Unlike overhead lines, where earth wires are located at a significant distance from the phase conductors, in underground cable metallic screen or earth continuity conductors (ECCs) are much closer to the core conductors. Consequently, higher induced voltage and currents are expected if compared to overhead line earth wires, both in normal operation and fault condition [18], [23], [24], [25].

The currents flowing through the metallic screen or through an ECC are opposite to the phase-conductor current and generate a partially compensating magnetic field, thereby reducing the residual external magnetic field. This compensation is strongly affected by the geometrical distance between the main current path and the metallic return path. In underground cables, the metallic screen is located only a few centimetres from the core conductor, whereas in overhead lines the distance between the phase conductors and the overhead earth wires may reach several metres or even tens of metres, especially at the highest voltage levels [8], [20], [26].

The geometrical separation between the main current path and the metallic return or shielding path is markedly different in overhead lines and underground cable systems. Typical engineering orders of magnitude are summarised in Table 3.1.

Table 3.1: Order-of-magnitude comparison compiled in this work of the characteristic distance between phase conductors and metallic return or shielding paths in representative Terna OHL and UGC configurations [27], [28], [29], [30], [31].

System	132–150 kV	220 kV	380 kV
OHL, characteristic separation between earth wire and nearest phase conductor	~ 4.4[1] – 5.7[2] m	~ 5.9[2] m	~ 5.5[1] m
UGC, characteristic spacing between core and metallic screen/sheath	~ 18 – 25 mm	~ 22 – 30 mm	~ 25 – 35 mm

Notes: [1] Sostegno tipo N a semplice terna a delta tiro pieno (132–150 kV) and sostegno tipo N a semplice terna trinato (380 kV). [2] Sostegno tipo N a semplice terna tiro pieno (132–150 kV) and sostegno tipo N a semplice terna (220 kV). The original Terna terminology is retained. OHL values refer to representative Terna support configurations and are intended only for order-of-magnitude comparison.

When the bonding arrangement of the metallic screens does not allow a significant return current to flow along the sheath, earth continuity conductors may play a more relevant role in defining the return-current paths. As metallic conductors laid in parallel with the cable system, they can contribute to reducing the residual magnetic field and, therefore, to mitigating the coupling towards nearby metallic infrastructures. Their presence, position and number must therefore be considered as modelling parameters in the assessment of interference [8], [20], [32], [33].

The geometrical arrangement of the phases remains important, especially under normal operating conditions. Compact configurations, such as trefoil laying, favour the mutual compensation of the magnetic fields generated by the three phases, whereas more open arrangements may result in a higher residual external magnetic field. Under single line-to-earth fault conditions, however, the effect of the laying configuration may become less significant than the fault current itself and the distribution of the return-current paths, while still remaining a geometrical parameter of the model [8], [22], [24].

From a circuital point of view, the shielding effect of metallic return paths can be interpreted through the distribution of current between the phase conductor, metallic screens, soil, and possible earth continuity conductors. The portion of current flowing through metallic screens or ECCs depends on the self-impedances of those paths and on the mutual impedances with the phase conductor. For this reason, the shielding contribution of metallic screens and earthing conductors can be described through the concept of reduction factor, which is recalled in standards dealing with earthing systems and partial short-circuit currents, such as CEI EN 50522 and CEI EN 60909-3 [8], [20].

The reduction factor provides a compact indication of the portion of fault current that effectively returns through the soil. Typical indicative values for overhead-line and underground-cable configurations are reported in Table 3.2.

Table 3.2: Indicative reduction factors for typical overhead-line and underground-cable configurations at power frequency, summarised in this work from the indicative ranges reported in EN 50522 Annex I. EN 60909-3 is used as a methodological reference for calculating reduction factors [8], [20].

System type	Typical configuration	Indicative reduction factor
OHL	One steel earth wire	0.80 – 0.98
	One ACSR/AACSR earth wire	0.55 – 0.85
	Two AACSR earth wires	0.50 – 0.80
UGC	Single-core XLPE cable with Cu screen, small cross-section	0.50 – 0.60
	Single-core XLPE cable with Cu screen, larger cross-section	≈ 0.32
	Single-core XLPE cable with high-cross-section Pb sheath	≈ 0.20
	Oil-filled cable with high-cross-section Al sheath	≈ 0.01 – 0.05

The values in Table 3.2 are indicative and should not be used as fixed design values. The actual reduction factor depends on conductor geometry, bonding arrangement, soil resistivity, earthing conditions and the electrical characteristics of the metallic return paths. A more accurate evaluation therefore requires the specific calculation procedures described in EN 60909-3 for the considered line or cable configuration [8], [20].

The electromagnetic response of an underground cable system therefore depends not only on the current flowing in the phase conductors, but also on the way in which the metallic screens are bonded and connected to earth. Depending on the bonding arrangement, the screens may carry circulating currents under normal operation, develop induced voltages to earth, or provide part of the return path under fault conditions. Link boxes, used to arrange the bonding connections of cable sheaths, and surge arresters, installed to limit sheath overvoltages, are therefore part of the electrical behaviour of the system rather than only accessory components. For the same reason, earth continuity conductors must also be included in the model when they are present, since they can affect the external magnetic field and the resulting interference towards the pipeline [34], [35], [36].

In underground cable systems, conductive coupling is mainly associated with the earthing points of the cable system, especially at major sections, where metallic screens or ECCs are connected to local earthing systems. These earthing systems are typically designed as local earth electrodes and may disperse part of the fault current into the surrounding soil during asymmetrical fault conditions. Compared with overhead lines, however, a large portion of the fault current is recalled by the metallic screens and/or ECCs, so that the current dispersed by the earthing systems of major sections is generally much lower than that dispersed by tower earthing systems. In practical cases, these dispersed currents are often of the order of hundreds of amperes rather than kiloamperes.

The evaluation of longitudinal currents in the cable core, metallic screen and ECC, as well as transverse currents in the earthing system, therefore requires a detailed electromagnetic model of the three-phase single-core cable system. Depending on the level of detail allowed by the available data, the laying configuration, bonding arrangement, earthing points, possible earth continuity conductors and soil properties should also be included. These elements affect the magnitude of inductive and conductive coupling with parallel metallic pipelines [18], [23], [24], [32], [33].

The resulting distribution of current between cable cores, metallic screens, ECCs, earthing systems and soil is therefore a key input for assessing both inductive and conductive coupling with nearby metallic pipelines.

4. UNDERGROUND CABLE SYSTEMS: STRUCTURE, LAYING CONFIGURATIONS AND SHEATH BONDING

High-voltage underground cable systems exhibit electromagnetic characteristics that strongly depend on both the constructional and installation features of the system. Unlike overhead lines, where the geometry of the phase conductors represents the main element defining the interfering source, underground cable systems are also influenced by the structure of the single-core cable, the presence of metallic screens, the grounding arrangement, the geometrical configuration of the phases and the possible presence of earth continuity conductors.

These elements directly affect the distribution of induced currents, the return-current paths under both operating and fault conditions, and the residual external magnetic field generated by the cable system. As a consequence, the assessment of interference towards metallic pipelines or other nearby buried utilities cannot be reduced to the current flowing in the phase conductors alone, but requires a consistent representation of the entire cable system and its electrical connections [23], [24], [25], [18].

This chapter therefore describes the main components of underground cable systems that are relevant for electromagnetic interference analysis: the structure of single-core HV cables, the main laying configurations, the bonding arrangements of metallic sheaths, and the role of earth continuity conductors, link boxes and joint bays. This framework provides the link between the physical description of the coupling mechanisms and the subsequent numerical modelling of interference scenarios.

In the following sections, the schemes and components discussed are not intended as an exhaustive review of all possible construction solutions, but rather as the elements that are most relevant for reconstructing the electromagnetic behaviour of an HV underground cable link operating in proximity to metallic pipelines. The focus is therefore placed on the aspects that can modify current return paths, the residual magnetic field and the voltages induced on the interfered pipeline.

4.1 Structure of Single-Core HV Cables

High-voltage underground transmission systems are generally implemented using single-core cables, in which each phase consists of a central conductor (core), an insulation system, semiconductive layers, a metallic screen or sheath, and an external protective jacket. In modern XLPE cables, the cable core includes the conductor, the inner and outer semiconductive layers, and the main insulation, while the metallic sheath and the external covering complete the cable system structure [36].

In technical documentation related to HV cable links of the Italian National Transmission Network (RTN), the metallic sheath is described as an element performing not only a shielding function, but

also mechanical and electrical functions. It may consist, for example, of an aluminium or lead metallic tube, or copper wires, with a cross-section suitable for ensuring mechanical protection, radial watertightness and the capability to withstand earth-fault currents. A polyethylene outer jacket is generally applied over the metallic sheath to provide corrosion protection and electrical separation from the surrounding environment [37], [38].

The structure described above is consistent with the examples shown in Figure 4.1, where different construction solutions for single-core XLPE-insulated land HV cables are compared. The main differences concern the type of metallic screen or sheath adopted, which may consist of welded aluminium sheath, aluminium laminate sheath, copper wires, lead-alloy sheath, or combinations of copper wires and lead sheath. Despite these differences, all configurations share the presence of the central conductor, the main insulation, semiconductive layers, longitudinal water-blocking systems and the external protective jacket.

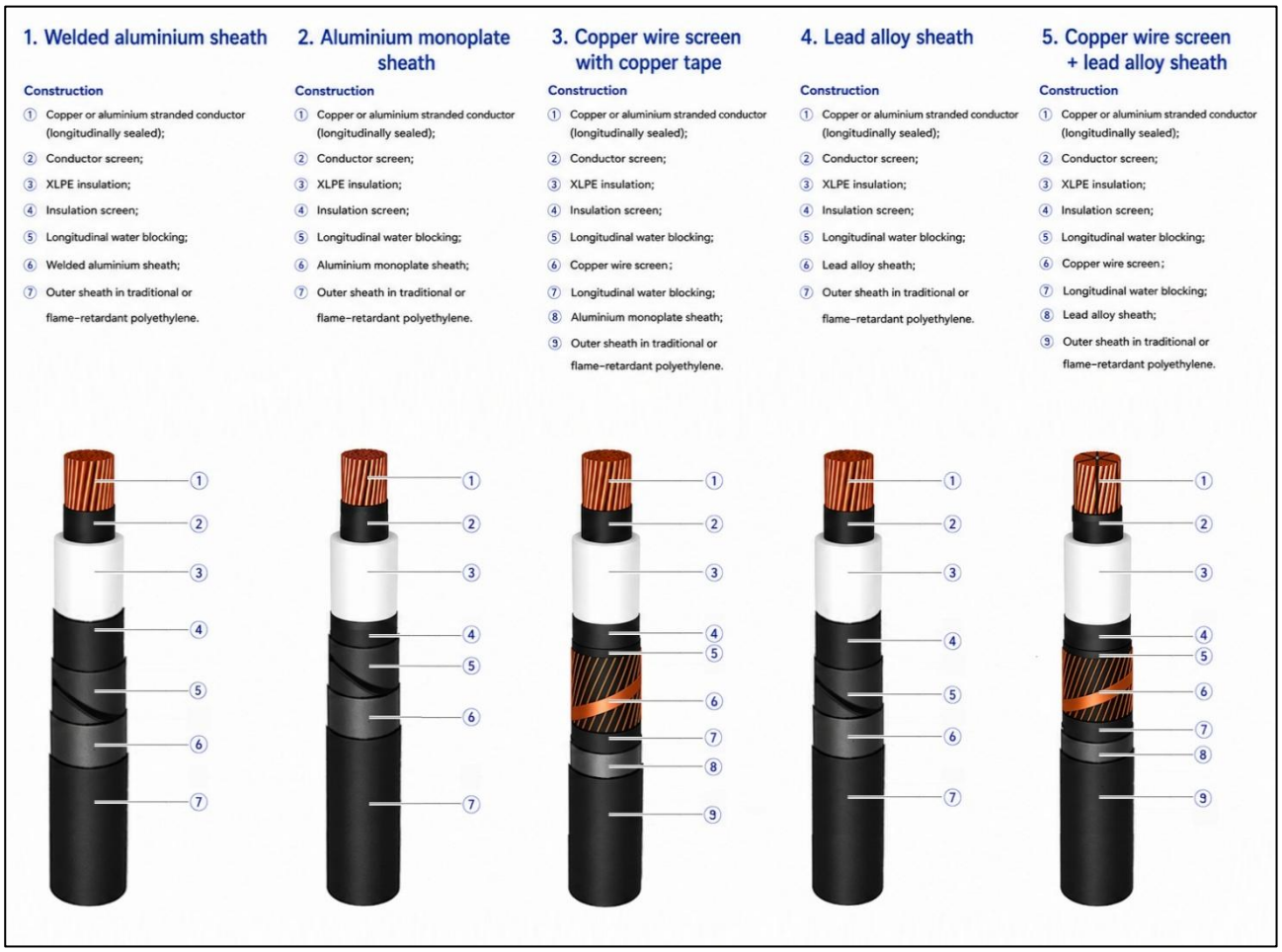


Figure 4.1: Examples of construction configurations for single-core HV land cables with XLPE insulation, graphically developed in this work based on the technical and constructional data reported in the Prysmian catalogue [39].

For the purposes of this thesis, the constructional description of the cable is not intended as a complete cable design specification, but as the basis for identifying the parameters that are relevant for electromagnetic modelling. In particular, the conductor material and cross-section, the conductor

radius, the insulation thickness, the metallic sheath or screen material, the sheath radius and the equivalent sheath cross-section define the relative position and electrical characteristics of the current-carrying core and the metallic return path. These quantities are required to estimate self and mutual impedances, induced sheath voltages, sheath currents and the residual external magnetic field.

Since the objective is to describe a general modelling approach rather than a specific commercial cable, representative ranges are preferable to manufacturer-specific data. Table 4.1 therefore summarises the typical conductor materials and cross-sections considered for HV underground cable systems, grouped according to voltage level. These data provide a practical basis for selecting the geometrical and electrical parameters to be adopted in the subsequent interference model.

Table 4.1: Typical conductor cross-sections used in Terna high-voltage underground cable systems according to the voltage level and conductor material. The listed values refer to nominal conductor cross-sections commonly adopted in transmission applications. For 380 kV systems, different cable designs may be available for the same nominal conductor cross-section (2000 mm² and 2500 mm²) [40], [41], [42].

Voltage level	**Conductor material**	**Typical conductor cross-sections [mm²]**
132 – 150 kV	Cu	400 – 630 – 1000 – 1200
	Al	400 – 1000 – 1600
220 kV	Cu	1000 – 1200 – 1600 – 2000 – 2500
	Al	1600
380 kV	Cu	2000 – 2500
	Al	/

From an electromagnetic point of view, the metallic sheath is the most relevant component of the cable structure for interference analysis. Depending on the sheath bonding arrangement, it may carry induced voltages and currents or participate in the return path of fault currents. For this reason, when modelling interference towards nearby metallic pipelines, the single-core cable should not be represented only by the phase conductor, but also by the metallic elements that influence current distribution and the external magnetic field [36], [43].

Although the external jacket does not represent a metallic return path, it contributes to defining the electrical separation between the metallic sheath and the surrounding environment. The following sections therefore analyse the installation and bonding features that determine how the metallic sheaths and possible auxiliary conductors are connected, positioned and involved in current return paths.

4.2 Laying configurations

The geometrical arrangement of the phases represents one of the main parameters affecting the magnetic field generated by an underground cable system. Unlike overhead lines, where conductor spacing is generally large, underground cable systems can be installed with more compact configurations, thereby modifying the degree of mutual cancellation between the magnetic fields generated by the three-phase currents.

As shown in Figure 4.2, the most common configurations are flat formation, triangular arrangement and trefoil arrangement [36], [44].

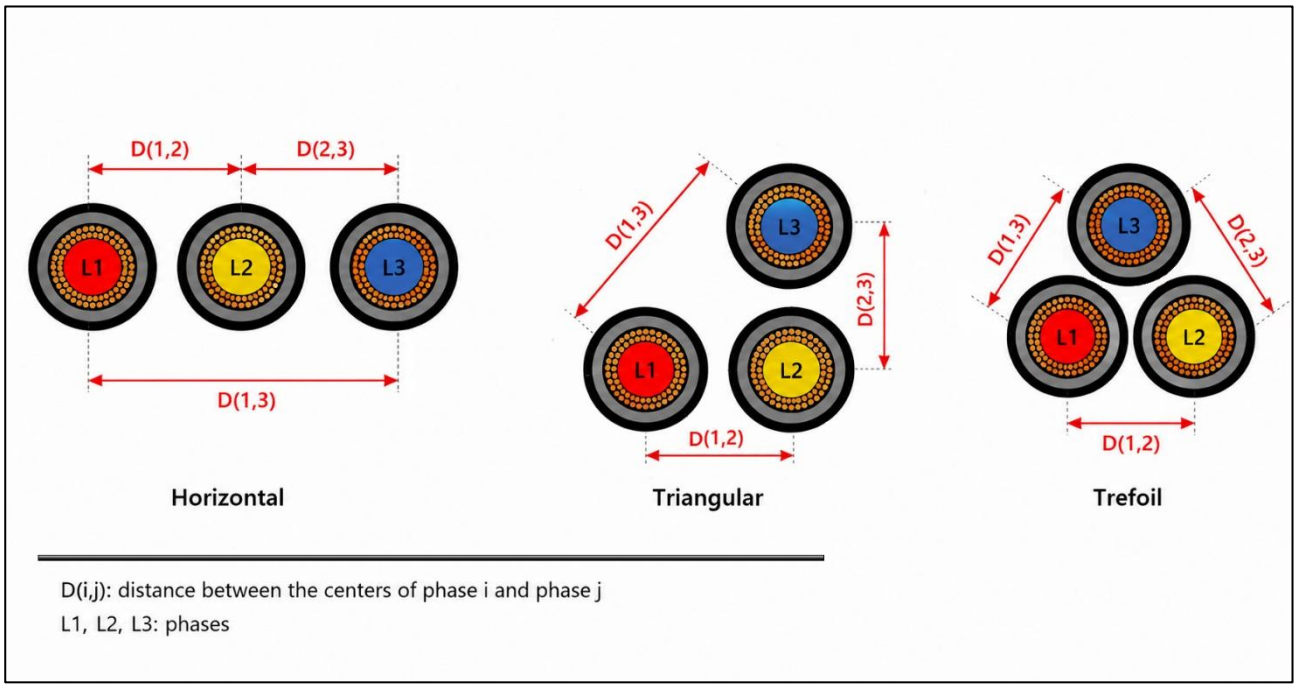


Figure 4.2: Schematic representation developed in this work of typical arrangements for single-core HV underground cables: horizontal, triangular and trefoil configurations.

In flat formation, the phases are arranged side by side along the same direction; in triangular arrangements, the cables are positioned at the vertices of a triangular geometry; in trefoil arrangements, the three phases are grouped in a highly compact configuration. In general, smaller spacing between phases promotes mutual cancellation of the magnetic fields, whereas larger geometrical separation may result in a higher residual external magnetic field.

Under normal operating conditions, the trefoil arrangement generally represents a favourable solution from the magnetic-field point of view, since the three phases are arranged in a compact and symmetrical configuration. The different elevation of the individual cables within the trefoil has only a limited effect compared with the overall burial depth, as cable dimensions are typically of the order of centimetres whereas burial depths are of the order of metres. Under single line-to-earth fault conditions, however, the relative importance of the laying configuration may decrease, since the magnetic-field distribution becomes dominated by the phase carrying the fault current and by the

associated return-current paths. The laying arrangement therefore remains an important geometrical parameter, but it must be evaluated together with the correct representation of metallic sheaths, earth continuity conductors and grounding points. For this reason, the choice of the laying configuration has not only installation and thermal implications, but also directly affects the level of magnetic coupling with nearby metallic pipelines and other buried utilities [23], [24], [25].

In practical HV cable-link projects, trench installation with trefoil arrangement is a common solution for 132–220 kV systems [37]. Similar configurations are also reported in Terna project documentation for 132 kV cable links, where underground installation typically includes trefoil arrangement, burial depths of approximately 1.6 m, and metallic-sheath bonding arrangements based on either cross-bonding or single-point bonding [38].

As an example, Figure 4.3 shows a typical duct-bank cross-section of an underground HV cable link arranged in an “L” configuration. This example highlights that the geometry of the cable system should not be interpreted merely as the relative arrangement of the three phases, but rather as the overall configuration of the installation corridor.

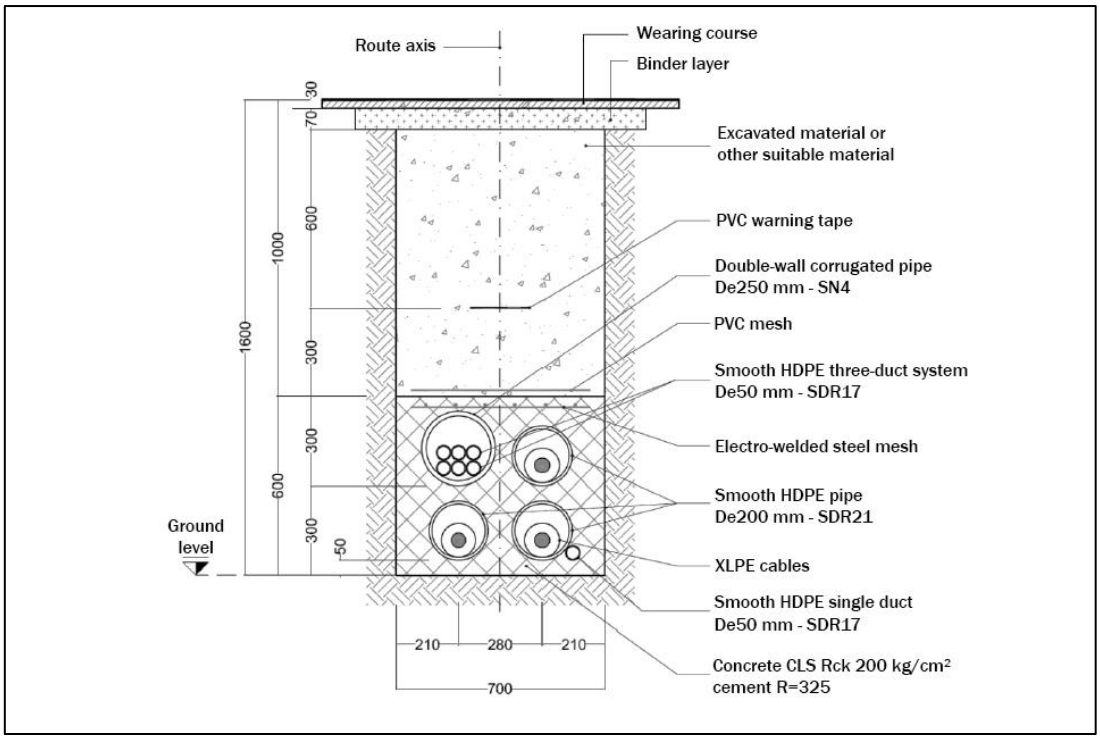


Figure 4.3: Typical trench cross-section for an HV underground XLPE cable system in an L-shaped arrangement, showing cable ducts, auxiliary pipes, protection layers, warning tape, backfilling materials and road pavement layers, from an internal Terna technical document [45].

Beyond the phase arrangement, burial depth and lateral separation from the interfered infrastructure also influence the level of interference. Increasing the lateral separation between the cable system and the pipeline tends to reduce mutual coupling, whereas burial depth modifies the geometry of the coupling circuit and the role of the soil as a return-current path. These aspects are

particularly relevant in electromagnetic compatibility studies, since the actual geometry of the infrastructure corridor determines the distribution of the external magnetic field and therefore the voltages that may be induced on nearby metallic structures [23], [24], [18].

The laying configuration must also be evaluated together with the presence and position of additional metallic conductors, such as earth continuity conductors or earthing wires. These elements may modify the return-current paths of induced or fault currents and, depending on their position with respect to the phase conductors and metallic sheaths, may contribute to changes in the residual external magnetic field. Their position should therefore be considered as part of the system geometry, since it may influence both current distribution and the resulting external magnetic field [32], [33].

The laying configuration must also be considered together with the thermal behaviour of the system. More compact arrangements may favour magnetic field cancellation, but can also affect heat dissipation and cable ampacity. Conversely, larger spacing between phases may improve certain thermal aspects while increasing the residual external magnetic field. Similarly, although a greater burial depth may increase the distance between the source and the interfered structure, it is not generally pursued as a mitigation measure for electromagnetic interference, since deeper excavation entails higher installation costs and may worsen the thermal performance of the cable system. The choice of the cable layout therefore represents a compromise between electrical, thermal, installation and electromagnetic compatibility requirements [36], [43].

For interference modelling purposes, the laying configuration must therefore be represented consistently with the actual installation or with the considered study scenario. Parameters such as phase arrangement, burial depth, spacing between cables, distance from the interfered pipeline, position of possible earth continuity conductors and the presence of other metallic conductors within the corridor directly affect the calculation of mutual impedances and the estimation of induced voltages. In the following sections, this geometrical description will be integrated with the analysis of metallic-sheath bonding arrangements, which represent another key factor affecting current distribution and the external magnetic field.

4.3 Sheath bonding arrangement

The metallic sheaths of single-core cables should not be regarded merely as constructional or protective elements, but as electrically active components of the cable system. In the presence of alternating current in the core conductor, the associated time-varying magnetic field links with the metallic sheath and induces a longitudinal voltage along it. The effect of this induced voltage depends on the bonding arrangement adopted: if a closed metallic path is available, circulating sheath currents may flow during normal operation; if the sheath is not continuously bonded to earth, sheath-to-earth

voltages may instead appear along the cable section. Under fault conditions, the sheath may also contribute to the return path of the fault current [34], [36], [43].

Figure 4.4 qualitatively illustrates this mechanism. The current flowing in the core conductor generates a magnetic field around the cable; when the sheath circuit is electrically closed, the induced voltage can drive a longitudinal current in the metallic sheath. These currents are particularly relevant during normal operation, since they produce additional Joule losses, increase cable heating and may reduce the admissible current-carrying capacity of the cable system, leading to ampacity derating. This is one of the main reasons why different sheath bonding arrangements are adopted in HV cable systems.

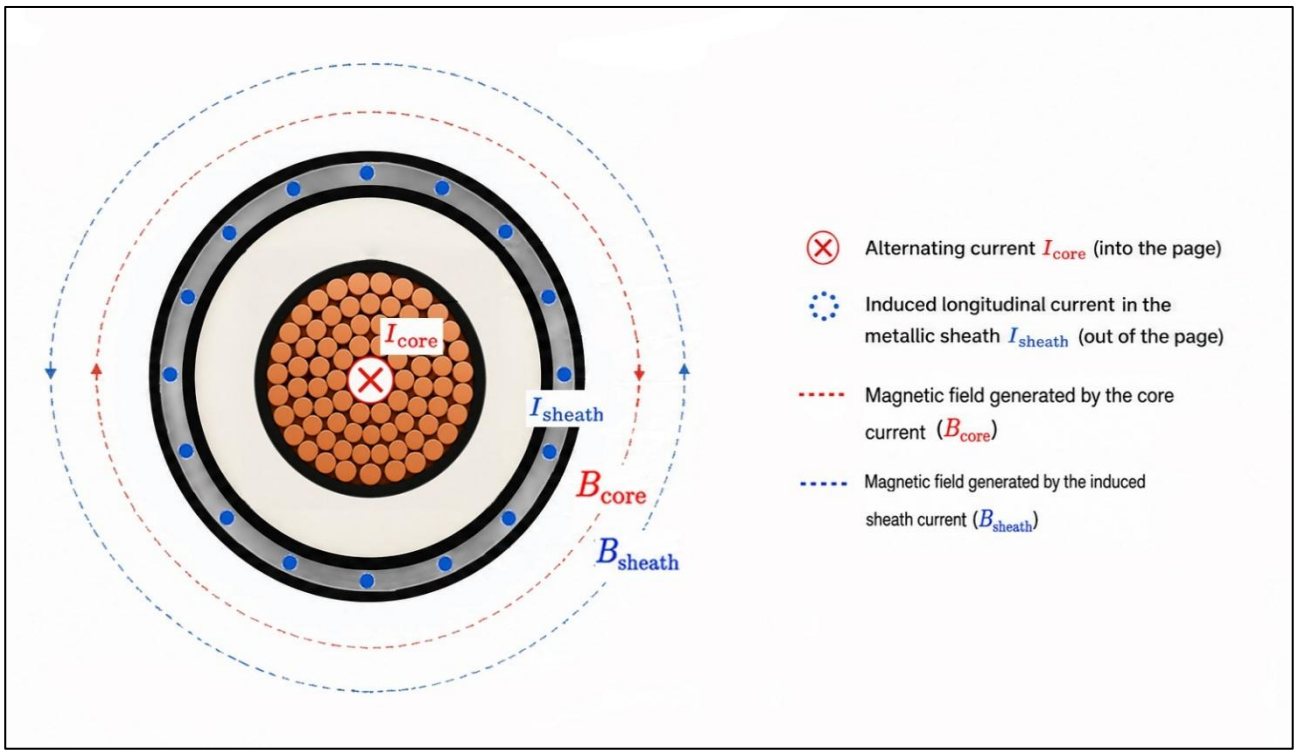


Figure 4.4: Qualitative cross-sectional representation developed in this work of a single-core HV cable, showing the conductor current, the induced longitudinal current in the metallic sheath and the associated magnetic fields. The figure is intended for explanatory purposes; the actual sheath current distribution depends on the bonding arrangement, grounding conditions, cable geometry and surrounding return paths.

From a circuital and modelling point of view, the bonding arrangement defines the boundary conditions of the metallic sheath: it determines whether the induced voltage mainly results in circulating sheath currents, sheath-to-earth voltages, or fault-current sharing through the metallic layers. The resulting current distribution depends on the sheath impedance, the mutual coupling with the core conductor, possible parallel return conductors and the earthing resistances at the bonding points. Therefore, sheath bonding must be explicitly represented in interference studies, since it affects cable losses and ampacity during normal operation, as well as return-current paths, reduction factor and residual magnetic field under fault conditions [8], [46], [47].

The bonding arrangements of metallic sheaths can be grouped into three main schemes:

- solid bonding,
- single-point bonding and
- cross-bonding.

The selected bonding arrangement has a direct impact on the electrical behaviour of the cable system, since it determines whether the metallic sheath acts as a closed circuit, a conductor earthed at a single point, or a sectionalised system providing compensation along the route. As a consequence, sheath bonding influences induced voltages, circulating currents, additional losses, cable ampacity and possible fault-current return paths [34], [36], [43].

Solid bonding, or earthing at both ends, is the simplest bonding arrangement. In this configuration, the metallic sheaths of the single-core cables are interconnected and earthed at both ends of the section. This keeps the sheath potential close to earth potential and provides a low-impedance path for possible fault currents. However, since both-end bonding electrically closes the sheath circuit, voltages induced by the current in the central conductor may produce circulating sheath currents even under normal operating conditions. These currents cause Joule losses in the metallic sheath and may reduce the ampacity of the cable [34], [35], [39], [43].

Figure 4.5 shows the solid bonding scheme, in which the metallic sheaths of the single-core cables are interconnected and earthed at both ends of the section.

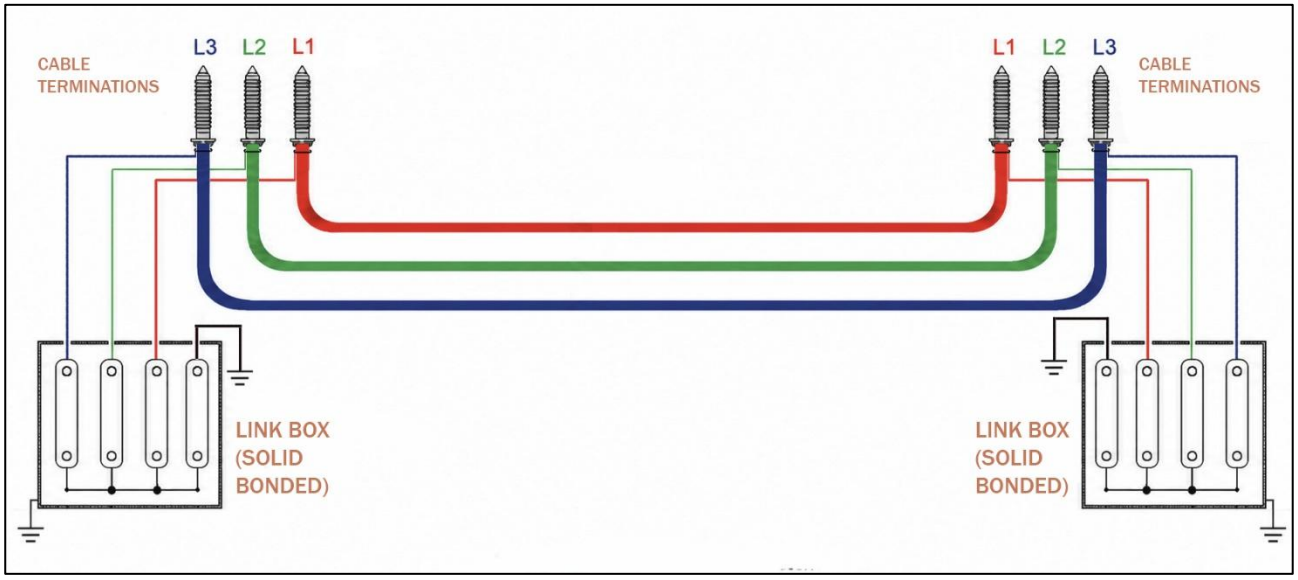


Figure 4.5: Solid bonding configuration developed in this work for single-core HV cable systems, in which the metallic sheaths are connected together and earthed at both ends of the section.

In single-point bonding, the metallic sheaths are connected to earth at only one point within each electrically continuous sheath section, while the opposite end remains insulated from earth and is generally protected by surge arresters. Since no closed sheath circuit is formed, circulating sheath

currents are eliminated or significantly reduced during normal operation, thereby limiting sheath losses and the associated ampacity derating [34], [35], [39], [43].

In the conventional end-point arrangement shown in Figure 4.6(A), the sheaths are solidly bonded at one cable termination and protected by surge arresters at the opposite termination. For longer links, the route may be divided into several electrically independent sheath sections by means of sheath sectioning insulators and intermediate link boxes, as shown in Figure 4.6(B). Each section remains single-point bonded, while surge arresters protect the insulated sheath ends. This configuration is referred to as sectionalised single-point bonding. When a single earthing point is instead located at the centre of the route and both cable terminations are insulated from earth and protected by surge arresters, the arrangement is defined as mid-point bonding [34], [35], [39], [43].

The main limitation of these arrangements is the induced sheath-to-earth voltage, which increases with distance from the earthing point. The length of each sheath section must therefore be selected so that the permissible voltage is not exceeded. For substantially longer cable links, cross-bonding is generally adopted. An earth continuity conductor installed in parallel with the cables ensures the continuity of the earthing path without altering the sheath bonding arrangement [34], [35], [39], [43].

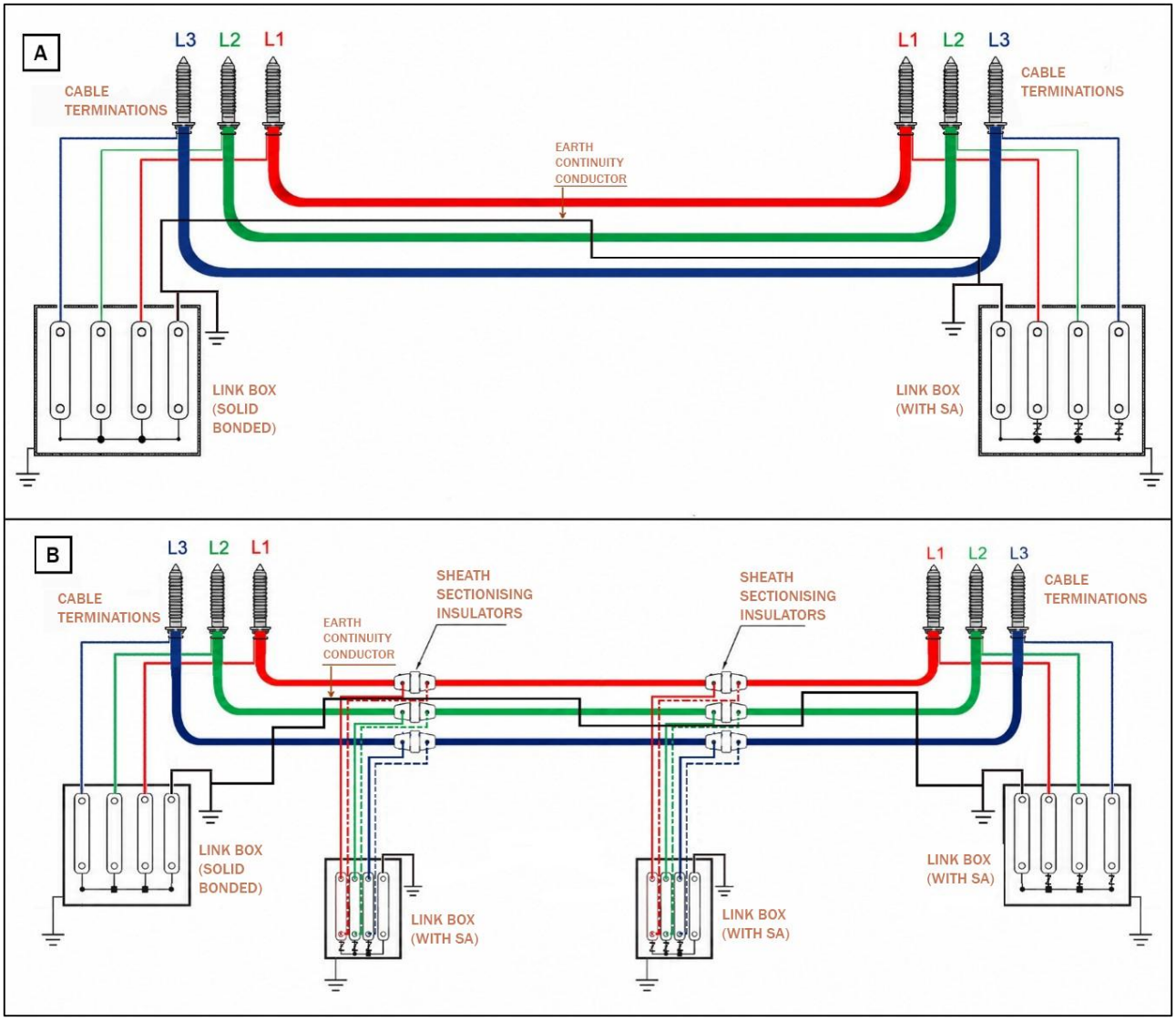


Figure 4.6: Single-point bonding arrangements for single-core HV cable systems: (A) conventional end-point bonding; (B) sectionalised single-point bonding with sheath sectioning insulators and surge arresters.

For longer sections, cross-bonding is a widely used solution. In this scheme, the metallic-sheath system is divided into elementary sections, generally grouped into a major section, and the sheaths of the three phases are cross-connected in the link boxes. The aim is to make the induced sheath voltages in the different sections compensate each other vectorially as much as possible, thereby reducing the overall residual voltage and limiting circulating currents under normal operating conditions [34], [35], [43].

The effectiveness of cross-bonding also depends on the geometrical arrangement of the three cables along the route. In flat configurations, the three phases occupy different geometrical positions: the central phase and the two outer phases do not have the same mutual distances and are not exposed to the same level of magnetic coupling. In such cases, physical transposition of the cables along the route may also be adopted, so that each phase successively occupies the different geometrical positions. In compact configurations, such as trefoil laying, the three phases are instead placed in

more similar geometrical conditions with respect to the other conductors; for this reason, cross-bonding may also be implemented without physical cable transposition.

It is nevertheless important to distinguish between physical cable transposition and the electrical cross-connections of the sheaths in the link boxes. The metallic sheaths are not physically transposed along the route; rather, they continue along their own physical path and are electrically cross-connected inside the link boxes to the sheath of another phase. As a result, over successive sections, the sheath circuit is associated with different phase conductors and with the corresponding induced voltages, allowing the induced electromotive forces to be compensated without interpreting the scheme as a physical transposition of the sheaths.

Under ideal conditions, with sections of equal length and sufficiently regular geometry, cross-bonding can therefore reduce sheath losses while maintaining the electrical continuity of the shielding system [34], [35], [43]. Figure 4.7 schematically shows two typical configurations: one with sheath cross-bonding only, without physical cable transposition, generally associated with compact arrangements such as trefoil laying; and one with both physical cable transposition and sheath cross-bonding, more commonly adopted in flat arrangements.

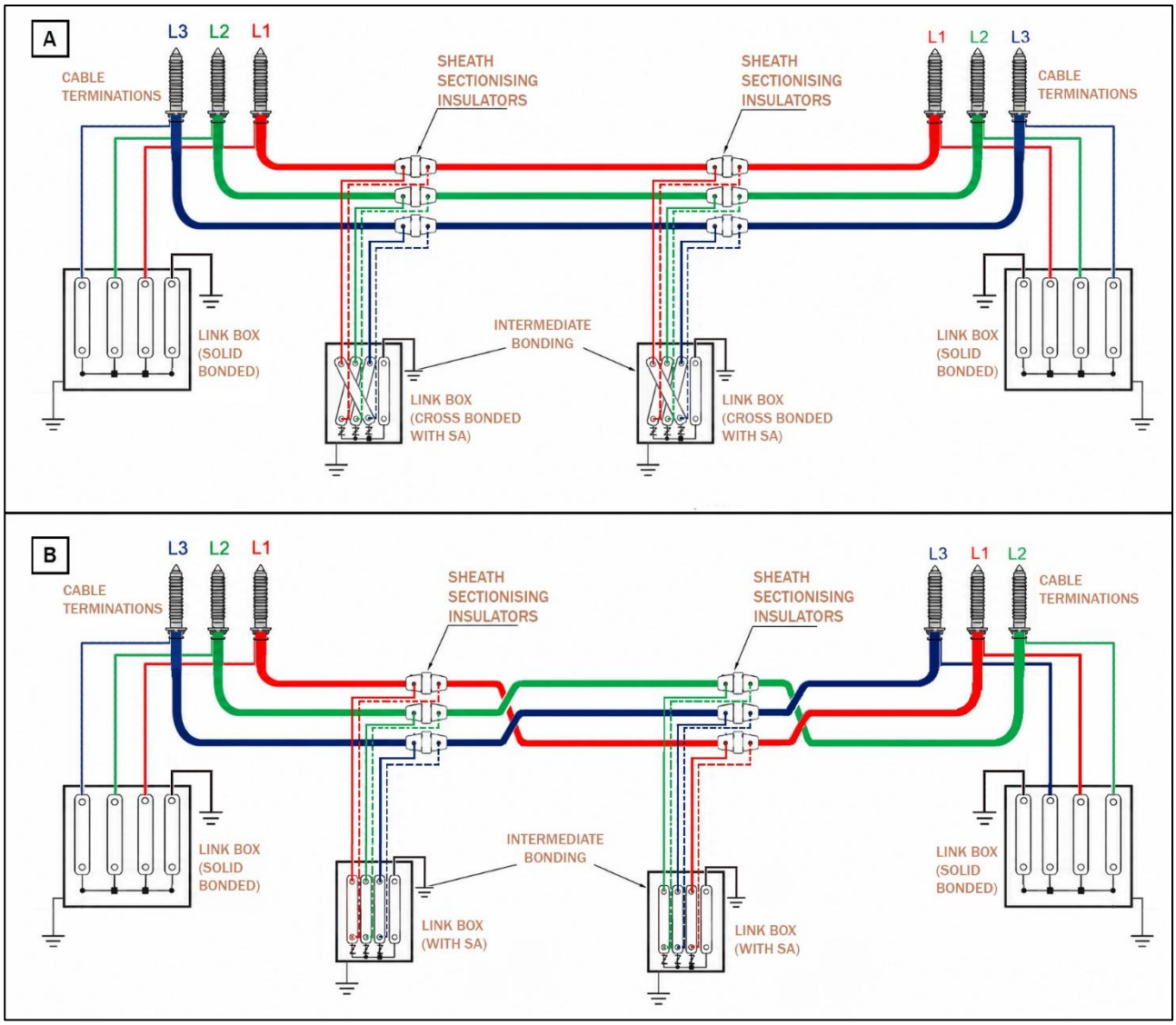


Figure 4.7: Cross-bonding configurations developed in this work for single-core HV cable systems: (A) cross-bonded system without cable transposition, typically associated with compact arrangements; (B) cross-bonded system with cable transposition, where the phase cables are physically transposed and the metallic sheaths are cross-connected through link boxes to balance the induced sheath voltages.

In engineering practice, the sheath bonding arrangement is mainly determined by the design constraints of the cable link itself, rather than by the presence of nearby interfered infrastructures. The selected scheme depends on the total length of the connection, the available cable drum lengths, the position of joints and terminal substations, the subdivision into elementary and major sections, the acceptable sheath-to-earth voltages and the need to limit circulating currents and additional losses during normal operation.

For long HV cable links, cross-bonding is generally preferred, since it allows the induced sheath voltages to be compensated over successive sections and reduces circulating sheath currents and the associated ampacity derating. However, a complete cross-bonded arrangement is not always achievable along the entire route. Short sections, residual portions close to terminal substations or links, whose length does not allow a regular subdivision, may require a different bonding

arrangement, typically single-point bonding. Therefore, the same cable link may include a mainly cross-bonded route and a final section with a different bonding scheme near the substation [34], [35], [39], [43].

Solid bonding, although conceptually simple, is generally less favourable for long single-core HV cable links because it creates a closed sheath circuit in which induced currents can circulate continuously during normal operation. These currents increase sheath losses and may reduce the current-carrying capacity of the cable. For this reason, solid bonding is usually limited to specific local applications where the resulting losses and operating constraints remain acceptable [34], [35], [39], [43].

Although the presence of a nearby pipeline does not usually determine the sheath bonding scheme, the adopted arrangement remains a key input for interference modelling, since it defines the electrical continuity of the metallic sheaths and the available return paths for induced and fault currents. In sections where cross-bonding is not feasible, the possible use of one or more earth continuity conductors may provide additional parallel return paths, but this choice must be assessed together with its effects on losses, ampacity and grounding design [8], [32], [33], [48].

Therefore, in the interference model, the sheath bonding scheme should not be treated as an arbitrary mitigation option selected only to reduce the interference on the pipeline. It should instead be represented as a design feature of the cable link, imposed by constructional and operational constraints, which affects current return paths, the residual external magnetic field and the voltages induced on parallel metallic pipelines. In particular, cross-bonded configurations are generally more favourable from the shielding point of view, since the three metallic sheaths provide distributed return circuits along the cable route and contribute to reducing the effective inductive coupling with nearby metallic infrastructures [23], [24], [34], [35].

4.4 Joint bays and earthing systems

Underground cable links are generally composed of several cable sections connected through intermediate joint bays. Unlike the cable core and insulation, which are distributed continuously along the route, joint bays introduce discrete nodes where electrical and geometrical characteristics may change. These installations are therefore relevant for electromagnetic interference studies, particularly under fault conditions, when part of the return current may flow through metallic sheaths, earthing conductors and local grounding systems.

The following sections analyse the typical configuration of joint bays and the characteristics of the associated earthing systems, which constitute an important part of the return-current network of the cable link.

4.4.1 Typical Joint Bay Configuration

Joint bays are discontinuity points along underground cable links, where successive cable sections are joined and the associated sheath-bonding, earthing and overvoltage-protection connections are implemented. Depending on the adopted bonding arrangement, they may include cable joints, link boxes, surge arresters and connections to the local earthing system. Figure 4.8 shows an HV cable joint bay during installation.

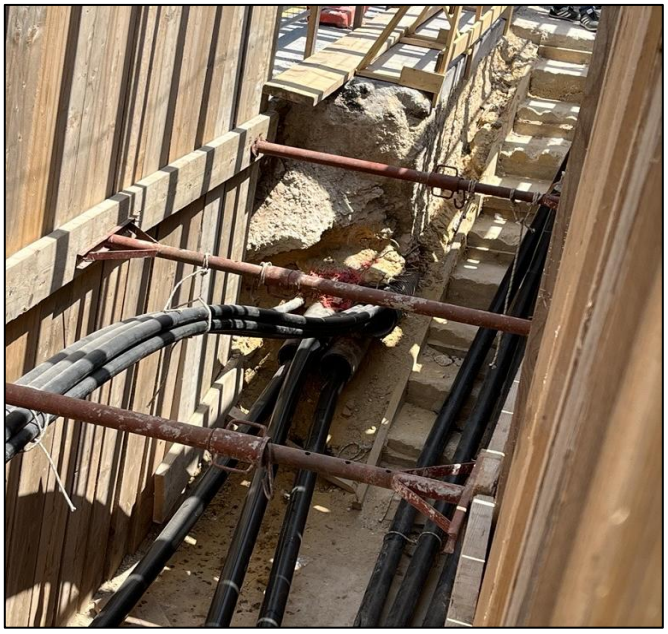


Figure 4.8: Field view of an HV underground-cable joint bay during installation, showing the incoming and outgoing single-core cables and the prepared jointing area [49].

The cable joints are installed within the bay, whereas the link boxes and earthing connections are generally placed in accessible chambers nearby. This arrangement permits inspection, testing and possible reconfiguration of the sheath connections during the service life of the cable system.

Link-box construction depends on the adopted sheath-bonding arrangement. Cross-bonding boxes provide the electrical cross-connections between the sheaths of successive cable sections, while single-point-bonding boxes implement the corresponding sheath termination and earthing arrangement. Surge arresters may also be installed between the cable sheaths and earth to limit transient and fault-induced overvoltages. Examples of these configurations are shown in Figure 4.9.

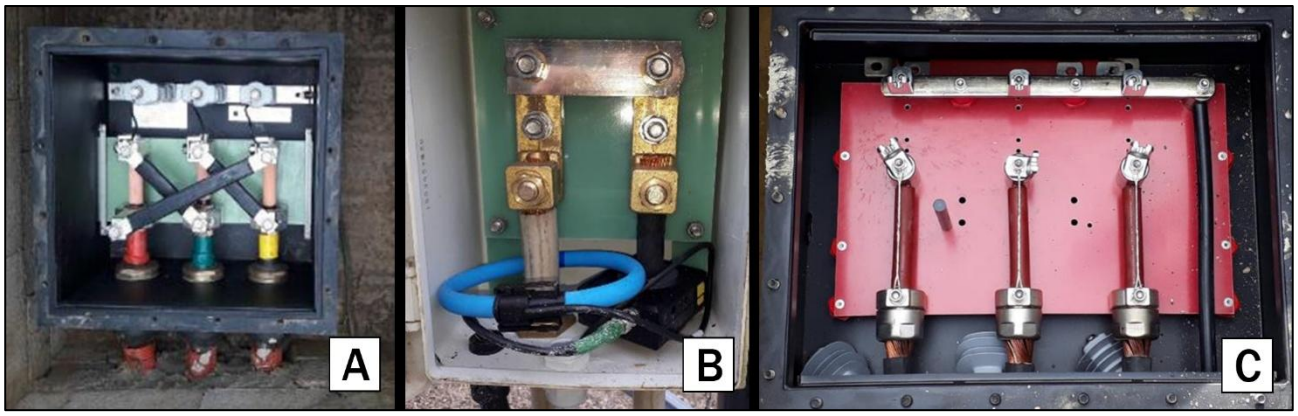


Figure 4.9: Typical cable-sheath link-box configurations used in HV cable systems: (A) cross-bonding link box, (B) single-point-bonding link box, and (C) link box equipped with three surge arresters connected between the cable sheaths and earth for overvoltage protection [50], [51].

For electromagnetic-interference assessment, the local joint-bay earthing system is particularly relevant. The metallic sheaths, link boxes and surge arresters are connected to a dedicated grounding arrangement that provides an earth-current return path and limits the resulting local earth-potential rise under fault conditions. Figure 4.10 shows the reference grounding geometry considered in this work.

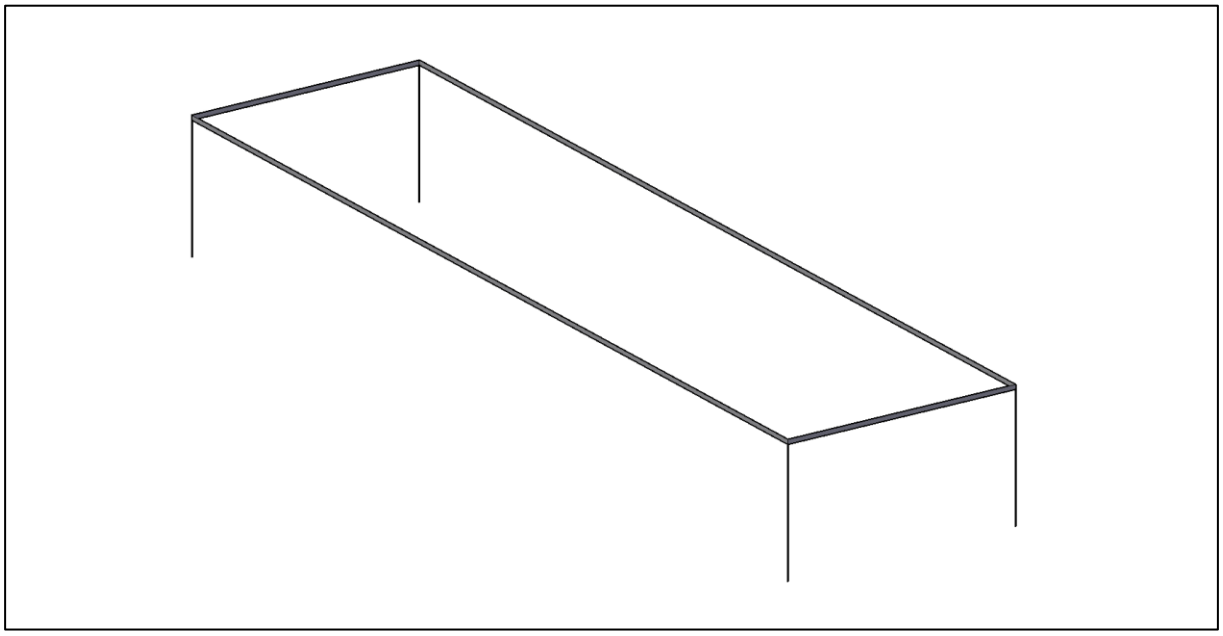


Figure 4.10: Simplified CAD layout developed in this work for the reference 150 kV joint-bay grounding system, showing the buried perimeter conductor and the vertical earth electrodes.

The main geometrical characteristics of the reference grounding system adopted in this study are summarised in Table 4.2. These parameters define the grounding arrangement used in the numerical analysis of Sections 4.4.2 and 4.4.3.

Table 4.2: Geometrical characteristics adopted in this work for the reference 150 kV joint-bay grounding system.

Parameter	Value
Ring size	11 m × 2.8 m
Burial depth	2.1 m
Ring conductor cross-section	125 mm²
Number of vertical electrodes	4
Vertical electrode length	1.5 m
Vertical electrode cross-section	314.16 mm²

Under normal operating conditions, negligible currents are expected to be exchanged with the surrounding soil. During earth faults, however, part of the return current may flow through the local grounding system, producing an earth potential rise and modifying the distribution of current between metallic sheaths, possible earth continuity conductors and the surrounding soil.

For this reason, the joint-bay grounding system should not be regarded only as a safety component. It is part of the return-current network of the cable link, and its geometry and grounding resistance become relevant parameters in interference studies involving nearby buried pipelines.

4.4.2 Earthing resistance of joint-bay grounding systems

As discussed in the previous section, the earthing system of a joint bay constitutes an integral part of the return-current network of the cable link. Its electrical behaviour is commonly characterised by the grounding resistance, which determines the relationship between the current injected into the soil and the resulting rise of earth potential.

For a given grounding arrangement installed in homogeneous soil, the grounding resistance can be expressed as:

$$R_g = k \cdot \rho \tag{4.1}$$

where:

- R_g is the grounding resistance [Ω];
- ρ is the soil resistivity $[\Omega \cdot m]$;
- k is a geometrical coefficient that depends on the dimensions and configuration of the grounding system $[m^{-1}]$.

For the reference 150 kV joint-bay grounding system considered in this study, the coefficient k was obtained numerically from the homogeneous-soil case and resulted equal to $k = 0.0589\ \mathrm{m}^{-1}$. Therefore, for homogeneous soil conditions, the grounding resistance of the considered arrangement can be written as:

$$R_g = 0.0589 \cdot \rho \tag{4.2}$$

This relationship provides a useful reference condition, since it allows the influence of the grounding geometry to be separated from that of the soil properties. In real installations, however, soil conditions are often non-uniform and may exhibit vertical stratification. A common representation consists of a two-layer soil model characterised by an upper-layer resistivity ρ_1, a lower-layer resistivity ρ_2, and an upper-layer thickness h.

In this case, the grounding resistance can no longer be described by a simple linear relationship. The current injected into the soil is distributed between the two layers according to their electrical properties, and the resulting grounding resistance becomes a function of all three parameters:

$$R_g = \mathcal{F}(\rho_1, \rho_2, h) \tag{4.3}$$

The influence of soil stratification is particularly relevant for joint-bay grounding systems, since the dimensions of the buried conductors, the length of the vertical electrodes and their burial depth may be comparable with the thickness of the upper soil layer. As a consequence, the same grounding arrangement may exhibit different grounding resistances depending on the local geoelectrical conditions.

For this reason, the 150 kV joint-bay grounding system shown in Figure 4.10 was used as the reference geometry for the parametric analysis presented in the following section.

4.4.3 Parametric analysis in two-layer soil

The numerical results presented in this section were obtained in this work for the reference 150 kV joint-bay grounding system described above. To evaluate the influence of soil stratification on the grounding performance of the joint-bay earthing system, a parametric analysis was performed using the 150 kV grounding arrangement shown in Figure 4.11 as the reference geometry. The objective was to investigate how the grounding resistance varies as a function of the electrical properties of a two-layer soil.

The analysis was carried out by varying the resistivities of the upper and lower soil layers while maintaining a fixed grounding geometry. The grounding resistance was calculated for different combinations of ρ_1, ρ_2 and upper-layer thickness h.

The parametric analysis was first performed by fixing the upper-layer thickness to two representative values, $h = 0.5$ m and $h = 2\,m$, while varying both ρ_1 and ρ_2 within the selected range. The resulting grounding-resistance distributions are shown in Figure 4.11.

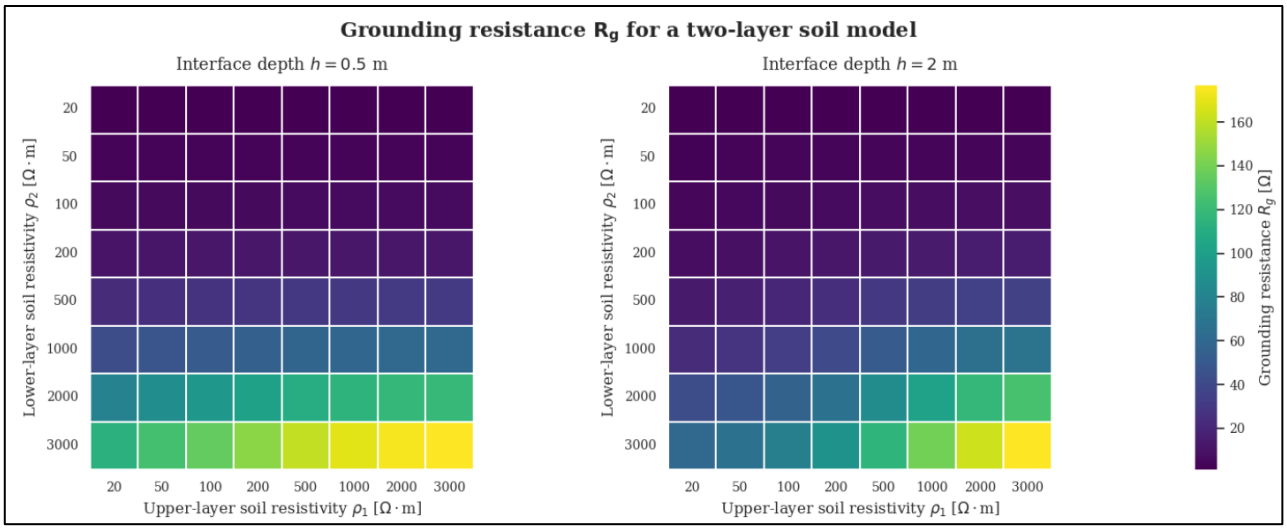


Figure 4.11: Grounding resistance R_g computed in this work for the reference 150 kV joint-bay grounding system as a function of the upper-layer resistivity ρ_1 and lower-layer resistivity ρ_2 in a two-layer soil model. Results are reported for two representative upper-layer thicknesses ($h = 0.5$ m and $h = 2$m).

The comparison between the two maps highlights the combined influence of the upper-layer resistivity, the lower-layer resistivity and the upper-layer thickness on the grounding resistance. In general, higher soil resistivity values lead to higher grounding resistance. However, the relationship is not linear, since the current injected into the soil is distributed between two layers characterised by different electrical properties.

The variation of the interface depth h modifies the relative contribution of the two soil layers to the current dispersion. For a shallow upper layer, the current distribution is more strongly affected by the resistivity of the deeper layer. Conversely, when the upper layer becomes thicker, the grounding system interacts for a larger portion of its current-dispersion region with the upper soil layer, and the influence of the lower layer is progressively reduced. This behaviour explains the differences observed between the two maps and confirms that the same grounding arrangement may exhibit different grounding resistances depending not only on the resistivity values, but also on the vertical stratification of the soil.

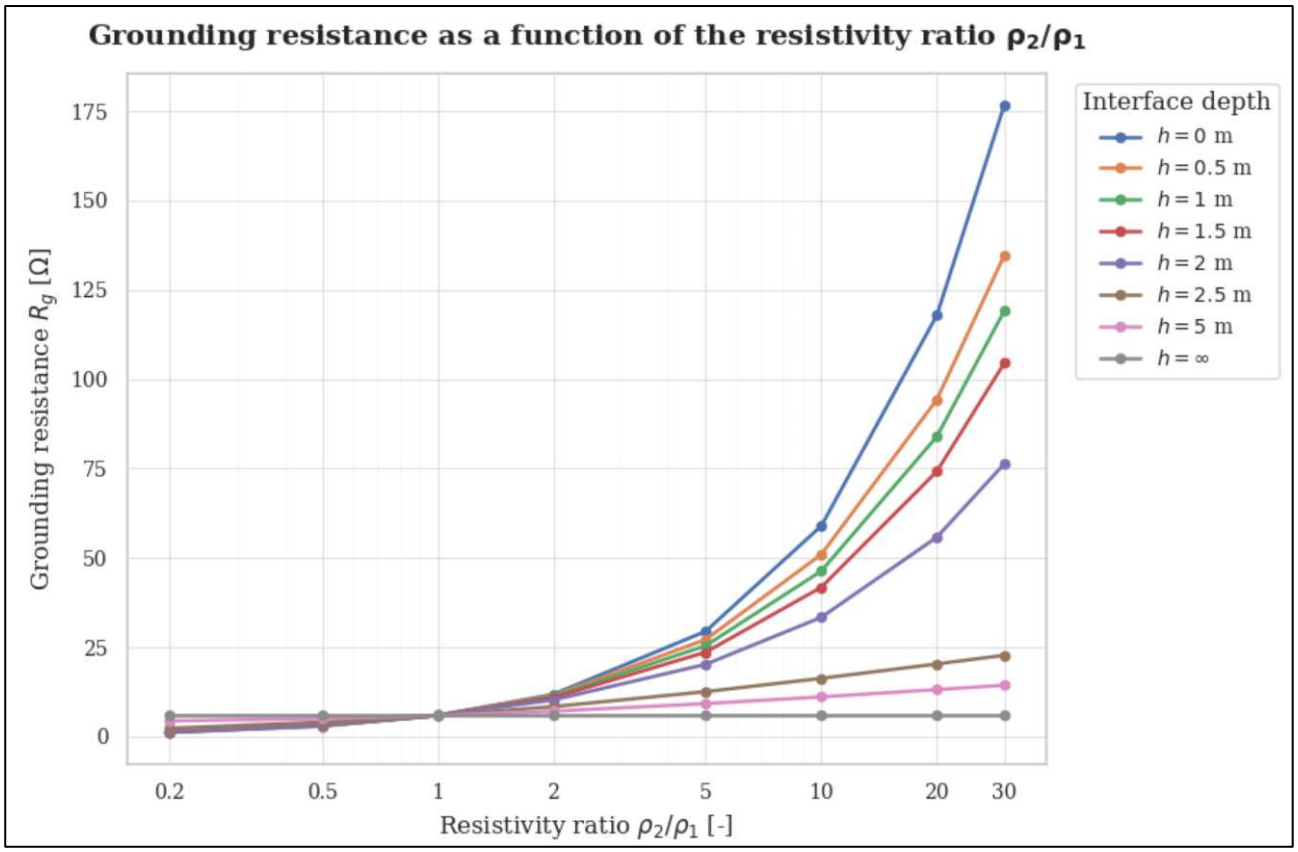


Figure 4.12: Design chart computed in this work for the reference 150 kV joint-bay grounding system. Grounding resistance R_g is plotted as a function of the soil resistivity ratio ρ_2/ρ_1 for different upper-layer thicknesses h, assuming $\rho_1 = 100\ \Omega m$.

In Figure 4.12, the upper-layer resistivity is fixed at $\rho_1 = 100\ \Omega$m. The curves show that, as h increases, the grounding system tends to be progressively influenced mainly by the upper soil layer. As a consequence, the effect of the deeper layer resistivity becomes less significant. This behaviour is particularly evident for h values greater than approximately 2.5 m, for which the increase of ρ_2/ρ_1 produces a much smaller variation of the grounding resistance.

This result is also relevant for conductive interference studies involving nearby buried metallic pipelines. During earth-fault conditions, the soil potential distribution generated by the joint-bay grounding system depends on the same stratification parameters. Therefore, the magnitude of transferred potentials on nearby metallic structures may also be affected by the upper-layer thickness and by the resistivity contrast between the two layers.

An empirical interpolation of the numerical results was then developed for the specific grounding system considered in this study. The calibration dataset was generated from numerical simulations performed with a dedicated software tool developed within Terna, which evaluates the grounding resistance of the considered earthing system using the average potential method. The dataset includes several combinations of upper-layer resistivity ρ_1, lower-layer resistivity ρ_2, and upper-layer thickness h, covering the analysed range of soil configurations.

The predictive capability of the proposed interpolation formula was assessed using an independent validation dataset obtained from CDEGS simulations. These simulations were performed at intermediate parameter values not included in the calibration grid, in order to verify the ability of the formula to reproduce the grounding resistance between the original tabulated points. The grounding resistance is expressed as:

$$R_g = k\rho_1 e^{\chi W} \qquad \begin{cases} \rho_1, \rho_2 \in [20, 3000]\ \Omega \cdot m \\ h \in [0.2, 5.0]\ m \end{cases} \tag{4.4}$$

In (4.4), R_g is expressed in Ω , ρ_1 and ρ_2 in Ω·m, and h in m. The logarithmic variable χ, the transition functions S_h and S_χ, and the weighting function W are dimensionless. The terms appearing are defined as follows:

$$\begin{cases} k = 0.05892110\ \mathrm{m}^{-1} \\ \chi = \ln\left(\dfrac{\rho_2}{\rho_1}\right) \\ W = (1 - S_\chi)[(1 - S_h)W_{11} + S_h W_{12}] + S_\chi[(1 - S_h)W_{21} + S_h W_{22}] \end{cases} \tag{4.5}$$

The interpolation model is based on two smooth transition functions. The first governs the transition between different thickness regimes, while the second describes the transition between low- and high-contrast resistivity conditions.

$$\begin{cases} S_h = \dfrac{1}{1 + \exp[-\beta_h(h - h_0)]} \\ S_\chi = \dfrac{1}{1 + \exp[-\beta_\chi(|\chi| - \chi_0)]} \end{cases} \tag{4.6}$$

1) Branch $\rho_2 \geq \rho_1$:

$$h_0 = 2.0646\ \mathrm{m}, \qquad \beta_h = 26.4792\ \mathrm{m}^{-1}, \qquad \chi_0 = 1.5691, \qquad \beta_\chi = 59.3954 \tag{4.7}$$

$$\begin{cases} W_{11} = 1.1409 - 0.0242h - 0.0812h^2 - 0.4551\chi + 0.1417\chi h + 0.4084\chi^2 - 0.1853\chi|\chi|^2 \\ W_{12} = 1.1151 - 0.3062h + 0.0258h^2 - 0.0097\chi + 0.0235\chi h - 0.0931\chi^2 + 0.0314\chi|\chi|^2 \\ W_{21} = 1.1488 - 0.1565h + 0.0109h^2 - 0.1086\chi + 0.0171\chi h + 0.0218\chi^2 - 0.0016\chi|\chi|^2 \\ W_{22} = 0.8944 - 0.1807h + 0.0120h^2 - 0.0579\chi + 0.0106\chi h - 0.0015\chi^2 + 0.0001\chi|\chi|^2 \end{cases} \quad (4.8)$$

2) Branch ($\rho_2 < \rho_1$):

$$h_0 = 2.0336\ \text{m}, \quad \beta_h = 60.0000\ \text{m}^{-1}, \quad \chi_0 = 4.9999, \quad \beta_\chi = 59.9879 \quad (4.9)$$

$$\begin{cases} W_{11} = 0.9837 - 0.0300h - 0.0120h^2 - 0.0133\chi - 0.0073\chi h - 0.0032\chi^2 - 0.0002\chi|\chi|^2 \\ W_{12} = 1.5245 - 0.5378h + 0.0587h^2 - 0.0962\chi + 0.0388\chi h + 0.0126\chi^2 + 0.0008\chi|\chi|^2 \\ W_{21} = -2.9410 + 0.5189h - 0.0130h^2 - 6.1275\chi + 0.1031\chi h + 3.7680\chi^2 + 0.9647\chi|\chi|^2 \\ W_{22} = -7.6842 - 8.3927h + 0.0368h^2 + 0.1107\chi - 1.5624\chi h + 1.6005\chi^2 + 0.2386\chi|\chi|^2 \end{cases} \quad (4.10)$$

The predictive performance of the proposed compact interpolation model was evaluated using an independent validation dataset. The resulting error metrics are summarised in Table 4.3.

Table 4.3: Validation performance metrics obtained in this work for the proposed double soft-transition interpolation model.

Metric	***Value***
RMSE	1.3683 Ω
MAE	0.5074 Ω
MAPE	1.297 %
Maximum percentage error	14.656 %
R²	0.996353

5. INTERFERED METALLIC PIPELINES AND AUXILIARY SYSTEMS

In the case of electromagnetic interference between high-voltage underground cable systems and gas pipelines, the interfered infrastructure cannot be represented as a simple uniform metallic pipe buried in the ground. Instead, the pipeline must be modelled as an electrically distributed system, whose behaviour depends on the main pipe, the insulating coating, cathodic protection, insulating joints, grounding connections and protection devices installed along the route [52], [53].

These elements define the electrical continuity, grounding conditions, current return paths and pipe-to-soil potential distribution. Therefore, they must be included in the model to identify the sections most exposed to induced voltages, current concentrations, safety issues and AC corrosion risk [54].

5.1 Pipeline structure

The metallic pipeline is the main conductive path of the interfered system. Under parallel exposure conditions, the magnetic field produced by the cable currents and associated return paths induces a distributed longitudinal voltage along the pipeline. The severity of this coupling depends mainly on separation distance, parallelism length, cable layout and source current, especially under fault conditions [52], [53], [55], [56].

For modelling purposes, the pipeline is represented as a distributed-parameter conductor characterised by a longitudinal impedance and an impedance to ground. Pipeline diameter, wall thickness and material are not the dominant parameters for inductive coupling itself, but they affect the longitudinal impedance of the pipe and therefore the distribution of induced currents along the route [52], [53], [57], [58].

Publicly available documentation on the Snam National Gas Pipeline Network shows that buried gas pipelines may cover a wide range of nominal diameters, from small connection lines to large transmission pipelines. In the analysed documentation, diameters range from DN 66 to DN 1400, depending on the function of the pipeline within the gas transmission network [59].

The coating governs the electrical exchange between the pipeline and the surrounding soil and is represented as a distributed pipe-to-soil impedance. An intact coating increases the insulation from ground, whereas degraded coating conditions or localized defects reduce the local impedance and create preferential current exchange points. For this reason, coating defects are critical for both AC interference and corrosion assessment, since induced AC currents and DC currents associated with cathodic protection may concentrate on the exposed metallic surface [60].

In the analysed compatibility studies, heavy bituminous coatings and three-layer polyethylene coatings are considered, with coating resistance values typically ranging from 10^3 to $10^5\ \Omega\,\mathrm{m}^2$. These values correspond to different insulation conditions and are translated into consistent assumptions for the equivalent pipe-to-soil impedance adopted in the model [60].

The soil provides the return path for dispersed currents and contributes to defining the pipeline impedance to ground. Soil electrical properties affect both the current exchanged at coating defects and the pipe-to-soil voltage profile along the route [55], [56]. However, soil resistivity should not be introduced as a fixed representative parameter of the pipeline system, since it is strongly dependent on the geographical location, local geological conditions and possible vertical stratification of the ground.

An indicative geographical distribution of ground electrical properties over the Italian territory can be obtained from the ITU-R P.832-3 world atlas of ground conductivities. The map reported in Figure 5.1 shows the effective ground-conductivity classes for Italy, expressed in $\mathrm{mS/m}$. Since resistivity is the inverse of conductivity, the conductivity classes shown in the map can be converted into the equivalent resistivity values reported in Table 5.1 [61].



Figure 5.1: Indicative geographical distribution of effective ground conductivity classes in Italy, extracted and graphically adapted in this work from ITU-R P.832-3 [61]. Conductivity values are expressed in mS/m.

Table 5.1: Conversion performed in this work of the effective ground-conductivity classes reported for Italy in ITU-R P.832-3 into equivalent resistivity values [61].

Ground conductivity σ [mS/m]	**Equivalent resistivity ρ[Ω m]**
0.3	≈ 3333
1	1000
3	≈ 333
10	100
30	≈ 33

These values should be interpreted as broad effective ground-conductivity classes rather than site-specific soil measurements. Nevertheless, they highlight that the electrical resistivity of the ground may vary by about two orders of magnitude across the Italian territory. In electromagnetic-interference studies, the soil resistivity must therefore be selected according to the local conditions of the investigated corridor and may be represented either by an equivalent homogeneous value or, when required, by a stratified soil model. The main pipeline and coating quantities required for the interference model are summarised in Table 5.2.

Table 5.2: Representative pipeline, coating and geometrical parameters used for electromagnetic interference modelling [55], [56], [59].

Parameter	**Typical / representative values**
Pipeline diameter	DN 66 – DN 1400 in Snam National Gas Pipeline Network documentation
Burial depth	Case-dependent; ≈ 1.5 m in the analysed interference cases
Exposed length	Case-dependent; 150 m to > 3000 m in the analysed interference cases
Coating type	Heavy bituminous coating; three-layer polyethylene in the analysed interference cases
Coating resistance	$10^3 - 10^5\ \Omega m^2$
Pipeline material / steel grade	Steel; grade case-dependent according to pipeline pressure class and project specification

In real systems, the pipeline may also belong to a wider network and may not be electrically independent. Metallic interconnections, branches, line facilities, valves, insulating joints and protection devices can modify the boundary conditions and allow induced voltages and currents to propagate beyond the sole parallel exposure section [52], [53]. These aspects define the electrical and geometrical properties of the interfered infrastructure and provide the input data required for the modelling phase.

5.2 Cathodic Protection, Measurement Points and Telecontrol Systems

Cathodic protection is the active system used to mitigate corrosion in buried metallic pipelines and defines the electrochemical state of the pipeline [62]. In gas transmission systems, it is generally implemented through rectifiers, distributed anodes, electrical connections to the pipeline and monitoring points [52], [53], [57].

In power-frequency interference analyses, cathodic protection does not usually require a detailed circuit representation, but it must be considered when interpreting the results. The induced AC component is superimposed on the DC polarization state of the pipeline, especially at coating defects, where AC current density, DC current density and pipeline polarization must be assessed together [63].

Measurement points and telecontrol systems are mainly relevant for monitoring and verification. They do not modify the interference mechanism, but may be used as comparison nodes with field data or as locations for checking pipe-to-soil voltage and possible touch-voltage conditions.

In the analysed interference cases, the most critical conditions are expected along parallel exposure sections, near grounding points and at coating defects, where AC interference, coating condition and cathodic protection state affect pipe-to-soil potential and local current density [63], [55], [56].

5.3 Insulating Joints, Surge Protection Devices and Accessible Parts

Insulating joints, surge protection devices, local grounding systems and accessible parts define important boundary conditions for the pipeline model. In electromagnetic interference studies, these elements are relevant because they introduce electrical discontinuities, voltage-limiting paths, local grounding connections and verification points along the pipeline [52], [53], [57].

Insulating joints provide electrical separation between pipeline sections and can be represented as high-impedance discontinuities in the longitudinal circuit. Under induced-voltage conditions, they may produce significant potential differences between the two sides of the joint. For this reason, the voltage across insulating joints is one of the quantities to be verified, especially under fault conditions [52], [53], [55], [56].

Surge protection devices associated with insulating joints limit overvoltages between pipeline sections or between the pipeline and ground. Under normal conditions, they remain open or highly resistive; when their triggering threshold is exceeded, they provide a low-impedance path. Their operation may therefore mitigate induced overvoltages, but it also introduces a temporary connection of the pipeline to ground or to another section of the network, modifying current distribution and pipe-to-soil potentials. When their contribution is included in the model, the resulting discharge

currents and absorbed energies must be checked against the device capabilities [34], [52], [55], [56], [57], [64].

Figure 5.2 schematically illustrates the main auxiliary elements of the interfered pipeline and the possible current return paths associated with electromagnetic interference.

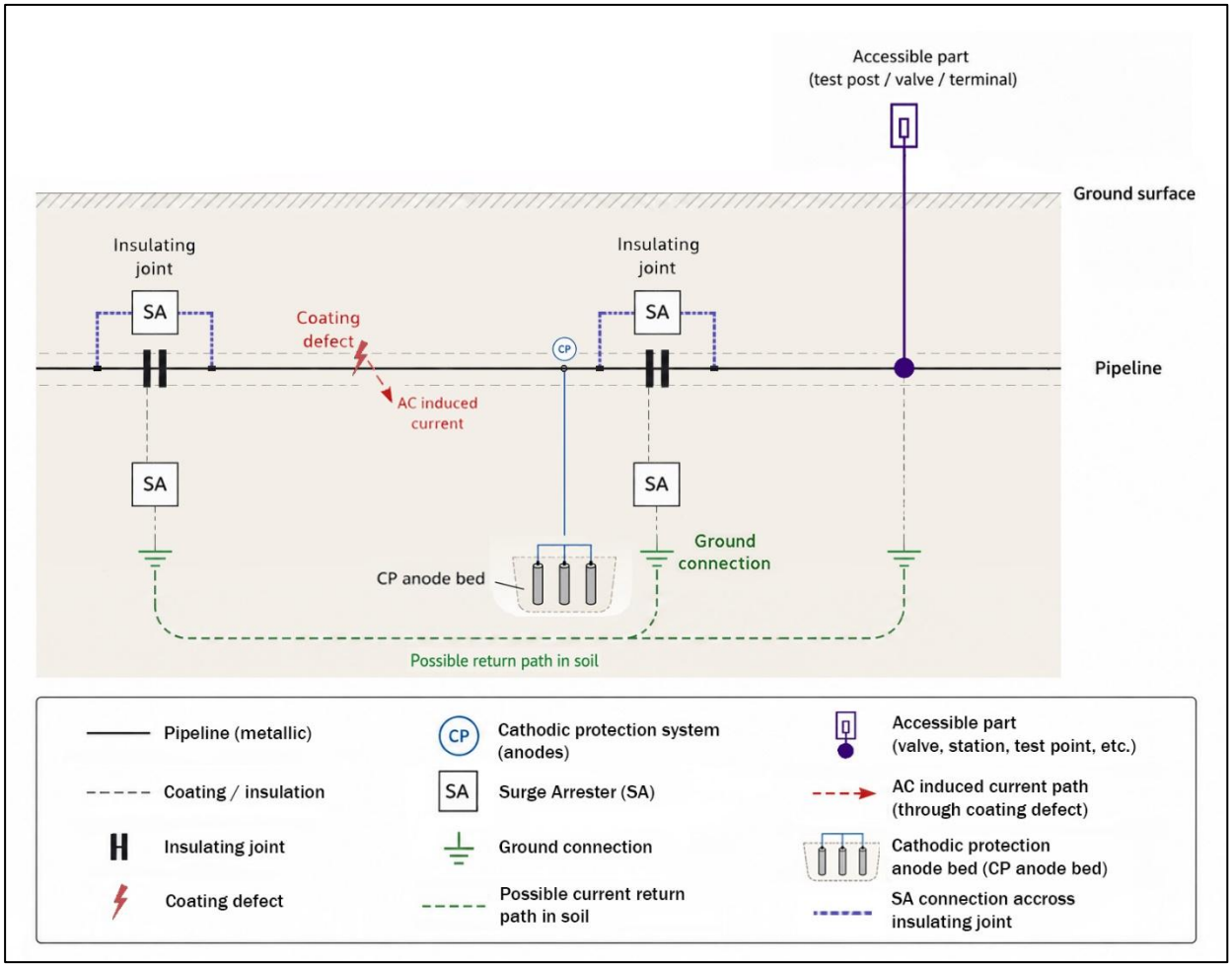


Figure 5.2: Schematic representation developed in this work of an interfered pipeline including insulating joints, surge arresters (SAs), cathodic protection system, grounding connections, accessible parts and a coating defect. The figure also highlights possible current return paths through the soil and the interaction between the pipeline and the surrounding environment under interference conditions.

The electrical configuration of the pipeline may consequently change between normal operation and fault or overvoltage conditions. For simulation purposes, it is therefore appropriate to distinguish between the normal configuration and the configuration with activated protection devices [34], [64].

Line facilities, stations, terminals and accessible parts, such as valves, pits, measurement points and local grounding connections, may locally constrain the pipeline potential and define points where touch-voltage checks are required. These locations are especially relevant near insulating joints, surge protection devices, grounding connections, cathodic protection facilities and areas affected by local GPR [53], [55], [56], [57].

A particularly severe touch-voltage condition may occur when the pipeline is well insulated from the soil and its electrical reference is imposed by cathodic-protection facilities or grounding points located far from the interference area. In this case, a local ground potential rise (GPR) caused by fault-current dissipation may raise the surrounding soil potential while the pipeline remains close to remote-earth potential. An accessible metallic part, such as a valve, test post or terminal, may therefore exhibit a significant voltage with respect to the local ground surface [55], [56].

For interference-modelling purposes, these elements must be translated into specific electrical conditions: longitudinal discontinuities, voltage-dependent nonlinear elements, local grounding connections and verification nodes with respect to local ground. Their representation allows the most stressed pipeline sections and nodes to be identified through pipe-to-soil voltages, joint voltages, touch voltages, local GPR and protection-device operation [54], [55], [56], [64].

5.4 Modelling Implications for the Interfered Infrastructure

In the simulation model, the pipeline is discretized along its route. Each section is assigned a longitudinal impedance and a distributed pipe-to-soil impedance associated with the coating [60].

Figure 5.3 shows the distributed-parameter representation adopted for the interfered pipeline, including longitudinal impedances, coating-to-ground coupling, insulating joints and localized coating defects.

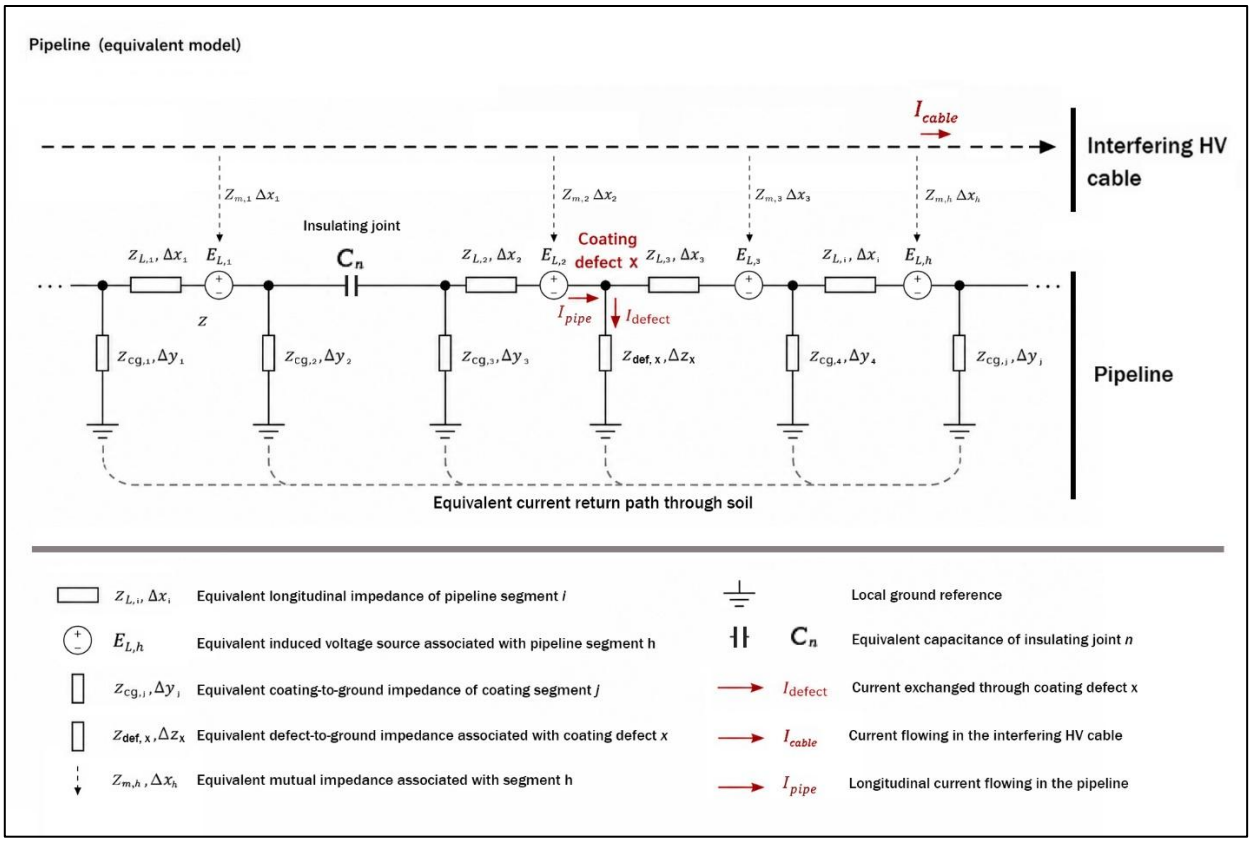


Figure 5.3: Distributed-parameter equivalent model developed in this work for an interfered buried pipeline including coating-to-ground coupling, insulating joints and localized coating defects.

The main input data for the model are the cable–pipeline geometry, parallel exposure length, pipeline discretization, longitudinal impedance, coating impedance, defect locations, insulating joints, protection devices, grounding conditions, terminal conditions and operating or fault currents of the interfering source. When surge protection devices are represented, their triggering voltage, residual voltage, current rating, energy withstand capability and connection scheme are also required. The soil is represented through its equivalent resistivity, which defines the ground-return path and affects pipe-to-soil voltage, dispersed current and local GPR.

The main output quantities are the longitudinal induced voltage, pipe-to-soil voltage, voltage across insulating joints, local GPR, AC current density at coating defects and the operating state of protection devices. If a surge protection device operates, the associated discharge current and absorbed energy must also be verified. These quantities allow the most critical sections and nodes of the pipeline to be identified for electrical safety and AC corrosion assessment.

Table 5.3 summarises the model inputs and verification quantities associated with the main elements of the interfered infrastructure.

Table 5.3: Elements of the interfered infrastructure relevant to electromagnetic interference modelling.

Element to be represented	**Required model data**	**Quantity to be verified**
Metallic pipeline	Route, burial depth, exposed length, diameter, wall thickness, longitudinal impedance	Longitudinal induced voltage, induced current, potential profile
Insulating coating	Equivalent pipe-to-soil impedance/resistance, coating condition	Pipe-to-soil voltage, dispersed current
Coating defects	Position, exposed area, local defect impedance	$J_{DC}, J_{AC}, J_{AC}/J_{DC}$, corrosion risk
Cathodic protection	Polarization condition, injection/measurement points	ON/OFF potential, IR-free potential
Insulating joints	Position, electrical condition, equivalent impedance	Voltage across the joint
Surge protection devices	Trigger threshold, residual voltage, current rating, energy withstand capability, position and connection scheme	Limited voltage, operating state, discharge current and absorbed energy
Local grounding systems and line facilities	Position, grounding resistance, equipotential connections	Local GPR, touch voltage, pipe-to-soil voltage
Accessible parts and measurement points	Valves, pits, test posts, terminals	Touch voltage, local pipe-to-soil voltage
Soil	Equivalent or stratified resistivity	Ground-return path, GPR, dispersed current

6. ELECTROMAGNETIC MODELLING OF CABLE–PIPELINE SYSTEMS

After describing the physical structure of underground cables, metallic pipelines and their possible interference mechanisms, this chapter introduces the mathematical framework used to model the cable–pipeline interaction. The corridor is represented through distributed-parameter equations, impedance and admittance matrices, and earth-return mutual-impedance formulations. Finally, the implementation of the model in ATP-EMTP is discussed, and a numerical verification of the adopted earth-return impedance formulation is performed in this work by comparing the Pollaczek reference formulation with the Ametani/ATP approach and the compact Wedepohl approximation.

6.1 Modelling Approach and Distributed-Parameter Representation

The cable–pipeline system is modelled as a multi-conductor distributed-parameter network. In this representation, each conductive element of the corridor is associated with a voltage and a current varying along the longitudinal coordinate x. The model may include phase conductors, metallic sheaths, earth continuity conductors, grounding conductors and the interfered pipeline. The electrical behaviour of the system is described by the following transmission-line equations:

$$\frac{d[\bar{V}]}{dx} = -[\dot{Z}][\bar{I}] \tag{6.1}$$

$$\frac{d[\bar{I}]}{dx} = -[\dot{\mathrm{Y}}][\bar{\mathrm{V}}] \tag{6.2}$$

where:

- $[\bar{V}]$: the vector of conductor voltages with respect to the reference potential $[V]$;
- $[\bar{I}]$: the vector of conductor currents $[A]$;
- x: the longitudinal coordinate along the considered route $[m]$;
- $[\dot{Z}]$: the per-unit-length impedance matrix of the multi-conductor system $[\Omega/m]$;
- $[\dot{Y}]$: the per-unit-length admittance matrix of the multi-conductor system $[S/m]$;
- $\frac{d[\bar{\mathrm{V}}]}{dx}$: the longitudinal voltage gradient along the conductors $[V/m]$;
- $\frac{d[\bar{I}]}{dx}$: the longitudinal current variation along the conductors $[A/m]$.

The matrix $[\dot{Z}]$ contains the longitudinal self and mutual impedances of the conductors, including internal conductor effects and earth-return contributions. The matrix $[\dot{Y}]$ describes the transverse capacitive coupling between conductors and the reference medium [12].

In this thesis, the cable–pipeline interaction is mainly governed by the off-diagonal terms of $[\dot{Z}]$, which represent the mutual coupling between the interfering cable system and the pipeline. For this reason, the following sections first define the cable impedance and admittance matrices, then focus on the earth-return and mutual-impedance terms used for induced-voltage assessment.

A detailed derivation of the internal impedances of single-core cables is outside the scope of this thesis, since these terms have limited influence on the cable–pipeline electromagnetic induction. The following analysis therefore focuses on the earth-return mutual impedance.

6.2 Ametani Formulation for Underground Cable Systems

Ametani's formulation describes cable systems through per-unit-length impedance and admittance matrices. The formulation is general and can be applied to single-core coaxial cables, cables including core, sheath and armour, pipe-type cables and overhead cable configurations. In this work, it is used for the representation of conventional underground single-core HV cables.

Before introducing the matrices, the main assumptions of the formulation are recalled. Each conducting medium is assumed to have constant magnetic permeability. In addition, for pipe-type cables, the pipe thickness is assumed to be greater than the penetration depth of the pipe wall. Since the systems considered in this thesis are not pipe-type cables, this last assumption is not directly involved in the reduced model adopted here.

6.2.1 Series-Impedance Matrix: Internal and Earth-Return Contributions

The longitudinal impedance matrix can be evaluated according to the following general equation:

$$[\dot{Z}] = [\dot{Z}_i] + [\dot{Z}_p] + [\dot{Z}_c] + [\dot{Z}_0] \tag{6.3}$$

where:

- $[\dot{Z}_i]$: the internal impedance matrix of the cable conductors, [Ω/m];
- $[\dot{Z}_p]$: the contribution of metallic enclosures or pipe-type structures, when present, [Ω/m];
- $[\dot{Z}_c]$: the matrix taking into account for coupling between internal and external conductive regions, [Ω/m];
- $[\dot{Z}_0]$: the impedance associated with the external medium and earth-return currents, [Ω/m].

For conventional single-core underground cables without pipe enclosure, the pipe-related terms are not present. Therefore, the impedance matrix reduces to:

$$[\dot{Z}] = [\dot{Z}_i] + [\dot{Z}_0] \tag{6.4}$$

This reduced form separates the internal cable contribution from the external-medium contribution. In the present application, $[\dot{Z}_0]$ is particularly relevant because it contains the earth-return terms responsible for the mutual coupling between overhead or underground cables.

A relevant aspect of Ametani's formulation is the block structure of the impedance matrix. The terms appearing in the global matrix are not necessarily scalar quantities; rather, they can be submatrices $[\dot{Z}_{0,ij}]$, whose dimensions are:

- 3×3 for cable with core, screen and armour conductors;
- 2×2 for cable with core and screen conductors;
- 1×1 for cable with only core conductor, overhead line conductor or pipeline;

According to the consideration above, the longitudinal matrix $[\dot{Z}_0]$ can be written as:

$$[\dot{Z}_0] = \begin{bmatrix} [\dot{Z}_{0,11}] & [\dot{Z}_{0,12}] & \cdots & [\dot{Z}_{0,1m}] \\ [\dot{Z}_{0,21}] & [\dot{Z}_{0,22}] & \cdots & [\dot{Z}_{0,2m}] \\ \vdots & \vdots & \ddots & \vdots \\ [\dot{Z}_{0,m1}] & [\dot{Z}_{0,m2}] & \cdots & [\dot{Z}_{0,mm}] \end{bmatrix} \tag{6.5}$$

being m the number of cables, overhead line and pipeline involved in the electromagnetic problem. The net current in the i-th cable returning through the soil, i.e. the algebraic sum of the core, screen and armour currents, gives rise to a voltage drop in the soil adjacent to the j-th cable. This voltage drop gives the e.m.f. induced into each conductor of this cable; i.e. the same e.m.f. is induced in both conductors. It follows from these remarks that all elements of the submatrix $[\dot{Z}_{0,ij}]$ must be equal:

$$[\dot{Z}_{0,ij}] = \dot{Z}_{0ij} \cdot [\mathbf{1}] \tag{6.6}$$

being:

- $[\mathbf{1}]$: the ones matrix of 3×3 for cable with core, screen and armour conductors, 2×2 for cable with core and screen conductors and 1×1 for cable with only core conductor, overhead line conductor or pipeline, $[pu]$;
- $\dot{Z}_{0ij}$: the earth return impedance between i-th and j-th cables according to Pollaczek or Carson equations, [Ω/m].

The internal contribution $[\dot{Z}_i]$ is assembled from diagonal submatrices associated with the individual single-core cables:

$$[\dot{Z}_i] = \begin{bmatrix} [\dot{Z}_{i1}] & [0] & \cdots & [0] \\ [0] & [\dot{Z}_{i2}] & \cdots & [0] \\ \vdots & \vdots & \ddots & \vdots \\ [0] & [0] & \cdots & [\dot{Z}_{im}] \end{bmatrix} \tag{6.7}$$

being $[\dot{Z}_{ij}]$ the diagonal submatrix expressing the self-impedance matrix of the j-th single-core cable, [Ω/m].

The off-diagonal blocks of $[\dot{Z}_i]$ are zero because the internal impedance terms describe the electromagnetic behaviour within each cable. The coupling between different cables is instead represented by the earth-return blocks of $[\dot{Z}_0]$.

In the general core–sheath–armour case, each diagonal submatrix has dimension 3×3. Since the HV XLPE cables considered in this work are represented by core and metallic sheath only, the submatrix of the j-th cable reduces to

$$[\dot{Z}_{ij}] = \begin{bmatrix} \dot{Z}_{ccj} & \dot{Z}_{csj} \\ \dot{Z}_{csj} & \dot{Z}_{ssj} \end{bmatrix} \tag{6.8}$$

where:

- $\dot{Z}_{ccj}$: the self-impedance of the core conductor of the j-th cable, [Ω/m];
- $\dot{Z}_{ssj}$: the self-impedance of the metallic sheath of the j-th cable, [Ω/m];
- $\dot{Z}_{csj}$: the mutual impedance between the core conductor and the metallic sheath of the j-th cable, [Ω/m].

The internal impedance matrix $\left[\dot{Z}_{ij}\right]$ accounts for the magnetic field stored within the conductive media (core, screen, and armour) as well as the insulating medium of each cable. Due to skin effect phenomena in the conductive media, the inductive components of the internal impedance exhibit a nonlinear dependence on frequency. The same considerations apply to the zero-sequence impedance $\left[\dot{Z}_0\right]$ [12].

6.2.2 Potential-Coefficient and Admittance Matrix

The transverse admittance matrix $\left[\dot{Y}\right]$ accounts for the electric field stored within the insulating medium of each cable; it is obtained from the potential-coefficient matrix $[P]$ as

$$\left[\dot{Y}\right] = j\omega[P]^{-1} \tag{6.9}$$

where:

- $\left[\dot{Y}\right]$: the per-unit-length admittance matrix, [S/m]
- $[P]$: the potential-coefficient matrix, [m/(F)];
- ω: the angular frequency, [rad/s].

The potential-coefficient matrix is written in the general form

$$[P] = [P_i] + \left[P_p\right] + [P_c] + [P_o] \tag{6.10}$$

where:

- $[P_i]$: the internal potential-coefficient matrix associated with the cable conductors [m/F];
- $[P_p]$: pipe internal potential coefficient matrix [m/F];
- $[P_c]$: potential coefficient matrix between pipe inner and outer surfaces [m/F];
- $[P_o]$: potential coefficient matrix of the pipe in air [m/F].

For conventional underground single-core cables without pipe enclosure, the formulation reduces to

$$[P] = [P_i] \tag{6.11}$$

The internal potential-coefficient matrix is assembled as

$$[P_i] = \begin{bmatrix} [P_{i1}] & [0] & \cdots & [0] \\ [0] & [P_{i2}] & \cdots & [0] \\ \vdots & \vdots & \ddots & \vdots \\ [0] & [0] & \cdots & [P_{im}] \end{bmatrix} \tag{6.12}$$

where:

- $[P_i]$: the internal potential-coefficient matrix of the cable system, [m/F];
- $[P_{ij}]$: the potential-coefficient submatrix associated with the j-th cable, [m/F];

For the reduced core–sheath representation, the potential-coefficient submatrix of the j-th cable is

$$[P_{ij}] = \begin{bmatrix} P_{cj} + P_{sj} & P_{sj} \\ P_{sj} & P_{sj} \end{bmatrix} \tag{6.13}$$

where:

- P_{cj}: the potential coefficient associated with the insulation region between core and sheath of the j-th cable, [m/F];
- P_{sj}: the potential coefficient associated with the insulation region outside the sheath of the j-th cable, [m/F].

The admittance matrix completes the multiconductor representation of the cable system. However, for the cable–pipeline interference analysed in this thesis, the dominant coupling mechanism is inductive.

For this reason, the following analysis focuses mainly on the series-impedance matrix and on the mutual terms of $[\dot{Z}_0]$ [12].

6.2.3 Mutual Earth-Return Impedance Formulations

The matrix $[\dot{Z}_0]$ introduced in the previous section represents the contribution of the external medium. In underground installations, this contribution is mainly associated with earth-return currents and is responsible for the electromagnetic coupling between buried conductors.

Therefore, the mutual terms of $[\dot{Z}_0]$ are the quantities required to evaluate the induced voltage on a nearby metallic pipeline. For buried conductors, the reference formulation is given by Pollaczek. In a general form, the mutual earth-return impedance between two conductors can be expressed as [12]:

$$\dot{Z}_{0ij} = \frac{j\omega\mu_e}{2\pi}\left[K_0(m_e d_{ij}) - K_0(m_e D_{ij}) + \int_{-\infty}^{+\infty} \frac{e^{-(h_i+h_j)\sqrt{\alpha^2+m_e^2}}}{|\alpha| + \sqrt{\alpha^2+m_e^2}} e^{j\alpha x_{ij}} d\alpha\right] \tag{6.14}$$

with

$$m_e = \sqrt{j\omega\mu_e/\rho_e}$$
$$d_{ij} = \sqrt{x_{ij}^2 + (h_i - h_j)^2}, \qquad D_{ij} = \sqrt{x_{ij}^2 + (h_i + h_j)^2} \tag{6.15}$$

The main geometrical quantities involved are shown in Figure 6.1.

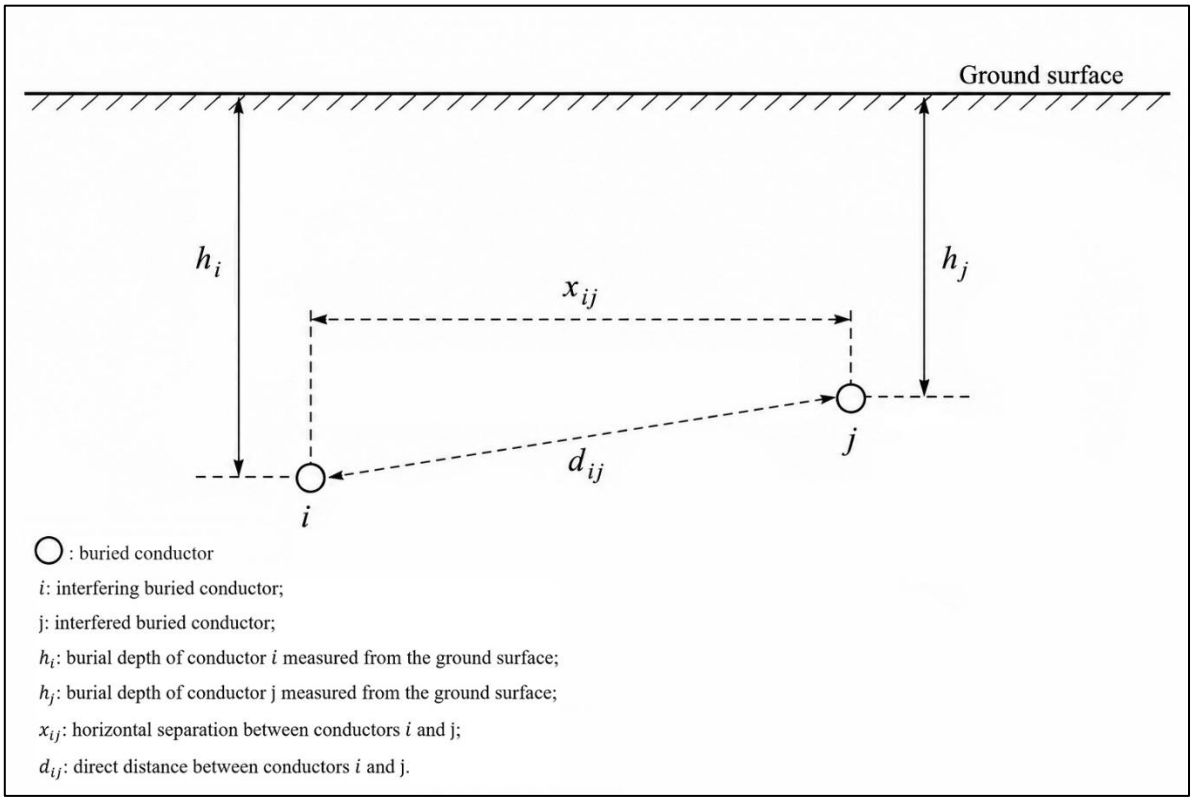


Figure 6.1: Geometrical definition developed in this work for two buried conductors, showing the burial depths h_i and h_j, the horizontal separation x_{ij}, and the direct distance d_{ij}.

Where:

- $\dot{Z}_{0ij}$: the mutual earth-return impedance per unit length, [Ω/m];
- m_e: the soil propagation coefficient, [1/m];
- μ_e: the magnetic permeability of the soil ($\mu_e = \mu_0$), [H/m];
- μ_0: the permeability of free space, [H/m];
- ρ_e: soil resistivity, [Ωm];
- α: the integration variable, [1/m];
- K_0: the modified Bessel function of the second kind and order zero, [pu];
- d_{ij}: the Euclidean distance between i-th and j-th cables, [m];
- D_{ij}: the Euclidean distance between i-th cable and the image of j-th cable, [m];
- h_i, h_j: the burial depths of conductors i and j, [m].

- x_{ij}: the horizontal separation between the conductors, [m];

Although Pollaczek's formulation provides a rigorous representation of the mutual earth-return impedance, its direct evaluation requires the computation of an infinite integral; it is argued that the series solution is rather complicated and it is better that the impedance is obtained numerically. For this reason, approximate expressions are commonly adopted in engineering calculations and EMTP-type implementations.

A simplification of Pollaczek's integral has been proposed by Ametani and is adopted in Cable Constant library of ATP-EMTP software. Ametani recognised that the integrand becomes identical with Carson's earth impedance if $|\alpha| \gg |m_e|$ [12], [65]:

$$e^{-(h_i+h_j)\sqrt{\alpha^2+m_e^2}} = e^{-(h_i+h_j)|\alpha|}$$

Therefore, the integral term can be evaluated using the well-known infinite series of Carson integral.

At very low frequencies, Ametani et al. proposed a further simplification [12], [65], obtained in the power-frequency range by assuming

$$|h_e| = \sqrt{\frac{\rho_e}{\omega\mu_0}} \approx \sqrt{\frac{\rho_e}{8f}} \cdot 10^3 \gg 1 \tag{6.16}$$

where:

- h_e is the equivalent earth penetration depth, [m];
- ρ_e is the soil resistivity, [Ωm];
- f is the system frequency, [Hz].

Under this condition, the approximate expression proposed by Ametani et al. and Lucca's formula become nearly coincident. The mutual earth-return impedance can then be written as

$$\dot{Z}_{0ij} \approx f + j\left[8.253 + 0.628\, ln\left(\frac{\rho_e}{f d^2}\right)\right] \tag{6.17}$$

being d the separation distance between the two conductors, [m]. For compactness, the unit-conversion factors required for dimensional consistency are omitted, as they are numerically equal to unity in the adopted units and do not affect the calculated value.

This expression is, therefore, not used as a general form of Pollaczek's impedance, but as a compact low-frequency approximation. In the present work, it is useful as a reference engineering formula for power-frequency cable–pipeline interference calculations.

A further simplified formulation is the Wedepohl approximation, which gives a compact expression for the same scalar mutual earth-return impedance $\dot{Z}_{0ij}$. For sufficiently small values of the dimensionless parameter $|m_e d| < 0.25$, the mutual impedance can be approximated as [6]:

$$\dot{Z}_{0ij} = \frac{j\omega\mu_e}{2\pi}\left[-\ln\left(\frac{e^{\gamma_E} m_e d}{2}\right) + \frac{1}{2} - \frac{2}{3} m_e\left(h_i + h_j\right)\right] \tag{6.18}$$

where γ_E is the Euler–Mascheroni constant.

For higher values of $|m_e d|$, the compact expression is no longer directly applicable and the corresponding integral formulation should be used. In this work, the Wedepohl approximation is retained as an additional engineering model to be compared with the Pollaczek reference formulation and the low-frequency approximation discussed above.

Once the mutual coupling term $\dot{Z}_{0ij}$ has been determined, the induced voltage $\bar{E}_{ind}$ on a pipeline can be evaluated according to the following equation:

$$\bar{E}_{ind} = \dot{Z}_{0ij} L \bar{I} \tag{6.19}$$

being L the length of pipeline [m] and $\bar{I}$ the equivalent inducing current flowing in the interfering cable system, [A].

6.3 Comparison of earth-return impedance formulations

The focus of this section is the evaluation of the mutual earth-return impedance, since this is the parameter directly involved in the inductive coupling between the cable system and the pipeline. A numerical comparison is carried out among the Pollaczek reference formulation, the Ametani approximation implemented in the ATP-EMTP Cable Constants routine, and the Wedepohl approximation.

6.3.1 Frequency-dependent comparison of Pollaczek, Ametani and Wedepohl formulations

The numerical verification is based on a simplified two-buried-conductor configuration. The objective is not to reproduce the complete electromagnetic behaviour of the cable–pipeline system, but to compare the mutual earth-return impedance obtained from different formulations under the same geometrical and soil conditions.

The following assumptions are adopted:

- The soil is represented as an equivalent homogeneous and non-magnetic medium.
- The cable system and the pipeline are represented by two parallel buried conductors, with fixed burial depths and horizontal separation.
- The comparison is performed in the frequency domain and refers to the mutual earth-return impedance per unit length.
- End effects, coating impedance, cathodic protection, grounding discontinuities and finite-length boundary conditions are not included at this stage, since they do not affect the comparison between the earth-return impedance formulations.

A representative input set is defined in Table 6.1. The adopted values are derived from typical Terna–Snam electromagnetic-compatibility case studies involving high-voltage underground cable systems and nearby buried metallic pipelines [55], [56].

Table 6.1: Input parameters adopted for the mutual earth-return impedance verification.

Parameter	***Symbol***	***Adopted value / range***
Frequency range	f	$10^{-2} - 10^{7}$ Hz
Power frequency	f_0	50 Hz
Equivalent homogeneous soil resistivity	ρ_e	200 Ωm
Soil magnetic permeability	μ_e	$\mu_0 = 4\pi \cdot 10^{-7}$ H/m
Cable burial depth	h_i	1.6 m
Pipeline burial depth	h_j	1.5 m
Horizontal separation	$x_{ij,0}$	10 m
Parallel exposure length	L	2000 m
Pipeline diameter	DN	DN 150
Pipeline material	–	Steel
Cable arrangement	–	Single 380 kV HVAC cable circuit, three single-core cables

For each frequency value, the Pollaczek formulation is first evaluated and used as the reference result. The corresponding values obtained from the Ametani/ATP formulation and from the Wedepohl compact approximation are then compared with this reference. The comparison is carried out on the complex mutual impedance per unit length, by analysing separately its resistive component and equivalent inductive component.

The resulting deviations are used to assess whether the simplified formulations remain sufficiently close to the Pollaczek reference within the frequency range of interest. The results of the numerical comparison are reported in Figure 6.2 and Figure 6.3, while the corresponding quantitative error values are summarised in Table 6.2.

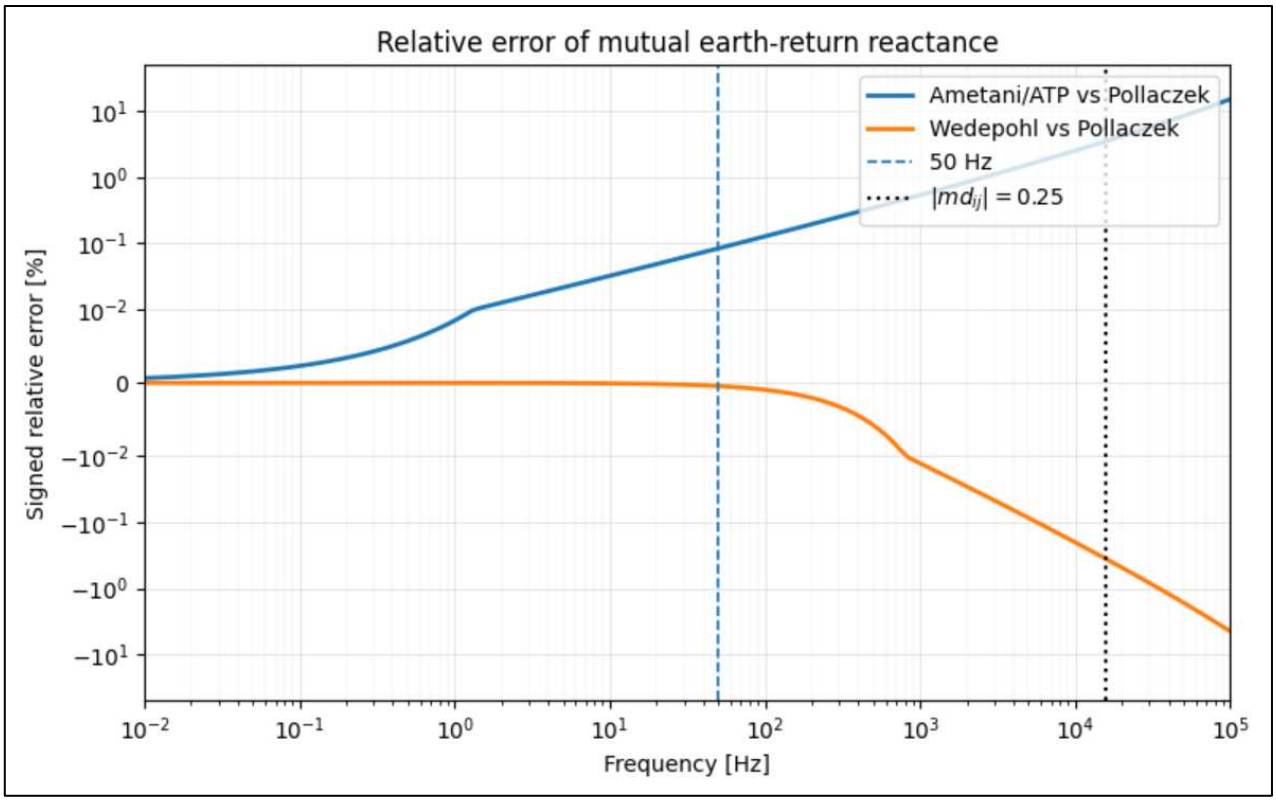


Figure 6.2: Relative error of the equivalent inductive component of the mutual earth-return impedance, computed in this work with respect to the Pollaczek reference formulation.

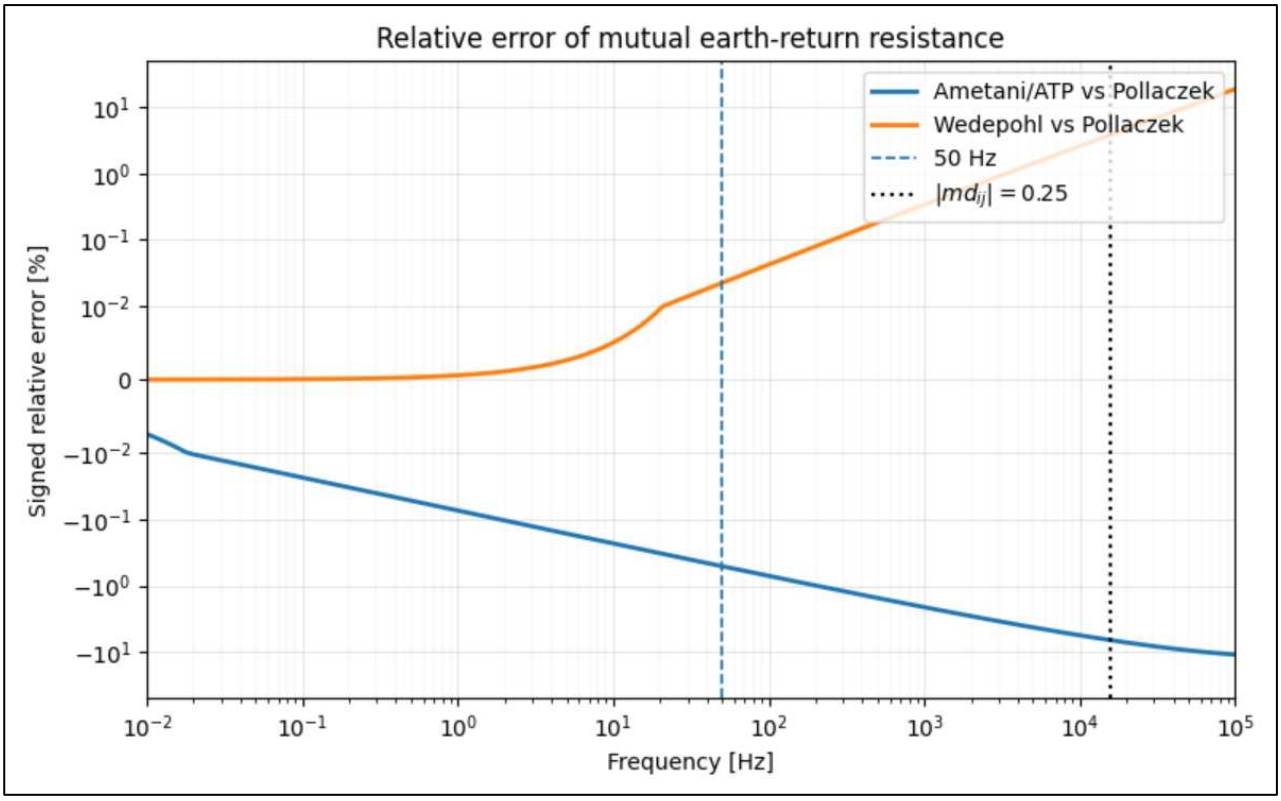


Figure 6.3: Relative error of the resistive component of the mutual earth-return impedance, computed in this work with respect to the Pollaczek reference formulation.

The quantitative error values reported in Table 6.2 support the graphical results for the selected case.

Table 6.2: Summary of the relative errors computed in this work for the mutual earth-return impedance verification. Negative values indicate an underestimation with respect to the Pollaczek reference.

Formulation	**Error R_m at 50 Hz [%]**	**Error L_m at 50 Hz [%]**	**Max. $\lvert \varepsilon_R \rvert$ for $\lvert m_e d_{ij} \rvert < 0.25$ [%]**	**Max. $\lvert \varepsilon_L \rvert$ for $\lvert m_e d_{ij} \rvert < 0.25$ [%]**	**f at max. $\lvert \varepsilon_R \rvert$ and $\lvert \varepsilon_L \rvert$ [Hz]**
Ametani/ATP	-0.522	0.084	6.589	3.456	15288
Wedepohl	0.023	≈ 0.000	3.766	0.344	15288

At 50 Hz, both simplified formulations show limited deviations from the Pollaczek reference. Over the range satisfying $\left|m_e d_{ij}\right| < 0.25$, the maximum errors remain moderate, with the Wedepohl approximation showing particularly small deviations in the inductive component. This indicates that, for the representative configuration considered, both simplified formulations are sufficiently close to the Pollaczek reference for the purpose of the present mutual-impedance verification.

To extend the verification beyond the single representative configuration, an additional parametric analysis was carried out at the reference power frequency. The mutual earth-return impedance was evaluated as a function of the horizontal separation between the buried conductors, for different values of soil resistivity. This allows the behaviour of the considered formulations to be assessed under low-frequency conditions representative of the applications addressed in this work, while also accounting for the variability of the main geometrical and soil parameters. The results are shown in Figure 6.4.

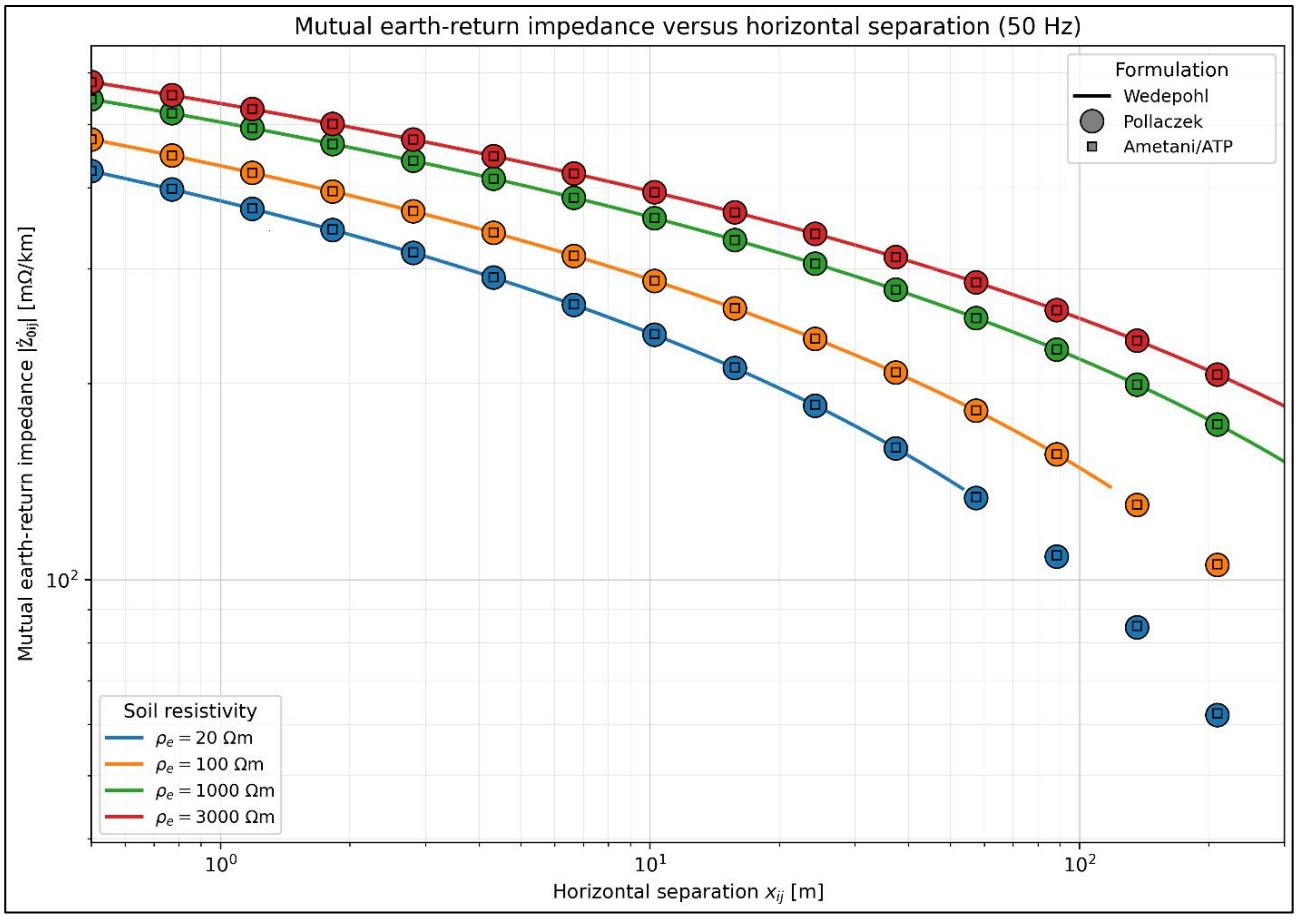


Figure 6.4: Mutual earth-return impedance versus horizontal separation for different soil resistivity values, developed in this work. Pollaczek, Ametani/ATP and Wedepohl formulations are compared.

The results show that the Pollaczek reference formulation, the Ametani/ATP and Wedepohl compact approximations provide very similar trends at 50 Hz. In particular, the Ametani/ATP formula results remain very close to the Pollaczek ones over the analysed range, confirming the consistency of the approximation adopted in EMTP-type cable-constant routines. At the same time, within the range where the Wedepohl validity condition is satisfied, the continuous Wedepohl curves are also practically superimposed on the corresponding Pollaczek and Ametani/ATP results.

This confirms that, for the analysed power-frequency cases, both simplified formulations can be used to estimate the mutual earth-return impedance with limited loss of accuracy. The Ametani/ATP approximation is particularly relevant for the numerical cable model, since it is consistent with the approach adopted in EMTP-type implementations. The Wedepohl formulation, instead, provides a more compact analytical expression of $\dot{Z}_{0ij}$, avoiding the direct numerical evaluation of the Pollaczek integral. Therefore, when the geometrical and soil conditions fall within the verified range, both simplified approaches are suitable for estimating the mutual coupling between the cable system and the pipeline.

6.3.2 Parametric assessment of mutual earth-return impedance formulations

A comparative assessment was carried out to evaluate the mutual earth-return impedance obtained from the formulations introduced in the previous sections. The comparison was performed using the Pollaczek formulation as reference.

The analysed configuration considers a buried cable and a buried pipeline with fixed installation depths, while the soil resistivity ρ_e and the horizontal separation x_{ij} are varied over a representative range of values. In this way, the comparison covers both close and distant cable–pipeline configurations, as well as low- and high-resistivity soil conditions. The input data used for the comparison are reported in Table 6.3.

Table 6.3: Input data adopted for the comparison of mutual earth-return impedance formulations.

Parameter	***Symbol / setting***	***Adopted value***
LCC system representation	-	Two equivalent buried conductors
ATP-EMTP LCC model setup	-	Homogeneous ground, PI model, one section
Section length	L_{LCC}	2000 m
Frequency	f	50 Hz
Soil resistivity	ρ_e	$20, 50, 100,200,500,1000,2000,3000\ \Omega$m
Cable-side conductor depth	h_i	1.6 m
Pipeline-side conductor depth	h_j	1.5 m
Horizontal separation	x_{ij}	1,2,5,10,20,30,50,100,200 m
Cable-side equivalent conductor radius	r_{cab}	0.01 m
Pipeline-side metallic equivalent radius	r_p	0.084 m
Cable-side conductor resistivity	ρ_i	$1.68 \times 10^{-8}\ \Omega$m
Pipeline-side conductor resistivity	ρ_j	$1.72 \times 10^{-7}\ \Omega$m
Relative magnetic permeability	μ_r	1

The pipeline was represented in LCC as an equivalent buried metallic conductor. Only the metallic conductor and the surrounding homogeneous soil are considered in this verification; coating impedance, cathodic protection, insulating joints and finite-length boundary conditions are not included, since the objective is limited to the comparison of mutual earth-return impedance formulations.

For each combination of ρ_e and x_{ij}, the mutual impedance obtained from the following methods was compared with the Pollaczek reference:

- Ametani/ATP impedance, extracted from the off-diagonal terms of the impedance matrix generated by the ATP-EMTP Line/Cable Constants routine;
- CIGRE/Carson-Clem approximation, taken from the CIGRE formulation for mutual impedance with earth return [3];
- CIGRE/Haberland approximation, taken from the same CIGRE set of earth-return impedance approximations [3];
- ITU-T K.68 screening formulation, based on the polynomial approximation used for preliminary inductive-coupling assessments [7];
- Wedepohl approximation [6].

When the formulation provides a complex impedance, both the real and imaginary parts were evaluated. However, the main comparison was based on the magnitude $|\dot{Z}_{0ij}|$, since this is the quantity directly used to assess the strength of the inductive coupling in the screening analysis. For formulations defined only in terms of magnitude, namely CIGRE/Haberland and ITU-T K.68, only $|\dot{Z}_{0ij}|$ was considered.

For CIGRE/Carson-Clem and Wedepohl, the statistical comparison was limited to the points satisfying the corresponding validity conditions. Points outside the formal validity range were excluded from the error indicators and explicitly marked in the error maps. This allows the comparison to distinguish between the accuracy of each formulation and its actual range of applicability. The results of the comparison are summarised in Table 6.4.

Table 6.4: Summary of the relative errors of the considered formulations with respect to the Pollaczek reference for the mutual impedance magnitude $|\dot{Z}_{0ij}|$.

Method	**Valid points**	**MAPE [%]**	**Median error [%]**	**95th percentile [%]**	**Maximum error [%]**	**Applicability**
Wedepohl	66/72	0.005	< 0.001	0.025	0.088	Only where $\mid m_e d_{ij} \mid < 0.25$
CIGRÉ/Carson–Clem	66/72	0.032	0.010	0.112	0.226	Only where $d_{ij} \leq 90\sqrt{\rho_e/f}$
ITU-T K.68	72/72	0.070	0.066	0.140	0.450	All points
Ametani/ATP	72/72	0.103	0.058	0.318	0.555	All points
CIGRÉ/Haberland	72/72	1.884	1.949	2.173	4.955	All points

Errors are calculated with respect to the Pollaczek formulation. For Wedepohl and CIGRE/Carson-Clem, only the points satisfying the respective validity conditions are included in the statistical indicators.

The spatial distribution of the error over the investigated $\rho_e - x_{ij}$ grid is shown in Figure 6.5. The figure reports the relative error of $|\dot{Z}_{0ij}|$ for each formulation with respect to Pollaczek.

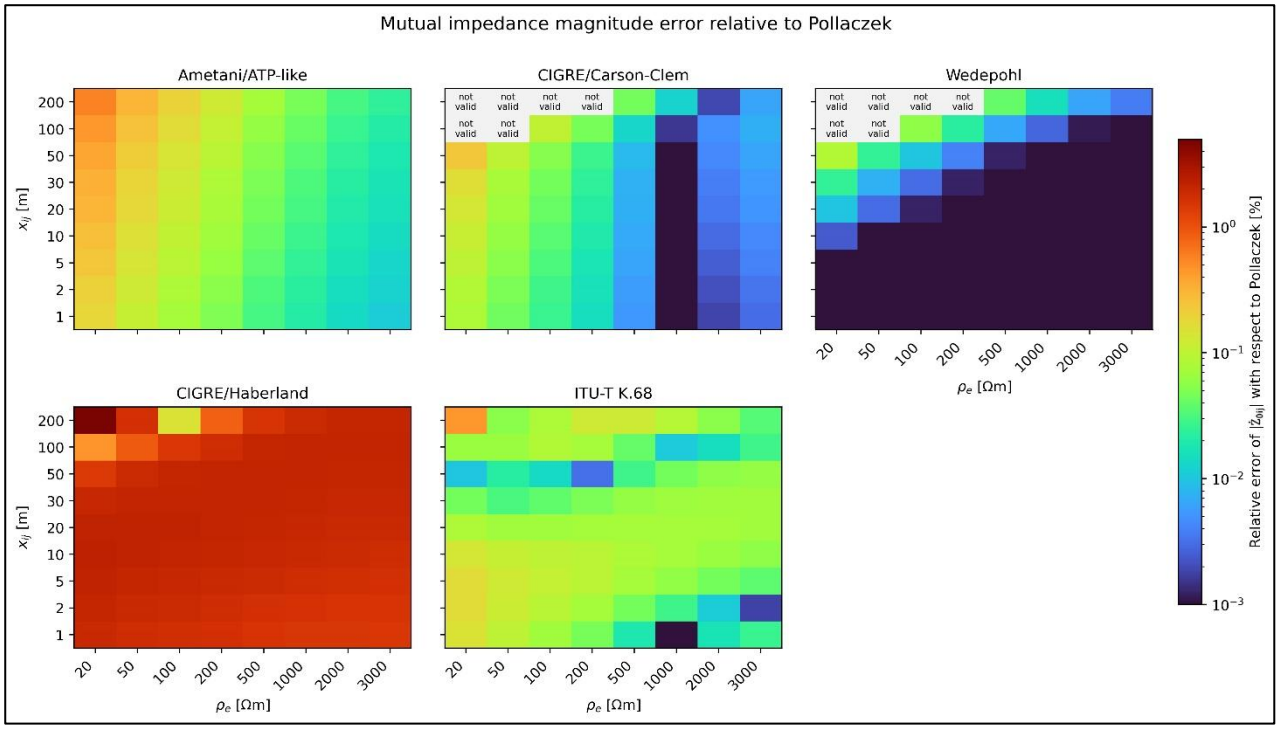


Figure 6.5: Relative error of the mutual impedance magnitude $|\dot{Z}_{0ij}|$ with respect to the Pollaczek reference for the considered formulations, developed in this work. The colour scale is logarithmic to improve the readability of both low- and high-error regions.

Grey cells marked as “not valid” indicate configurations outside the formal applicability range of the corresponding approximation and were therefore excluded from the statistical indicators in Table 6.4.

The comparison shows that the mutual earth-return impedance obtained from the considered formulations is consistent with the Pollaczek reference over the analysed range. The lowest errors are obtained with Wedepohl and CIGRE/Carson-Clem, provided that the corresponding validity conditions are satisfied. This aspect is relevant from an engineering point of view, since these formulations can provide accurate estimates, but their use must remain limited to the parameter range for which the underlying approximations are valid.

The Ametani/ATP-like results show low deviations from the Pollaczek reference over the whole analysed grid. This confirms that the off-diagonal terms extracted from the ATP-EMTP LCC impedance matrix are consistent with the analytical earth-return impedance and can be used as a numerical basis for the subsequent cable–pipeline simulations.

The ITU-T K.68 formulation also provides limited errors on the impedance magnitude over the full set of analysed configurations. This confirms its suitability for preliminary screening calculations, where the objective is to obtain a computationally simple estimate of the inductive coupling. CIGRE/Haberland gives the largest deviations among the considered methods, although the

maximum error remains limited. This result is consistent with its nature as a compact wide-range approximation of the impedance magnitude, rather than a complete complex formulation.

Overall, the comparison supports the use of Pollaczek as the analytical reference and of the Ametani/ATP model as the numerical implementation adopted in ATP-EMTP. The simplified screening formulations remain useful for preliminary assessments, provided that their validity limits and approximation level are explicitly considered.

7. REGULATORY FRAMEWORK AND ACCEPTANCE CRITERIA

The assessment of electromagnetic interference in Italy is primarily governed by CEI EN 50443, which establishes the criteria for ensuring both the integrity of the affected infrastructure and the safety of personnel. The standard specifies the admissible limits for induced and touch voltages under both steady-state and fault conditions. However, the analytical procedures for evaluating interference mechanisms, including inductive, capacitive, and conductive coupling, are not developed within the standard itself but are instead derived from CIGRE Technical Brochures and ITU recommendations. Consequently, CEI EN 50443 provides the acceptance framework, whereas CIGRE and ITU documents constitute the main technical references for the modelling and calculation of interference effects.

It should be noted that CEI EN 50443 does not specify limits for the transverse current density in pipelines, despite its relevance to AC-corrosion mechanisms. The standard focuses on induced and touch voltage limits for infrastructure protection and personnel safety. Consequently, the assessment of corrosion-related effects requires reference to sector-specific UNI standards and to the recommendations provided in the relevant CIGRE publications.

It should also be noted that the voltage limits established by CEI EN 50443 are intended to ensure the protection of personnel working on the pipeline and of the equipment connected to it. When conductive parts are accessible to the general-public, different safety criteria should be considered. In this context, the touch-voltage safety curves provided in CEI EN 50522 can be used as a reference for the assessment of electrical safety conditions.

The main references considered in this chapter are summarised in Table 7.1 according to their role in the subsequent modelling and verification procedure.

Table 7.1: Main legislative, regulatory, and technical references for the assessment of electromagnetic interference between AC power systems and buried metallic pipelines.

Reference	***Main Scope***	***Role in the Analysis***
D.M. 17 April 2008	Natural gas transmission	Establishes general safety and integrity requirements for pipelines
CEI EN 50443	Electromagnetic interference on metallic pipelines caused by HV AC systems	Main reference for assessment procedures, interference distances, coupling mechanisms, and voltage limits
CEI EN 50522	Grounding systems	Relevant for GPR, step voltages, and touch voltages
CEI EN 60909-3	Earth short-circuit currents in three-phase AC systems	Supports the calculation of fault current distribution through the soil, metallic sheaths, and grounding conductors, providing useful information for the assessment of GPR, reduction factors, and return current paths.
CEI 103-6	Electromagnetic induction on telecommunication lines under fault conditions	Secondary methodological reference for induced EMF, voltage to earth, exposure zone, and exposure length
CEI 11-17	Underground power cable systems	Relevant for installation configurations, physical coexistence, and cable system safety
UNI EN ISO 15589-1	Cathodic protection of onshore pipelines	Defines cathodic protection criteria for pipelines
UNI EN 12954	Cathodic protection of buried or immersed metallic structures	Provides general cathodic protection criteria and supports electrochemical assessment of the pipeline
UNI EN ISO 18086	AC corrosion and cathodic protection of pipelines	Reference for AC corrosion risk assessment criteria, widely cited in technical literature and experimental studies
CIGRE TB 95	Influence of HV AC systems on metallic pipelines	General framework for interference mechanisms and pipeline effects
CIGRE TB 290	AC corrosion on metallic pipelines interfered by AC lines	Technical support for risk criteria, modelling approaches, measurements, and countermeasures

CIGRE TB 373	Mitigation of power-frequency magnetic fields	Reference for magnetic field reduction techniques
CIGRE TB 559	Impact of electromagnetic fields on cable system ampacity	Support for evaluating the effects of mitigation solutions on losses, heating, and possible cable derating

In the following sections, the references listed in Table 7.1 are organized according to three levels of analysis. The first concerns legislative and installation requirements, which are necessary to define the physical coexistence between the cable system and the pipeline. The second addresses power-system-side criteria, required to establish operating, fault, and interference scenarios. The third concerns pipeline-side criteria, where the calculated electrical quantities are interpreted with respect to cathodic protection performance, AC corrosion, and pipeline integrity assessment. The final part of the chapter summarizes how these criteria are ultimately translated into simulation inputs, modelling assumptions, and output quantities.

7.1 General Legislative Requirements

The legislative provisions discussed in this section define the overall safety framework within which electrical infrastructures and natural gas transmission pipelines must be designed, constructed, and operated. Although these regulations do not constitute the primary reference for electromagnetic interference calculations, they establish installation constraints, safety criteria, applicability conditions, and general requirements governing the coexistence of different infrastructures.

In Italy, the design and installation of high- and extra-high-voltage cable systems are primarily governed by CEI 11-17 [44]. For issues related to the coexistence of power cables with other technological infrastructures (inductive coupling), including metallic pipelines and telecommunication systems, the standard refers to the technical documents developed by CEI Technical Committee 304. Although the conductive coupling mechanism associated with cable joint-bay grounding systems is not explicitly addressed, the grounding design of cable joint bays is required to comply with CEI 11-1, subsequently superseded by CEI EN 50522 [8]. The latter standard requires the assessment of transferred potentials arising from conductive coupling phenomena.

In Italy, the coexistence of buried gas pipelines and power cables installed in ducts or similar underground structures is governed by the Ministerial Decree of 17 April 2008, regarding the design, construction, testing, operation, and supervision of natural gas transmission infrastructures [66].

Consequently, for crossings and parallel installations involving power cables and natural-gas pipelines, the installation criteria and any necessary protective measures shall be defined in

coordination with the pipeline owner or operator to ensure compliance with the requirements of the decree.

Table 7.2 summarizes the main legislative and installation requirements concerning the coexistence of underground cable systems and buried infrastructures, with reference to minimum separation distances, crossings, and installation conditions.

Table 7.2: Main legislative and installation requirements concerning the coexistence of underground cable systems and buried infrastructures, with particular reference to minimum separation distances, crossings, and installation conditions.

Verification	Application Condition	Operational Criterion / Limit	Reference
Physical coexistence between cable and gas pipeline	Route design phase	Minimum separation distance of 0.5 m. Reducible to 0.3 m when a non-metallic separator is installed	CEI 11-17; DM 17/04/2008
Cable–pipeline crossings	Crossing between underground power cable and metallic pipeline/gas pipeline	No cable joints within 1 m of the crossing point; possible use of non-metallic separators or protective elements at the crossing	DM 17/04/2008; CEI 11-17
Cable joints near crossings	Crossing conditions	Cable joints should be avoided within 1 m of the crossing point unless suitable protective measures are adopted	CEI 11-17; DM 17/04/2008
Shared civil structures	Coexistence between cables and gas pipelines	Power cables and gas pipelines shall not be installed within the same civil structure	DM 17/04/2008

7.2 Power-System-Side Standards and Technical References

From the power-system perspective, CEI EN 50443 is the main reference for assessing electromagnetic interference on metallic pipelines caused by high-voltage AC systems. It defines the interference distance, the coupling mechanisms to be considered and the voltage limits to be verified under both normal operating and fault conditions [4].

For the purposes of this work, CEI EN 50443 is mainly used to define the relevant interference scenarios and the quantities to be verified. Along parallel exposure sections, inductive coupling is the dominant mechanism, while conductive coupling becomes relevant near substations, grounding systems, cable sheath earthing points or other locations where current is injected into the soil. Capacitive coupling is generally secondary for buried metallic pipelines and shielded underground

cable systems [4]. It is worth noting that conductive coupling associated with underground cable systems is generally limited, since only a small fraction of the fault current is injected into the earth through grounding systems. Owing to the high screening effectiveness of metallic cable screens, the earth current is typically only a few hundred amperes, even when the total fault current reaches several kiloamperes. Consistently with this behaviour, CEI EN 50443 specifies a general interference distance of 50 m for underground AC power systems. For conductive coupling associated with the earthing systems of HV cables above 50 kV, a distance of 20 m is considered [4].

Under normal operating conditions, pipe-to-soil voltage and voltage across insulating joints must be checked against the applicable steady-state limits (60 V). Different limits are defined in fault conditions:

- 2000 V for the infrastructure integrity;
- as a function of fault duration for personnel safety according to Table 7.3.

Table 7.3: Pipe-to-soil voltage limits under fault conditions as a function of fault duration, adopted in this work for personnel safety assessment and based on CEI EN 50443 [4].

Fault Duration	Permissible Voltage
≤ 0,1 s	2000 V
0,1 – 0,2 s	1500 V
0,2 – 0,35 s	1000 V
0,35 – 0,5 s	650 V
0,5 – 1 s	430 V
1 – 3 s	150 V
> 3 s	60 V

CEI EN 50522 constitutes the reference standard for the assessment of transferred potentials caused by conductive coupling between cable joint-bay grounding systems and low-voltage installations [8]. The standard is also commonly adopted as the basis for evaluating permissible touch-voltage limits in areas accessible to the general-public.

The CEI 103-6 standard establishes the permissible induced-voltage limits for telecommunication circuits and specifies the corresponding assessment methodology [48], in accordance with the approach described in CIGRE Technical Brochure 95.

CIGRE Technical Brochures (TB) are used as complementary references for interpreting the physical mechanisms and modelling choices. In particular, TB 95 supports the general assessment of AC interference on metallic pipelines, while TB 373 and TB 559 are useful for magnetic-field mitigation, cable losses, ampacity and possible derating effects [3], [46], [47].

CEI EN 60909-0 establishes the methodology for calculating maximum short-circuit currents in high- and extra-high-voltage power systems [67]. CEI EN 60909-3 is instead the principal reference

for the calculation of reduction factors, i.e. the contribution of metallic screens, cable sheaths, and earth wires in reducing the electromagnetic effects associated with fault currents [20].
Table 7.4 summarizes the main operational checks adopted from the power-system side.

Table 7.4: Main operational checks from the power-system perspective for the assessment of electromagnetic interference.

Verification	**Application Condition**	**Operational Criterion / Limit**	**Reference**
Area to be included in the study	Preliminary screening	Interference distance equal to 50 m	CEI EN 50443
Inductive coupling	Normal operation and fault conditions for metallic pipelines located within the interference distance	Calculate induced pipe-to-soil voltages and voltages across insulating joints along exposed sections, considering interfering current, parallel exposure length, cable-to-pipeline separation distance, system geometry, soil resistivity, and reduction factors associated with sheaths/ground conductors	CEI EN 50443; CIGRE TB 95
Conductive coupling	HV system earth fault and proximity to grounding systems, towers, substations, or sheath grounding points	Evaluate Ground Potential Rise, the actual current dispersed through the soil, and the possible transfer of potential to the pipeline; verify pipe-to-soil voltages and voltages across insulating joints as a function of fault duration	CEI EN 50443; CEI EN 50522
Capacitive coupling	Buried pipelines	Generally negligible for shielded and grounded underground cable systems; to be evaluated only in particular configurations	CEI EN 50443
Pipe-to-soil voltage and voltage across insulating joints	Normal operating conditions	≤ 60 V rms	CEI EN 50443
Fault voltage	Fault conditions in the interfering system	Verify that the interference voltage between pipeline and earth, and across insulating joints, does not exceed the limits specified in Table 3 of CEI EN 50443, which vary according to fault duration	CEI EN 50443

Longitudinal EMF / Induced voltage	Operation and fault conditions along parallel, oblique, or crossing sections	Calculate longitudinal EMF and voltage to earth according to CEI EN 50443; use CEI 103-6 only as methodological support for mutual impedances, exposure lengths/distances, and reduction factors	CEI EN 50443; CEI 103-6
Currents in metallic sheaths	Earth fault conditions and sheath grounding configurations	Evaluate the portion of fault current returning through metallic sheaths and grounding conductors, considering bonding configuration, grounding resistances, connection points, and cable reduction factors	CEI EN 50522; CEI EN 60909-3
Partial fault currents in the soil	Single-phase-to-earth fault	Calculate the distribution of fault current between soil, metallic sheaths, cable sheaths, and grounding conductors through reduction factors and current distribution models	CEI EN 60909-3
Touch and step voltages	Earth fault / Significant GPR conditions	Verify that touch voltages and, where necessary, step voltages remain within admissible limits as a function of fault duration	CEI EN 50522

7.3 Pipeline-Side Criteria: Cathodic Protection and AC Corrosion

As previously discussed, CEI EN 50443 defines acceptance limits in terms of induced voltage on the pipeline. However, from a corrosion perspective, the transverse current density at the pipe surface represents the most relevant parameter. AC-corrosion phenomena are generally associated with steady-state operation of the electrical infrastructure, as the cumulative exposure time is substantially greater than that associated with short-circuit events, despite the higher current levels that may occur during faults.

To prevent corrosion and AC-corrosion phenomena, pipelines are commonly protected through a combination of coating systems and cathodic protection measures, implemented either as passive sacrificial-anode systems or as active impressed-current systems. Although modern pipelines are generally protected by insulating coating systems, coating defects may arise during manufacturing, transportation, handling, or installation. These defects expose small areas of the steel surface to the surrounding soil and may therefore become susceptible to corrosion and AC-corrosion phenomena.

At coating defects, the AC current exchanged between the pipeline and the surrounding soil may become concentrated over a very small surface area, leading to higher current densities. As a result, compliance with the 60 V induced-voltage limit specified by CEI EN 50443 does not necessarily guarantee the absence of AC-corrosion risk [4]. For this reason, additional assessment criteria based on AC current density and cathodic-protection performance, as specified in UNI EN ISO 18086 and supplemented by UNI EN ISO 15589-1 and UNI EN 12954, should be considered [68], [69], [70].

Table 7.5 reports the main criteria used for cathodic protection and AC corrosion assessment of interfered pipelines.

Table 7.5: Main operational checks from the pipeline perspective for cathodic protection and AC corrosion assessment.

Verification	**Application Condition**	**Operational Criterion / Limit**	**Reference**
AC corrosion screening	Cathodically protected pipeline located near AC lines/cables	Assess AC interference whenever the pipeline is exposed to induced or conductive AC voltages/currents	UNI EN ISO 18086
AC pipe-to-soil voltage	Steady-state conditions	Measure/calculate U_{AC} as a 24-hour average value; target value ≤ 15 V rms. If U_{AC} > 15 V, proceed with a combined assessment based on J_{AC}, J_{DC}, OFF/IR-free potential, coating condition, and soil resistivity	UNI EN ISO 18086
Combined J_{AC}–J_{DC} *criterion*	Coating defects, coupons, or probes	Verify the average AC current density J_{AC}: baseline criterion $J_{AC} \leq 30\ A/m^2$. If $1 < J_{DC} < 10\ A/m^2$, J_{AC} values up to $100\ A/m^2$ may be acceptable only following a complete assessment. If $J_{DC} < 1\ A/m^2$ or $J_{DC} > 10\ A/m^2$, maintain $J_{AC} \leq 30\ A/m^2$	UNI EN ISO 18086
OFF/IR-Free potential and cp level	Cathodic protection assessment under AC interference	Measure the potential without IR drop contribution and interpret it together with U_{AC}, J_{AC}, and J_{DC}; verify that possible overprotection conditions do not increase AC corrosion risk	UNI EN ISO 18086; UNI EN ISO 15589-1
Coating defects	Local assessment	Consider small defects as critical points, since they concentrate AC current and may increase J_{AC}	UNI EN ISO 18086; CIGRE TB 290
Soil resistivity	Modelling / Local measurements	Evaluate soil resistivity and defect/coupon spreading resistance, since they directly influence exchanged current	UNI EN ISO 18086
Coupons / Probes	Field measurements	Install coupons or probes at critical locations to measure AC current, DC current, ON/OFF potential, and estimate corrosion rate	UNI EN ISO 18086
Measurement points	Monitoring activities	Provide measurements along parallel sections, crossings, insulating joints, drainage points, maximum potential locations, and sections with critical coating conditions	UNI EN ISO 18086; UNI EN ISO 15589-1
Mitigation and post-mitigation verification	Exceedance of acceptance criteria	Apply interference mitigation measures such as AC grounding, mitigation conductors, decoupling devices, SPD systems, or coating repair; verify that cathodic protection remains effective and repeat measurements of U_{AC}, J_{AC}, J_{DC}, ON/OFF potential, and drained current	UNI EN ISO 18086; UNI EN ISO 15589-1

7.4 Limitations of Standard Assessment Criteria

AC corrosion risk depends on the combination of electrical, electrochemical, and environmental quantities, including AC current density, cathodic protection conditions, IR-free potential, soil resistivity, and the local condition of coating defects [4], [63], [71].

Under AC interference conditions, localized corrosion phenomena may occur even when conventional cathodic protection criteria appear to be satisfied. AC pipe-to-soil voltage therefore represents a useful screening parameter, but it does not directly describe the current exchanged at coating defects. For the same induced voltage, small coating defects or low-resistivity soils may lead to high current densities and therefore to locally more critical conditions [63], [71].

Cathodic protection parameters must also be interpreted carefully. The ON potential may include the contribution of the ohmic voltage drop in the soil, whereas the IR-free potential is more representative of the actual polarization state of the metallic surface. Furthermore, cathodic overprotection conditions may increase the severity of the interaction with the AC component, showing that the risk depends not only on the intensity of the interference, but also on the electrochemical state of the pipeline [63].

An additional limitation concerns the time evolution of the insulating coating. Coating degradation may alter the transverse admittance of the pipeline–soil circuit and, consequently, the distribution of induced voltages and currents along the pipeline. For this reason, an assessment based on invariant electrical and geometrical parameters may not fully represent the evolution of risk over the service life of the pipeline [72].

Overall, normative and technical criteria should therefore be regarded as necessary but not exhaustive tools. They define the quantities to be verified and the admissible limits, but they provide only limited guidance regarding the practical selection of modelling parameters, such as coating characteristics, representative defect size, coating degradation conditions, and operating or fault scenarios. The construction of the model therefore requires engineering assumptions that are both justified and consistent with the available data for the specific case under analysis.

Table 7.6 summarizes some of the main applicability and interpretation limitations associated with the normative criteria used in the assessment of AC corrosion and electromagnetic interference on metallic pipelines.

Table 7.6: Main applicability and interpretation limitations of the criteria adopted for AC corrosion assessment.

Modelling Aspect	**Criticality / Modelling Implication**
Coating characteristics	Standards do not define unique values for coating resistivity, degradation, or admittance. These parameters must therefore be estimated or assumed in a representative manner
Coating defects	Defect size, distribution, and number are not uniquely defined and require the selection of equivalent defects or representative scenarios
Fault scenarios	Standards do not impose a unique set of scenarios. Their selection depends on the actual system configuration and on the objectives of the study
Fault currents	Depend on network configuration, grounding system, and installed protection devices
Fault clearing time	Must be associated with the actual protection systems and with the considered network scenario
Soil parameters	Soil resistivity and stratification may vary spatially and temporally, influencing mutual impedances and return current paths
Cathodic protection conditions	Actual polarization conditions may differ from nominal or theoretical values
Pipeline ageing over time	Coating ageing and changes in cathodic protection may alter the electromagnetic response of the pipeline
Currents in metallic sheaths and return paths	Depend on the actual bonding configuration, sheath continuity, and the presence of parallel metallic return paths

7.5 Simplified Screening Calculations for Cable–Pipeline Interference

The previous chapters defined the physical mechanisms of interference, the cable and pipeline elements involved in the coupling process, the regulatory acceptance criteria, and the mutual-impedance formulations required for numerical modelling. Based on this framework, the present chapter introduces a simplified screening assessment aimed at obtaining preliminary order-of-magnitude indications before developing the complete cable–pipeline simulation.

The approach follows the general logic of the reference influence distance introduced in ITU-T K.68. Although this Recommendation is formally addressed to telecommunication systems exposed to power-system interference, its distance-based methodology can also be used as a preliminary screening tool for identifying configurations that require further investigation. However, for the evaluation of interference distances, CEI EN 50443 refers to the methodology described in ITU-T K.68 [4], [7].

Two simplified checks are considered. The first addresses inductive interference and evaluates a critical separation distance associated with a prescribed induced-voltage limit. The second addresses conductive interference and estimates the Ground Potential Rise influence zone by replacing the actual earthing arrangement with an equivalent hemispherical electrode. These calculations were developed by the author for this thesis: they do not reproduce the original K.68 curves but apply the same screening logic using the mutual-impedance formulations and voltage criteria adopted in the present work.

The resulting charts are, therefore, intended as original preliminary tools to identify potentially critical configurations and to support the interpretation of the subsequent distributed cable–pipeline model, rather than as a substitute for the detailed simulation.

7.5.1 K68-Based Inductive Interference Distance

The inductive screening assessment is based on the graphical approach proposed in ITU-T K.68 for the evaluation of the reference influence distance. In the original recommendation, the separation distance is related to the equivalent soil resistivity and to a normalised voltage parameter, allowing the designer to identify the distance beyond which a more detailed interference assessment may not be required [7].

In this work, the same graphical logic is retained, but the mutual impedance is not evaluated using the polynomial approximation reported in K.68. Instead, the mutual earth-return impedance z_m is calculated using the formulations introduced in Chapter 6, in order to keep the screening procedure consistent with the cable–pipeline model adopted in this thesis. The normalised induced voltage is defined as:

$$u_m = \frac{U_{lim}}{I\ L} \tag{7.1}$$

where:

- U_{lim} is the selected induced-voltage limit [V];
- I is the inducing current flowing in the interfering cable system [kA];
- L is the parallel exposure length between the cable system and the pipeline [km];
- u_m is the normalised induced voltage [V/(km · kA)].

When I is expressed in kA and L in km, u_m is numerically equivalent to $|\ z_m\ |$ expressed in mΩ/km. Therefore, each curve in the screening chart represents a constant value of mutual coupling [7]. For each selected value of u_m, the corresponding curve is obtained by varying the equivalent soil resistivity ρ and solving for the horizontal separation x_{ij} that satisfies:

$$\left|z_m(\rho, x_{ij})\right| = u_m \tag{7.2}$$

with z_m expressed in mΩ/km. In the Wedepohl-based chart, the solution is interpreted only within the validity range $\left|md_{ij}\right| < 0.25$. In the Pollaczek-based chart, the same procedure is applied using the complete mutual earth-return impedance formulation [7].

Figures 7.1 and 7.2 report the resulting K68-like screening charts. The first chart is obtained using the compact Wedepohl approximation, while the second is obtained using the complete Pollaczek formulation. The charts are read by selecting the soil resistivity and the normalised voltage u_m; the corresponding curve gives the critical horizontal separation x_{ij}. If the actual cable–pipeline separation is lower than this value, the configuration cannot be discarded at the screening stage and a more detailed distributed simulation of the pipeline system is required.

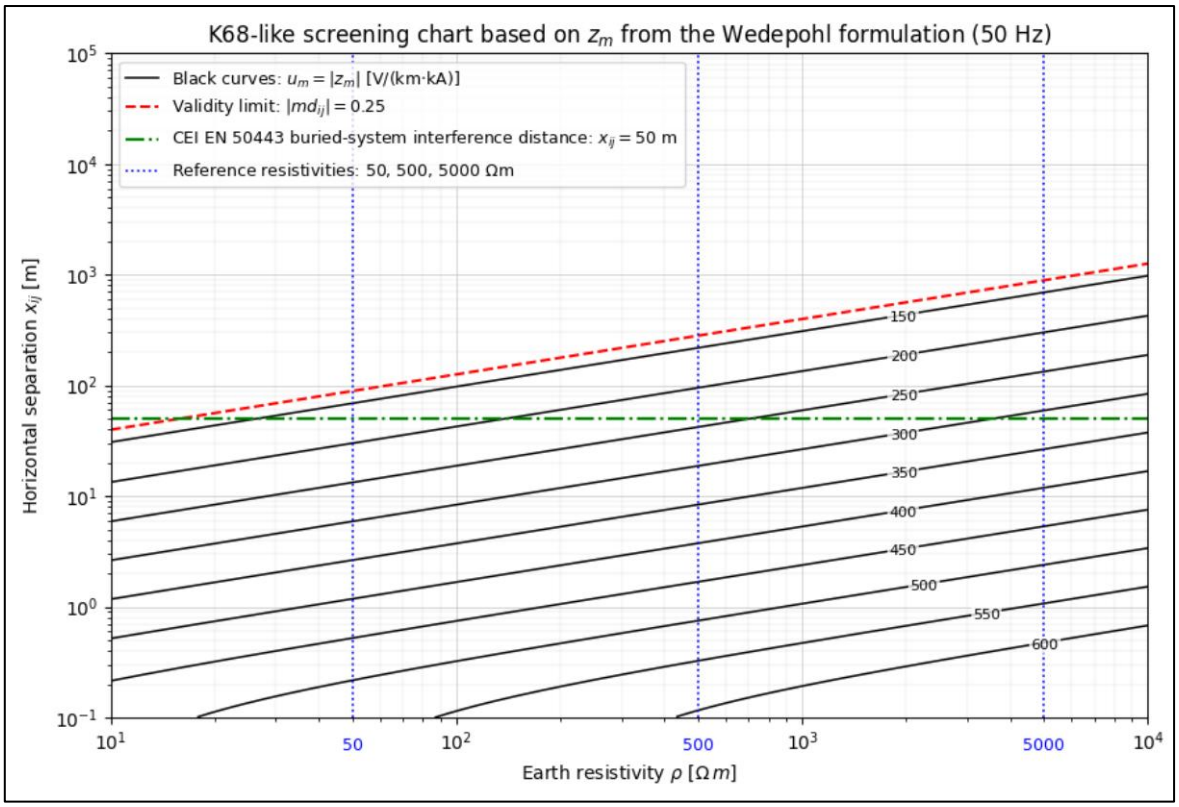


Figure 7.1: K.68-inspired inductive screening chart obtained in this work using the compact Wedepohl approximation for the mutual earth-return impedance. The black curves represent constant values of the normalised induced voltage, while the red dashed curve indicates the formal validity limit of the approximation.

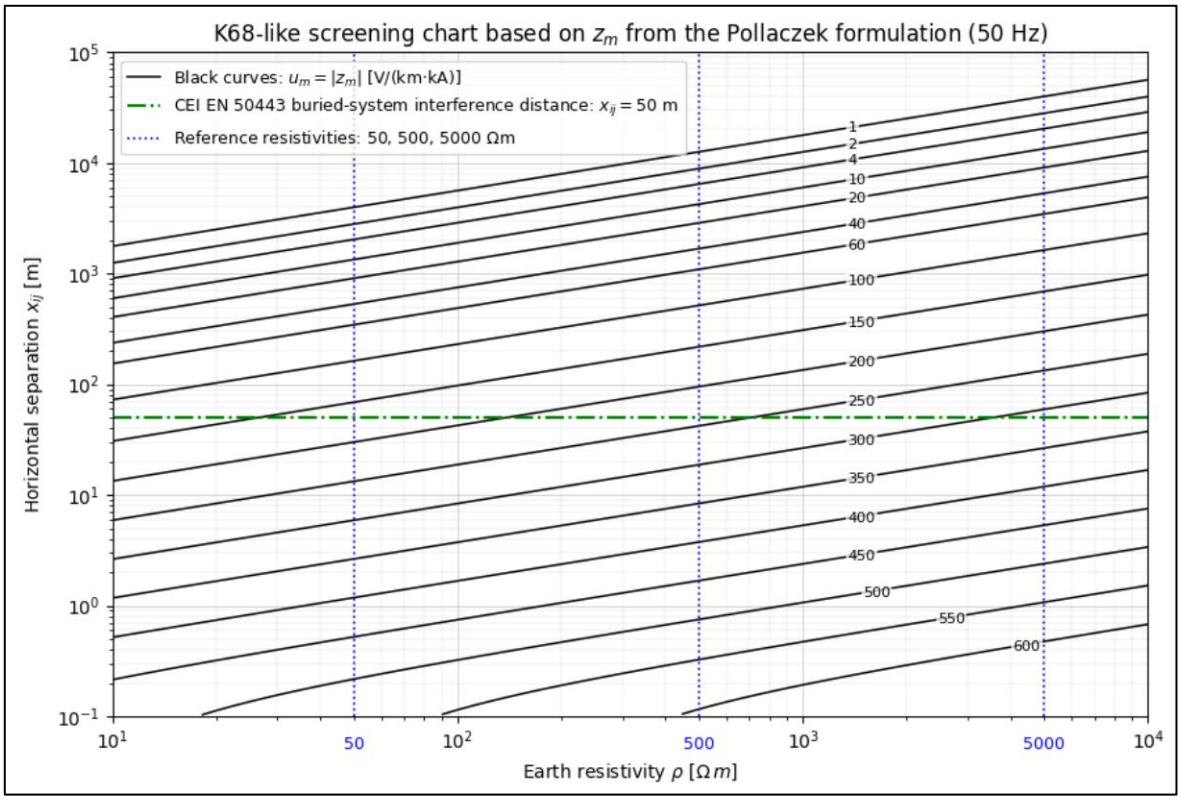


Figure 7.2: K.68-inspired inductive screening chart obtained in this work using the complete Pollaczek formulation for the mutual earth-return impedance. The chart relates soil resistivity, horizontal cable–pipeline separation and normalised induced voltage.

The comparison between the two charts shows that the Wedepohl formulation provides a compact screening representation, but only within its formal validity range. The Pollaczek formulation, instead, can be used as the reference chart when the screening assessment must be extended beyond this range.

The green horizontal line represents the 50 m interference distance indicated by CEI EN 50443 for buried AC power systems. From an application point of view, this line identifies the practical screening boundary considered in this work. Within this distance range, the Wedepohl validity limit is generally not restrictive, except for very low soil resistivity values.

In both cases, the obtained distance should be interpreted as a preliminary indication of potentially critical cable–pipeline configurations. The actual voltage profile along the pipeline still depends on the distributed model.

To further assess the practical impact of this limitation, the compact Wedepohl approximation was compared with the Pollaczek reference formulation also outside its formal validity range. The comparison was carried out in terms of the normalised induced voltage $u_m = |z_m|$, grouping the results according to increasing values of the dimensionless parameter $|md_{ij}|$. The objective is to quantify how rapidly the error increases when the condition $|md_{ij}| < 0.25$ is no longer satisfied.

The results are shown in Table 7.7.

Table 7.7: Error of the Wedepohl compact approximation with respect to the Pollaczek reference formulation outside the formal validity range.

Range of $\|md_{ij}\|$	Mean absolute error [%]	Median absolute error [%]	95th percentile absolute error [%]	Maximum absolute error [%]
$0.25 < \|md_{ij}\| \leq 0.50$	0.30	0.24	0.70	0.78
$0.50 < \|md_{ij}\| \leq 1.00$	2.87	2.31	6.11	6.99

The results show that the Wedepohl approximation remains very close to the Pollaczek reference formulation immediately beyond the formal validity boundary. For $0.25 < |md_{ij}| \leq 0.50$, the maximum absolute error remains below 1%, while for $0.50 < |md_{ij}| \leq 1.00$ the error is still moderate but no longer negligible, with a 95th-percentile absolute error of approximately 6%. For $|md_{ij}| > 1$, the 95th-percentile error becomes very large and increases rapidly as the validity condition is increasingly violated. This confirms that the compact Wedepohl expression should not be used far beyond its validity range. In those cases, the Pollaczek formulation must be retained as the reference model.

7.5.2 Simplified GPR Assessment with Equivalent Hemispherical Electrode

The second screening calculation concerns conductive interference associated with Ground Potential Rise. During an earth fault, part of the fault current may be injected into the soil through the grounding system of a joint bay, a sheath earthing point or another local earthing arrangement. This produces a local rise of the soil potential with respect to remote earth.

In line with the screening logic of ITU-T K.68, the conductive interference is, therefore, treated as a distance-dependent problem associated with the Earth Potential Rise zone surrounding the earthing arrangement [7].

In the detailed model, the actual grounding system geometry and the surrounding soil properties determine the spatial distribution of the ground potential. For a preliminary assessment, however, the real grounding arrangement can be replaced by an equivalent hemispherical electrode injecting the same current I_E into a homogeneous soil. Under this assumption, the ground potential at a distance r from the equivalent electrode is:

$$U(r) = \frac{\rho I_E}{2\pi r} \tag{7.3}$$

where:

- $U(r)$ is the ground potential rise at distance r, referred to remote earth [V];
- ρ is the equivalent soil resistivity [Ω m];
- I_E is the current injected into the soil [A];
- r is the distance from the equivalent hemispherical electrode [m].

By imposing $U(r) = U_{lim}$, the critical distance is obtained as:

$$r_{lim} = \frac{\rho I_E}{2\pi U_{lim}} \tag{7.4}$$

where:

- r_{lim} is the critical distance from the equivalent hemispherical electrode [m];
- U_{lim} is the admissible voltage limit [V], selected according to the fault duration on the basis of CEI EN 50443 or CEI EN 50522 [4], [8].

Therefore, r_{lim} represents the distance beyond which the soil potential rise is lower than the admissible limit. Within this distance, the configuration cannot be discarded at the screening stage and a more detailed assessment is required [7].

Figure 7.3 reports the resulting GPR screening chart obtained from the equivalent hemispherical-electrode model and the admissible voltage limits associated with fault duration.

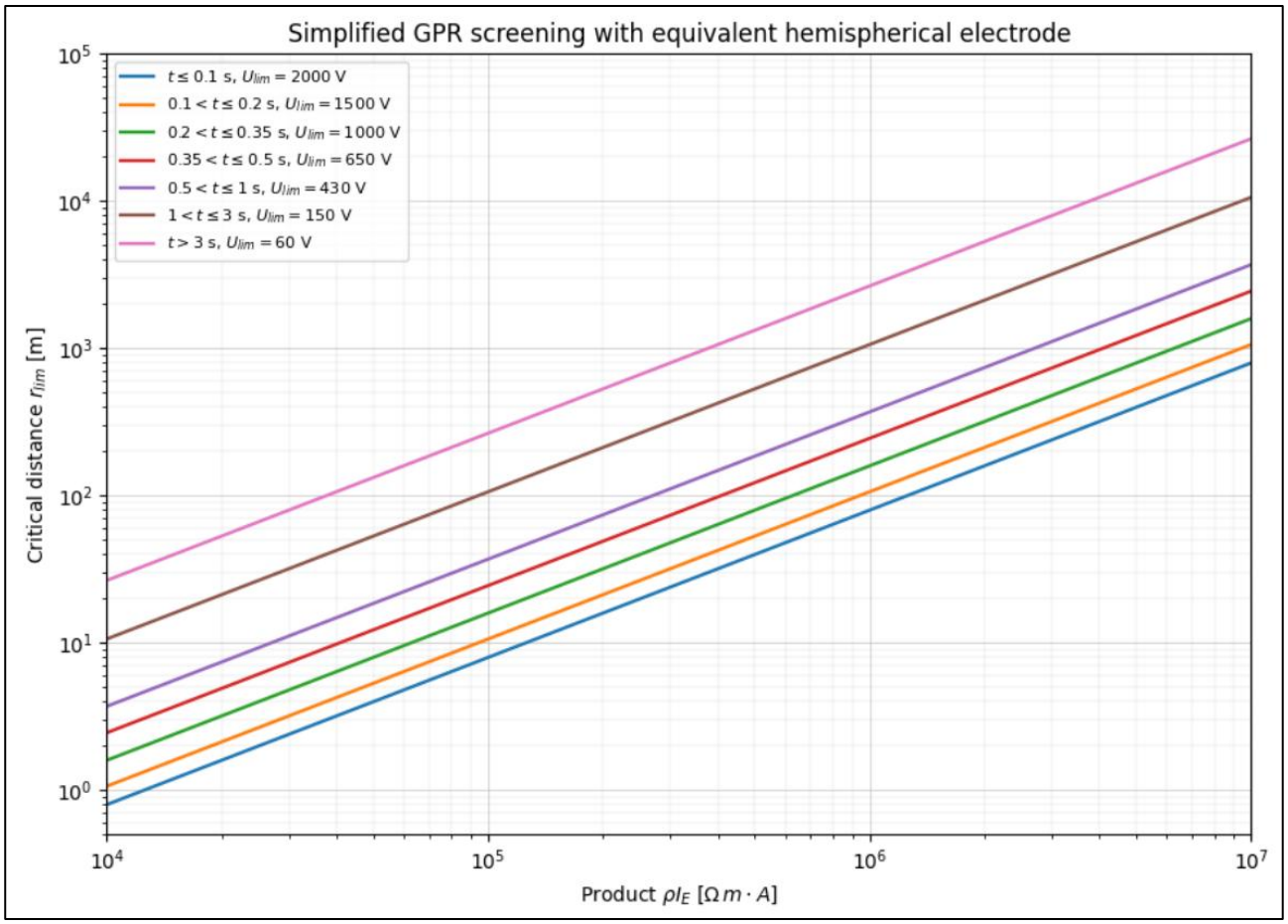


Figure 7.3: Simplified GPR screening chart obtained in this work using the equivalent hemispherical-electrode model and the admissible voltage limits derived from CEI EN 50443 [4].

The chart is used as an order-of-magnitude tool. Once ρ and I_E are known, their product is located on the horizontal axis and the corresponding critical distance is read from the curve associated with the applicable fault-duration limit. If a pipeline, test post, insulating joint or accessible metallic part lies within this distance, the GPR condition must be analysed in more detail.

It is important to note that $U(r)$ is a soil potential referred to remote earth. The practical safety issue arises when an accessible metallic structure does not follow the same local soil potential, for example because the pipeline is well insulated by its coating or is electrically referenced to remote points. In that case, a person touching the metallic structure while standing on the local soil may be exposed to a significant touch voltage.

This screening does not replace the detailed grounding and pipeline model. It neglects the real geometry of the grounding system, soil stratification, coating impedance, local connections and terminal conditions. Nevertheless, it provides a simple preliminary estimate of the GPR influence zone and supports the identification of potentially critical configurations before the complete distributed simulation.

The two screening calculations therefore provide complementary preliminary indicators: the K68-like chart identifies potentially critical inductive-coupling distances, while the GPR chart estimates the conductive influence zone around grounding points. These results are used only as preliminary criteria and are subsequently interpreted through the complete distributed cable–pipeline model.

8. ATP-EMTP MODELLING AND ANALYSIS OF EARTH-FAULT INTERFERENCE IN THE LA SPEZIA CABLE–PIPELINE CORRIDOR

The modelling methodology developed in the previous chapters is applied in the following to a real cable–pipeline interference case study located in the La Spezia port area. The case concerns a new 132 kV underground cable connection interacting with two existing buried gas pipelines. The project configuration, cable and pipeline characteristics, and operating conditions relevant to the electromagnetic-interference assessment are presented in the following sections.

8.1 Project framework and analysed configuration

This section identifies the project configuration selected for the analysis, distinguishes the successive temporary operating stages from the final permanent arrangement, describes the modelled cable–pipeline corridor and defines the reference fault condition adopted in the ATP-EMTP simulations.

8.1.1 Temporary and permanent network configurations

The case study is part of the development of the 132 kV electrical infrastructure serving the La Spezia port area. The project comprises two temporary configurations followed by the final permanent network arrangement.

The existing system includes the fluid-filled underground cable connection between La Spezia Substation and La Pianta Primary Substation. From La Pianta Primary Substation, the new 132 kV underground connection extends towards the port area through an intermediate Joint Bay.

In the first temporary configuration, the new connection terminates at the SCRI substation. This installation provides the temporary terminal of the 132 kV connection during the development of the subsequent project stages.

The second temporary configuration retains the connection between La Pianta Primary Substation, the Joint Bay and the SCRI Substation, and adds the downstream connection to the AdSP User Primary Substation. The first configuration therefore terminates at the SCRI Substation, whereas the second extends the temporary network to the AdSP User Primary Substation. The two configurations are compared schematically in Figure 8.1.

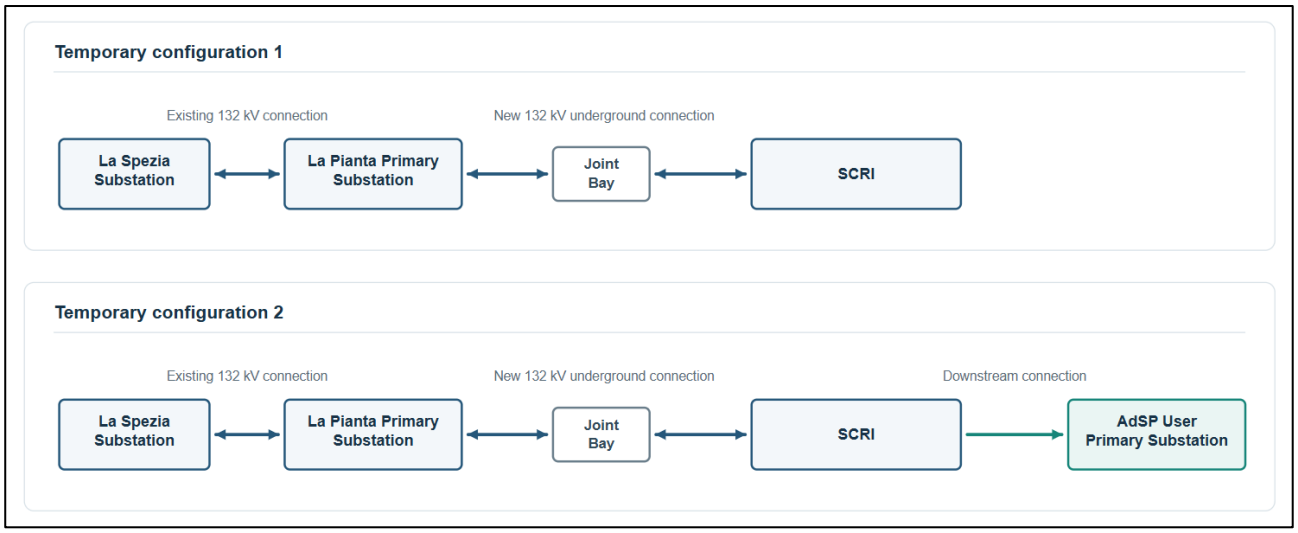


Figure 8.1: Schematic comparison developed in this work of the first and second temporary configurations of the 132 kV connection serving the La Spezia port area.

The final configuration involves the subsequent reorganisation of the network through the new port-area substation and the construction of two underground cable connections from La Spezia Substation, located on the northern and southern sides of the route. Although relevant from an electromagnetic-interference perspective, this configuration was not included in the numerical analysis.

The objective of this thesis is to analyse electromagnetic interference under the temporary network configuration. Attention is given to the second operating stage, which is considered the most conservative scenario due to the lower equivalent grounding impedance of the La Pianta substation.

The analysed corridor includes sections in which the underground cable approaches or runs alongside two metallic gas pipelines operating at low and medium pressure. The Mobile User Substation included in the analysed configuration is shown in Figure 8.2.



Figure 8.2: Field view of the SCRI forming the mobile user substation in the analysed temporary configuration of the 132 kV connection serving the La Spezia port area [73].

The case study assesses the electromagnetic interaction between the temporary 132 kV underground connection and the two pipelines, focusing on the earth-fault current-return paths, the ECC arrangement and the pipeline boundary conditions. The permanent configuration is retained only as part of the general project framework.

8.1.2 Modelled cable–pipeline corridor

The analysed system consists of a 132 kV three-phase single circuit underground cable. Each phase is represented by a single-core cable comprising a segmented copper conductor, XLPE insulation, an Aldrey-alloy wire screen and an external HDPE sheath. The main cable characteristics are summarised in Table 8.1.

Table 8.1: Main characteristics of the modelled underground cable system.

Model aspect	***Adopted representation***
Rated voltage	132 kV
Number of circuits	1
Cable type	Single-core underground cables
Main conductor	Segmented copper conductor
Nominal conductor cross-section	1600 mm^2
Main insulation	XLPE
Metallic screen	Aldrey-alloy wires
External sheath	HDPE
Cable transposition	Not adopted
Screen-bonding arrangement	Mid-point bonding
ECC arrangements assessed	Documented one-ECC arrangement and candidate two-ECC arrangement

Each ECC is represented as a longitudinally watertight 240 mm^2 copper conductor with EPR insulation and an external HDPE sheath. The ECCs are continuous along the complete cable connection and are not longitudinally transposed.

The one-ECC arrangement corresponds to the documented temporary configuration. A second ECC was introduced as a candidate alternative to assess the additional earth-fault return capacity and electrical redundancy provided by a parallel conductor. Since this arrangement is not included in the current project drawings, ECC2 is treated exclusively as a modelling alternative. It is assigned the same electrical and geometrical characteristics as ECC1, follows the same route and is connected to the same earthing systems at La Pianta Primary Substation, the Joint Bay and the SCRI.

Figure 8.3 provides a schematic representation of the most common TOC installation arrangement along the analysed route. The three phase cables are installed in dedicated ducts, while the auxiliary cable ducts and the ECC ducts are grouped within the adjacent larger duct. The figure shows the configuration including both ECC1 and the candidate ECC2 and is intended only to illustrate their relative arrangement; dimensions and distances are therefore not reported to scale.

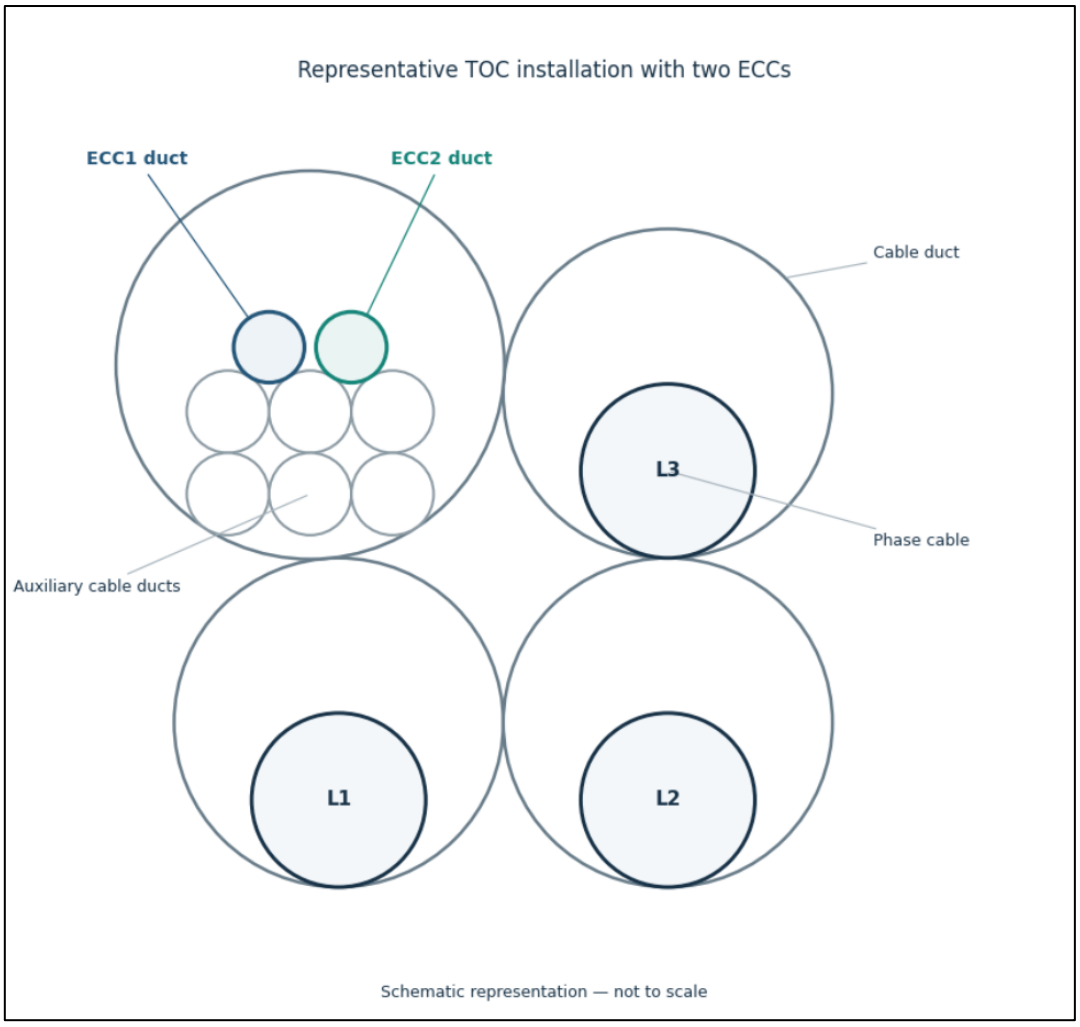


Figure 8.3: Schematic representation developed in this work of the representative TOC installation arrangement with the documented ECC1 and the candidate ECC2.

The cable burial depth varies along the route from approximately 1.35 m to 8÷9 m, with the greatest depths occurring near the railway crossing.

Two coated carbon-steel gas pipelines were included as interfered systems:

- a low-pressure pipeline, denoted as the LP pipeline;
- a medium-pressure pipeline, denoted as the MP pipeline.

Their main characteristics are reported in Table 8.2.

Table 8.2: Main characteristics of the metallic pipelines included in the electromagnetic model.

Model aspect	***LP pipeline***	***MP pipeline***
Service class	Low pressure	Medium pressure
Nominal diameter	DN300	DN300
Construction	Coated carbon-steel pipeline	Coated carbon-steel pipeline
Installation	Buried	Buried
Route configuration	Parallel, oblique and crossing sections	Parallel, oblique and crossing sections

The same material properties were assigned to both pipelines because the specific steel grade and coating formulation were unavailable. A relative permittivity of $\varepsilon_{r,\mathrm{coat}} = 2.3$ was adopted for the polyethylene-based coating, using the representative value reported for PE and HDPE in IEC 60287-1-1, adopted in Italy as CEI 20-21/1-1 [74]. The relative magnetic permeability of the carbon-steel wall was set to $\mu_{r,\mathrm{pipe}} = 300$, consistently with the representative value adopted by Ametani for a buried gas pipeline [58].

The route also crosses a railway and several existing utilities, including water pipelines, low-voltage cables and minor underground systems. These infrastructures affected the installation geometry and burial depth but were not explicitly represented as interfered conductors.

8.1.3 Analysed fault condition and modelling scope

Following a preliminary comparison of faults applied at both cable terminals, the single-phase-to-earth fault at the SCRI substation was selected as the reference condition for the subsequent analyses. The fault resistance was assumed to be negligible. The adopted simulation settings are summarised in Table 8.3.

Table 8.3: Fault condition and numerical settings adopted in the ATP-EMTP simulations.

Simulation aspect	***Adopted setting***
Fault type	Single-phase-to-earth fault
Fault location	Mobile-substation terminal of the temporary 132 kV cable connection
Fault resistance	Negligible
Simulation time step	$\Delta t = 10^{-4}$ s
Total simulation time	$t_{\max} = 0.5$ s
Adopted fault-clearing time	$t_F = 0.35$ s
Equivalent network	Thévenin equivalent impedance at La Pianta substation.

The adopted fault-clearing time was 0.35 s, according to Annex A.8 of Terna Grid Code [75]. This duration falls within the $0.2 < t_{\mathrm{F}} \leq 0.35$ s interval and, therefore, corresponds to an admissible fault-induced interference voltage of 1000 V_{rms} according to CEI EN 50443 [4]. This limit is applied to the results in Section 8.5.1.

8.2 ATP-EMTP model implementation

The cable system, screens, ECC, grounding connections and metallic pipelines were represented as a multiconductor underground system. The route was divided into sections with locally uniform geometry, each represented through a dedicated line-constant model.

8.2.1 Upstream-network equivalent

The external network upstream of the cable connection was represented according to the equivalent-voltage-source method of CEI EN 60909-0 [67]. The equivalent was calibrated using the official Terna maximum three-phase and single-phase-to-earth short-circuit currents at the La Pianta Primary Substation, which represents the sending end of the temporary cable connection. These data were adopted as the initial symmetrical currents I''_{k3} and I''_{k1} in the equivalent-source calculation. An ideal voltage source was placed behind positive-, negative- and zero-sequence equivalent reactances, thereby reproducing the maximum short-circuit strength of the upstream network without explicitly modelling the complete system.

Since the analysis concerns the sinusoidal fault-current component at power frequency, the sequence impedances were assumed to be purely reactive. In power transmission systems, the negative-sequence impedance is commonly assumed to be equal to the positive-sequence impedance. Based on this assumption, the following equations have been adopted to evaluate the Thévenin equivalent impedance:

$$X_1 = X_2 = \frac{cU_n}{\sqrt{3}\, I''_{k3}} \tag{8.1}$$

$$X_0 = \frac{\sqrt{3}\, cU_n}{I''_{k1}} - X_1 - X_2 \tag{8.2}$$

where:

- X_1 is the positive-sequence equivalent reactance, [Ω];
- X_2 is the negative-sequence equivalent reactance, [Ω];
- X_0 is the zero-sequence equivalent reactance, [Ω];
- c is the voltage factor defined according to CEI EN 60909-0, [pu];
- U_n is the nominal line-to-line voltage, [V];
- I''_{k3} is the maximum initial symmetrical three-phase short-circuit current adopted for the La Pianta Primary Substation node, [A];
- I''_{k1} is the maximum initial symmetrical single-phase-to-earth short-circuit current adopted for the La Pianta Primary Substation node, [A].

8.2.2 Cable system and earthing representation

Each cable section was represented using an ATP-EMTP line-constant (LCC) model comprising the phase conductor, XLPE insulation, metallic screen and external protective sheath. The insulation parameters were selected to reproduce the available core-to-screen capacitance. A preliminary no-load energisation check showed negligible deviation from the expected capacitive behaviour; detailed results are therefore not reported separately.

The screen-bonding arrangement specified in Table 8.1 was implemented explicitly. At the joint bay, the cable-screen surge arresters (SAs) connected between the relevant screen terminations and the local earthing system were represented in their blocking state. Their impedance was therefore assumed to be sufficiently high for the corresponding current to be negligible.

The one- and two-ECC geometries described in Section 8.1.2 were reproduced in the corresponding LCC sections. Each ECC was represented as a separate conductor extending continuously from La Pianta Primary substation to the SCRI Substation. The ECCs were connected to the earthing systems at La Pianta Primary substation, the joint bay and the SCRI substation. At the joint bay, electrical continuity was retained and an additional connection to the local earthing system was introduced.

The soil was represented as a homogeneous and isotropic medium with a uniform resistivity of 100 Ωm. This value lies in the lower part of the site-specific range of soil resistivity map of Atlarete (Terna application). It was applied uniformly in the LCC earth-return model and in the THOR 50Hz

(grounding system software developed by Terna) calculation of the joint-bay earthing resistance, ensuring consistency between the distributed cable model and the lumped earthing representation.

At La Pianta Primary substation, the earthing resistance was set to $0.04\ \Omega$. This value was taken from an Enel technical document reporting a dedicated verification of the substation earthing system.

The joint bay earthing resistance, R_{JB}, was calculated using THOR50Hz from the available earthing-system geometry and the adopted soil resistivity. The resulting value was $R_{JB} = 5.6\ \Omega$.

In the first temporary configuration, the SCRI substation earthing system was considered independently and assigned a target design resistance of $1\ \Omega$, a realistically attainable value, taking into account the space constraints associated with the implementation of the temporary solution at the SCRI substation.

In the second temporary configuration, the downstream AdSP User Primary Substation provides an additional connection to earth. This substation was not represented explicitly in ATP-EMTP; its contribution was included through the equivalent resistance seen at the SCRI substation terminal. The parallel connection of the two earthing systems gives an equivalent resistance of $0.61\ \Omega$. A conservative value of $R_{\mathrm{MUS}} = 0.5\ \Omega$ was adopted in the simulations. The adopted earthing connections are summarised in Table 8.4.

Table 8.4: Equivalent earthing connections adopted in the ATP-EMTP model of the second temporary configuration.

Location	***Equivalent resistance***	***Connected element***
La Pianta Primary Substation	0.04 Ω	Metallic screens and ECC
Joint bay	5.6 Ω	ECC; cable-screen SA earth reference
Mobile User Substation	0.5 Ω	ECC

8.2.3 Pipeline route and terminal representation

The cable and pipeline routes are not uniformly parallel. The electromagnetic model was, therefore, divided into consecutive sections with locally uniform cross-sectional geometry, following the sectional approach of CIGRE Technical Brochure 95 [3].

The discretisation was based on the following principles:

- each LCC section represents a locally uniform cable–pipeline geometry;
- oblique routes are converted into equivalent parallel sections;
- the representative lateral separation is determined from the local route geometry;
- changes in the side of the pipeline relative to the cable are retained;
- crossing regions are represented by dedicated sections.

Electrical continuity was maintained between adjacent sections, while the pipeline depth and lateral position were updated according to the local equivalent geometry. The LP and MP pipelines were modelled independently, without including mutual electromagnetic coupling between them.

Because the pipeline routes beyond the reconstructed interference zone are not known in sufficient detail, each end of the LP and MP pipelines was extended through an LCC section of length L_{ext}. This continuation retains the longitudinal pipeline impedance and the distributed coating capacitance to earth before the remote terminal condition is applied.

An insulating joint and a pipeline surge arrester in its blocking state were represented as an open circuit. When the pipeline surge arrester was assumed to operate, its internal conducting resistance was considered negligible compared with the remaining components of the discharge path. The complete connection between the pipeline and the local earth was therefore represented by the equivalent terminal resistance $R_{\mathrm{term}} = 10\ \Omega$, corresponding mainly to the earthing system of surge arrester.

An active impressed-current cathodic-protection system was assumed. Since the analysis is limited to AC quantities at 50 Hz, its DC source was not represented as an independent excitation. When a terminal surge arrester operates, the resulting low-impedance discharge path effectively bypasses the cathodic-protection system, which therefore does not affect the calculated AC response. This assumption applies to an active impressed-current system and would not necessarily apply to passive cathodic protection based on sacrificial anodes. The pipeline is not assumed to be directly grounded: its AC terminal behaviour remains defined by L_{ext} and R_{term}.

The selected continuation lengths, arrester operating threshold and terminal states are assessed in Section 8.4.

8.3 Influence of the ECC arrangement on fault-current return and pipeline voltage

Under the second temporary network configuration, a single-line-to-ground fault at the SCRI substation produced higher induced voltages on the pipeline than the corresponding fault at the La Pianta Primary Substation. The reason is that the fault current is fed directly from the La Pianta Primary Substation, whereas the SCRI substation is modelled as a passive node.

The influence of the faulted phase on the analysed quantities was found to be negligible. Repeating the complete analysis for faults on L1, L2 and L3 was therefore unnecessary, and L2 was selected as the representative faulted phase. All subsequent results refer to an L2-to-earth fault at the SCRI substation in the second temporary configuration.

The following subsections define the current quantities used in the assessment and compare their redistribution along the two cable sections for the one- and two-ECC arrangements.

8.3.1 Current definitions and route segmentation

The cable connection was divided into two electrical sections:

- La Pianta Primary Substation–joint bay;
- joint bay–SCRI substation.

This separation is required because the connection of the ECCs to the joint-bay earthing system modifies the current carried by the conductors in the two sections.

For each section, the residual phase-current phasor was defined as

$$3\bar{I}_0^s = \bar{I}_{\mathrm{L1}}^s + \bar{I}_{\mathrm{L2}}^s + \bar{I}_{\mathrm{L3}}^s \tag{8.3}$$

where:

- $s = 1$ identifies the La Pianta Primary Substation–joint bay section, while $s = 2$ identifies the joint bay– SCRI substation;
- $\bar{I}_{\mathrm{L1}}^s$, $\bar{I}_{\mathrm{L2}}^s$ and $\bar{I}_{\mathrm{L3}}^s$, are the phase-conductor current phasors in section s, [A];
- $\bar{I}_0^s$ is the zero-sequence current phasor in section s, [A];
- $3\bar{I}_0^s$ is the residual phase-current phasor in section s, [A].

The total current returned through the ECCs was defined as

$$\bar{I}_{ECC,\Sigma}^s = \sum_{n=1}^{N_{ECC}} \bar{I}_{ECC,n}^s \tag{8.4}$$

where:

- $\bar{I}_{ECC,n}^s$ is the current phasor carried by the n-th ECC in section s, [A];
- n identifies the individual ECC;
- N_{ECC} is the number of ECCs included in the analysed arrangement and is equal to 1 or 2;
- $\bar{I}_{ECC,\Sigma}^s$ is the phasor sum of the currents returned through the ECCs in section s, [A].

The residual inducing-current phasor was calculated as

$$\bar{I}_{ind}^s = 3\bar{I}_0^s - \bar{I}_{ECC,\Sigma}^s \tag{8.5}$$

where $\bar{I}_{ind}^s$ is the residual inducing-current phasor not returned through the ECCs in section s, [A].

The phase-current reference direction was defined from La Pianta Primary Substation towards the SCRI substation whereas the ECC-current reference direction was defined in the opposite direction, consistently with the return-current path. The same convention was applied to both cable sections. The reported values are RMS magnitudes calculated after performing the complex phasor subtraction in Equation (8.5). As can be seen, the metallic-screen currents were not included in Equation (8.5), since the cable screens are connected to earth through surge arresters. The surge arresters are designed

to remain in the non-conducting state under internal fault conditions and therefore do not contribute to the earth-fault current path.

The residual inducing current was therefore used as a comparative indicator of the current not returned through the ECCs. These definitions were applied to the representative L2 fault and to both the one- and two-ECC arrangements. To isolate the effect of the ECC configuration, the same pipeline boundary conditions were retained throughout the comparison. Hereafter, the sending terminal (S) and ending terminal (E) denote the two ends of each reconstructed pipeline route according to the adopted longitudinal direction. These labels refer to the pipeline route and not to the La Pianta Primary Substation and Mobile User Substation terminals of the cable connection. For both the LP and MP pipelines, the adopted boundary conditions were

$$L_{\mathrm{S}} = L_{\mathrm{E}} = 1000\ \mathrm{m}, \qquad R_{\mathrm{term,S}} = 10\ \Omega, \qquad R_{\mathrm{term,E}} = \infty.$$

The sending terminal therefore represents the conducting surge-arrester condition, whereas the ending terminal remains open.

8.3.2 Effect of the ECC arrangement on current return and pipeline voltage

The current results for both cable sections are summarised in Table 8.5.

Table 8.5: Phase-current sum, total ECC return current and residual inducing current in the two cable sections for the one- and two-ECC configurations under the representative L2-to-earth fault.

Quantity	***1 ECC***		***2 ECCs***	
	La Pianta Primary Substation–Joint Bay	**Joint Bay–Mobile User Substation**	**La Pianta Primary Substation–Joint Bay**	**Joint Bay–Mobile User Substation**
$\lvert 3I_0 \rvert$ $[kA_{rms}]$	11.863	11.852	11.954	11.944
$\lvert I_{ECC,\Sigma} \rvert$ $[kA_{rms}]$	8.634	8.836	9.635	9.788
$\lvert I_{ind} \rvert$ $[kA_{rms}]$	3.321	3.103	2.388	2.220
I_{ind} *reduction* [%]	—	—	28.11	28.44

The magnitude of $3I_0$ remained between 11.852 and $11.954\ \mathrm{kA_{rms}}$. In the La Pianta Primary Substation–joint bay section, the total ECC return current increased from 8.634 to $9.635\ \mathrm{kA_{rms}}$, reducing the residual inducing current from 3.321 to $2.388\ \mathrm{kA_{rms}}$, corresponding to a reduction of 28.11%. In the joint bay–SCRI substation section, the ECC return current increased from 8.836 to $9.788\ \mathrm{kA_{rms}}$, while the residual inducing current decreased from 3.103 to $2.220\ \mathrm{kA_{rms}}$, corresponding to a reduction of 28.44%.

The resulting maximum pipeline-to-earth voltages are reported in Table 8.6.

Table 8.6: Maximum pipeline-to-earth voltages for the LP and MP pipelines for the one- and two-ECC configurations under the representative L2-to-earth fault.

Pipeline	V_{max}, *1 ECC* [V_{rms}]	ξ_{max}, *1 ECC [-]*	V_{max}, *2 ECCs* [V_{rms}]	ξ_{max}, *2 ECCs [-]*	*Reduction [%]*
LP	202.205	1.000	149.479	1.000	26.08
MP	171.858	1.000	121.352	1.000	29.39

The two-ECC arrangement reduced the maximum pipeline-to-earth voltage from 202 to 150 V_{rms} for the LP pipeline and from 172 to 121 V_{rms} for the MP pipeline. The corresponding reductions were 26.08% and 29.39%, respectively. Both maxima occurred at the end of the reconstructed interference zone, at $\xi = 1$. The normalised longitudinal coordinate refers only to the reconstructed interference zone and excludes the external pipeline continuations used to represent the boundary conditions.

The two-ECC voltage profile remained lower over the entire analysed length for both pipelines, with the absolute reduction increasing towards the position of the maximum voltage.

The second ECC provides an additional metallic return path for the earth-fault current. The residual inducing-current fraction decreased from 28% to 20% in the La Pianta Primary Substation–joint bay section and from 26.2% to 18.6% in the joint bay – SCRI substation section. This behaviour is consistent with the reduction in the calculated pipeline voltages and confirms the mitigation of inductive coupling. The voltage reduction is not directly proportional to $|I_{\mathrm{ind}}|$, as it also depends on the route geometry, mutual impedances and pipeline boundary conditions.

The two-ECC arrangement and the representative L2-to-earth fault were retained for the subsequent sensitivity analysis of the pipeline boundary conditions.

8.4 Pipeline boundary-condition sensitivity and surge-arrester response

The sensitivity analysis investigated the effects of the unknown external pipeline continuations and the possible operation of the terminal surge arresters. The pipeline terminal representations defined in Section 8.2.3 were retained throughout the analysis.

The external continuation lengths at the sending and ending terminals, L_{S} and L_{E}, were varied independently over 0, 250, 500, 1000 and 2000 m. The same pair of continuation lengths was assigned to the LP and MP pipelines. Each simulation initially considered the Open–Open condition. The calculated voltage at each terminal was compared with the surge-arrester firing threshold equal to $V_{\mathrm{th}} = 70\ \mathrm{V_{rms}}$.

Because no device-specific characteristic was available, the surge arresters were represented using the blocking and conducting terminal conditions defined in Section 8.2.3. At each steady-state update, all terminal surge arresters whose voltage exceeded the operating threshold in the preceding simulation were assigned the conducting-state representation. Terminals containing an insulating joint remained open as the induced voltage is always below the longitudinal surge-arrester firing threshold (350 V_{rms}).

The pipeline-voltage distribution was then recalculated and any remaining open terminals equipped with a surge arrester were checked against the same threshold. The procedure was repeated until no additional arrester operation was required. Consequently, when both terminal voltages exceeded the threshold in the same simulation, both arresters were assigned the conducting state directly and no forced one-arrester intermediate condition was introduced.

Surge-arrester switching was not simulated dynamically. Each terminal configuration was represented by a separate steady-state ATP-EMTP simulation. The simultaneous state update therefore defines the adopted modelling procedure and does not represent the actual operating times of the devices.

All simulations retained the two-ECC arrangement and the L2-to-earth fault at the Mobile User Substation terminal of the second temporary configuration. The following sections examine the initial Open–Open condition and the subsequent terminal states determined through the adopted operating procedure.

8.4.1 Open–Open pipeline-terminal screening

The initial screening was performed under the Open–Open condition defined in Section 8.2.3. The continuation lengths L_S and L_E were varied independently over 0, 250, 500, 1000 and 2000 m, resulting in 25 combinations for each pipeline. The Open–Open terminal voltages and the corresponding threshold exceedances are summarised in Figure 8.4.

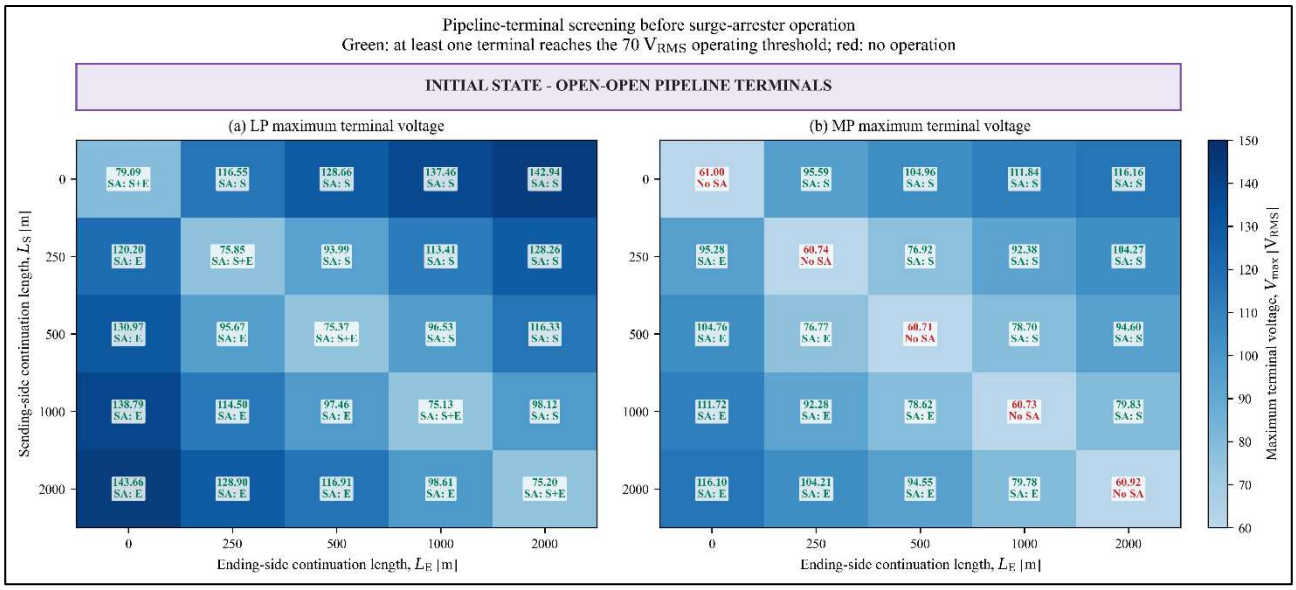


Figure 8.4: Maximum terminal pipeline-to-earth voltages under the Open–Open condition as functions of the sending- and ending-side continuation lengths. Green annotations identify terminals at which the 70 V_{RMS} operating threshold is exceeded; red annotations indicate that no arrester operation is required.

Equal continuation lengths produced the lowest terminal voltages. For the LP pipeline, however, the threshold was exceeded at both terminals in all five equal-length cases. In each of the 20 asymmetric cases, it was exceeded at one terminal: S for $L_S < L_E$, and E for $L_S > L_E$. Arrester operation was therefore required in all 25 LP configurations.

For the MP pipeline, the five equal-length cases remained below the threshold. All 20 asymmetric cases exceeded it at one terminal, following the same dependence on the continuation-length asymmetry. The maximum Open–Open terminal voltages were $144\,\mathrm{V_{rms}}$ for LP at $L_S = 2000\,\mathrm{m}, L_E = 0\,\mathrm{m}$, and $116\,\mathrm{V_{rms}}$ for MP at $L_S = 0\,\mathrm{m}, L_E = 2000\,\mathrm{m}$. The corresponding longitudinal voltage-profile envelopes are shown in Figure 8.5.

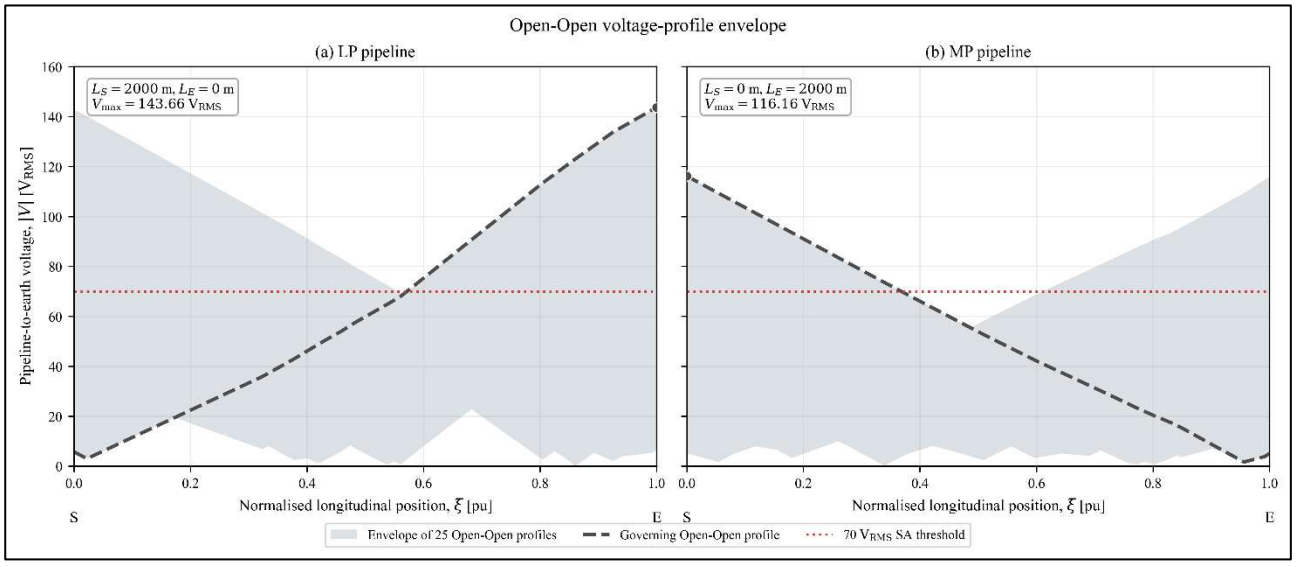


Figure 8.5: Envelope of the longitudinal pipeline-to-earth voltage profiles under the Open–Open condition, together with the governing profile for each pipeline.

The profile envelopes confirm that the terminal response is governed mainly by the asymmetry between $L_S$and L_E. According to the adopted state-update rule, the five equal-length cases pass directly to a condition with both LP arresters conducting, since both LP terminal voltages already exceed the threshold in the Open–Open solution. The MP terminals remain Open–Open. The 20 asymmetric cases instead proceed through an intermediate state with one operated arrester at each pipeline.

8.4.2 Pipeline response after surge-arrester operation

The operated arresters were represented using the conducting terminal condition defined in Section 8.2.3. Two operating sequences were considered.

In the five equal-length cases, both LP terminals already exceeded the threshold under the Open–Open condition. Both LP arresters were therefore applied directly, without an intermediate one-arrester state. The MP terminals remained Open–Open.

In the 20 asymmetric cases, the LP and MP arresters on the initially critical side were first represented in the conducting state. Recalculation showed that the opposite LP and MP terminals exceeded 70 V_{rms} in every case. The final state therefore included conducting arresters at both ends of both pipelines. The intermediate and final terminal states obtained through the adopted operating procedure are summarised in Figure 8.6.

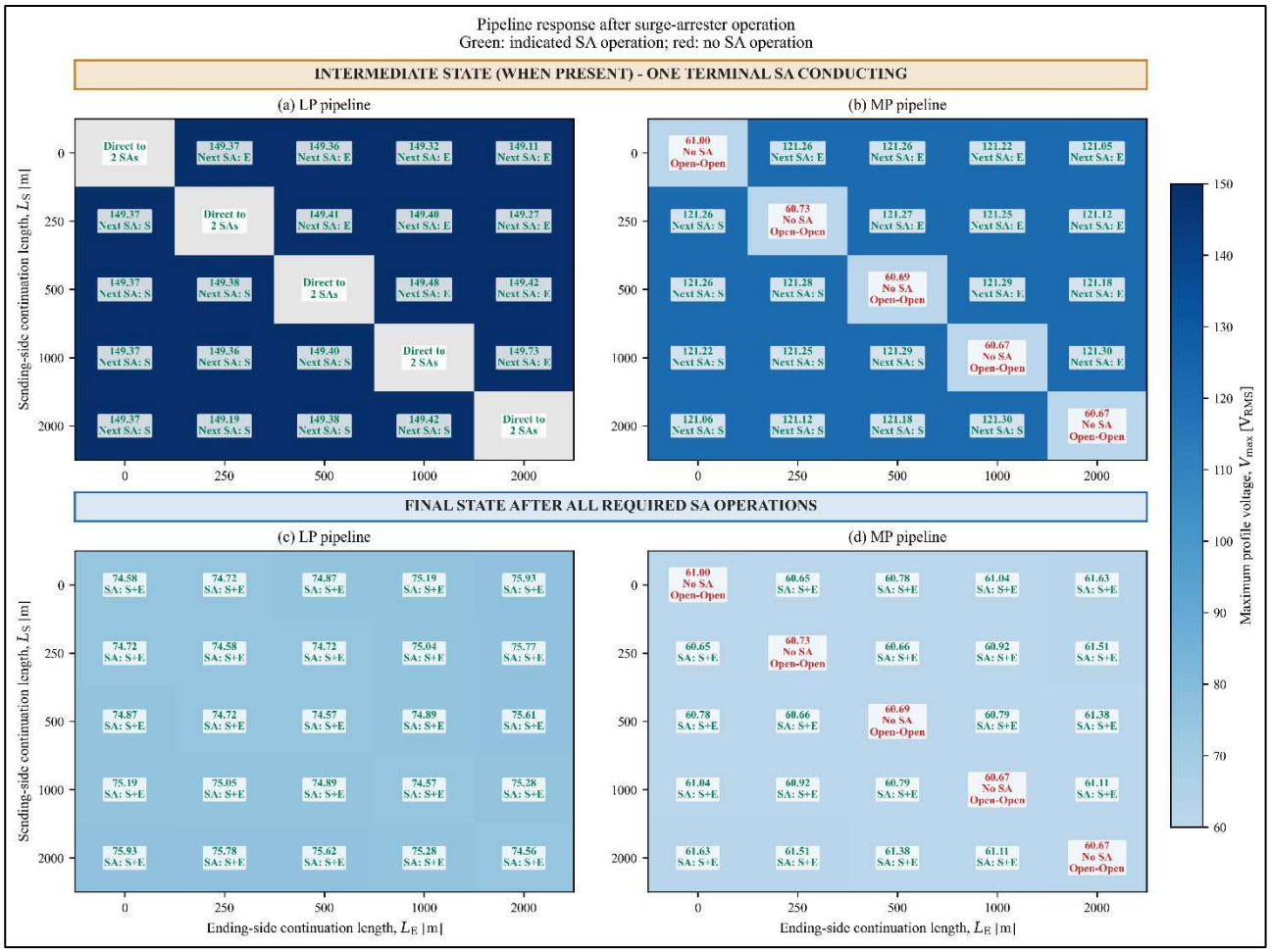


Figure 8.6: Maximum longitudinal pipeline-to-earth voltages in the intermediate state, where present, and in the final state after all required surge-arrester operations. Green annotations identify the required or active arrester condition, while red annotations indicate that no operation occurs. The equal-length LP cases pass directly to the final state with both arresters conducting. All panels use the same voltage scale.

The nearly uniform colours of the intermediate- and final-state heatmaps indicate that surge-arrester operation strongly reduces the sensitivity of the maximum pipeline voltage to L_S and L_E. In the intermediate state, the total variation was limited to 0.62 V for LP and 0.25 V for MP. In the final state, it remained below 1.37 V for LP and 0.99 V for MP.

In the intermediate state, the voltage maximum moved towards the opposite open terminal. The resulting maxima ranged from 149.11 to 149.73 V_{rms} for LP and from 121 to 121 V_{rms} for MP. This redistribution caused the second arrester to operate in all 20 asymmetric cases.

After all required operations, the maximum voltages ranged from 74.56 to 75.93 V_{rms} for LP and from 60.65 to 62 V_{rms} for MP. The highest final values for both pipelines occurred for $L_S = 2000$ m, $L_E = 0$ m. The successive voltage profiles for the governing final-state configuration are compared in Figure 8.7.

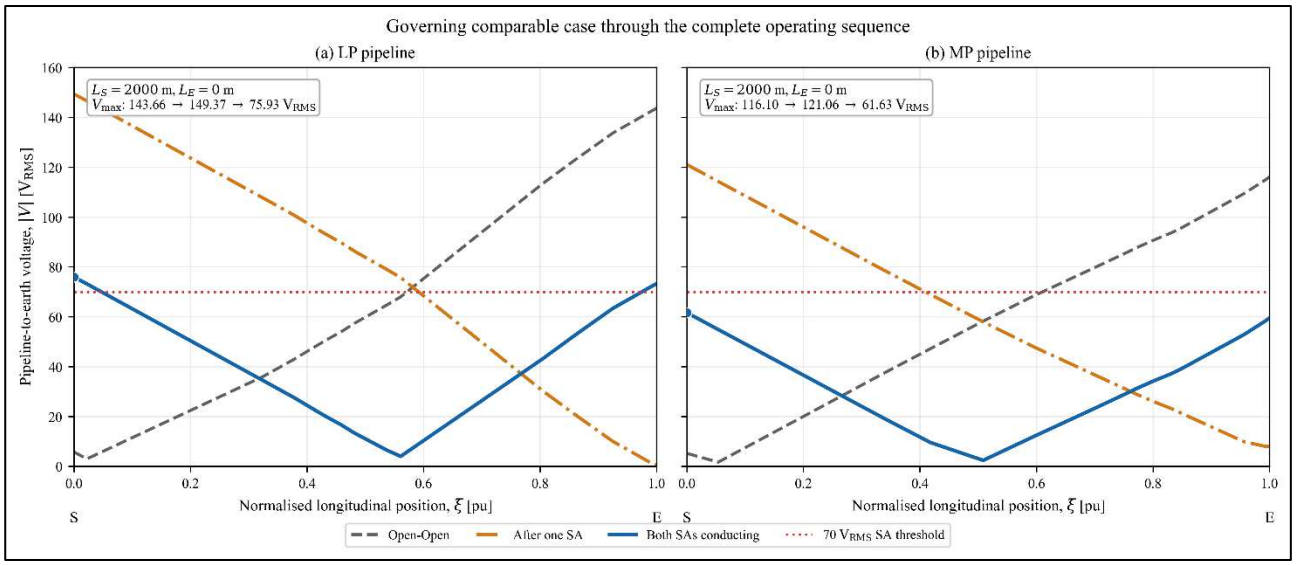


Figure 8.7: Longitudinal pipeline-to-earth voltage profiles for the governing final configuration under the Open–Open condition, after the first arrester operation and after operation of both terminal arresters.

For the governing configuration, the LP maximum changed according to

$$144 \longrightarrow 149 \longrightarrow 76\ \mathrm{V_{rms}}$$

whereas the corresponding MP values were

$$116 \longrightarrow 121 \longrightarrow 62\ \mathrm{V_{rms}}$$

Operation of only one terminal arrester therefore increased the maximum voltage, whereas operation of both arresters reduced it by approximately 49% relative to the intermediate state. Although the final LP-pipeline profile remains locally above 70 $\mathrm{V_{rms}}$, no additional terminal-arrester operation is required. The adopted operating threshold applies to the pipeline voltage at the terminals where the arresters are installed, rather than to internal points along the route.

Finally, the longitudinal surge arresters were checked over the complete set of analysed configurations. The maximum voltage relevant to their operation was $150\ \mathrm{V_{rms}}$, obtained in the intermediate state, and remained below their firing voltage of $350\ \mathrm{V_{rms}}$. The current through these devices was also verified in all the analysed configurations and remained below the admissible value of 230 A for the 350 ms fault duration. The longitudinal surge arresters were therefore not expected to operate and their current capability was not exceeded under any of the analysed conditions.

8.4.3 Sensitivity to the conducting-state terminal resistance

The sensitivity analysis was performed for the governing final-state configuration $L_{\mathrm{S}} = 2000$ m, $L_{\mathrm{E}} = 0$ m. The equivalent conducting-state terminal resistance was varied over $R_{\mathrm{term,on}}$ = 5 ,10, 15 Ω.

Three terminal states were considered: both terminal SAs blocking, the ending-side SA conducting and both terminal SAs conducting. The Open–Open result is independent of $R_{\mathrm{term,on}}$ and is therefore reported only once. The maximum pipeline voltages are summarised in Table 8.7.

Table 8.7: Sensitivity of the maximum pipeline-to-earth voltages to the equivalent conducting-state resistance for the governing final-state configuration $L_S = 2000\ m$, $L_E = 0\ m$.

Terminal state	$R_{term,on}$ *[Ω]*	$V_{max,LP}$ *[V_{rms}]*	$V_{max,MP}$ *[V_{rms}]*
Both terminal SAs blocking (Open–Open)	—	143.657	116.095
Ending-side SA conducting	5	149.384	121.274
	10	149.116	121.054
	15	148.674	120.692
Both terminal SAs conducting	5	78.046	63.347
	10	75.928	61.635
	15	75.319	61.141

In the intermediate state, V_{max} varied by only $0.71\ \mathrm{V_{rms}}$ for LP and $0.58\ \mathrm{V_{rms}}$ for MP. The corresponding terminal currents also remained nearly constant. In the final state, increasing $R_{\mathrm{term,on}}$ from 5 to 15 Ω reduced V_{max} by approximately 3.5% for both pipelines, while the maximum terminal currents decreased from 14.365 to $4.928\ \mathrm{A_{rms}}$ for LP and from 11.659 to $4.000\ \mathrm{A_{rms}}$ for MP.

The calculated pipeline voltages are therefore weakly dependent on the assumed conducting-state resistance, whereas the terminal current is significantly affected. The voltage-related conclusions obtained with the reference value of 10 Ω remain valid over the investigated range.

8.5 Touch-voltage and conductive-coupling assessment

Two additional safety checks were performed. The first compares the maximum MP-pipeline voltage with the applicable touch-voltage limits. The second assesses the conductive coupling produced by the current dissipated through the joint-bay earthing system. Only the MP pipeline was considered because it is the pipeline running parallel to the joint bay.

Both assessments refer to the two-ECC arrangement, the L2-to-earth fault at the SCRI substation terminal and the adopted fault-clearing time of $t_F = 0.35$ s.

8.5.1 Touch-voltage assessment of accessible pipeline-connected components

Accessible metallic components electrically connected to the MP pipeline, such as vents and valves, were conservatively assumed to reach the pipeline potential.

For the adopted fault duration, CEI EN 50443 specifies an admissible fault-induced interference voltage of $U_L = 1000\ V_{rms}$ at locations normally accessible to electrically instructed persons [4].

The permissible touch voltage was evaluated in THOR 50Hz as a function of the fault duration, according to CEI EN 50522 [8]. For $t_F = 0.35$ s, the value obtained without accounting for additional resistances was $U_{Tp} = 345.95\ \mathrm{V_{rms}}$. This value was obtained without accounting for footwear or other additional resistances and was adopted as the more restrictive criterion. Compliance with this limit therefore also ensures compliance when additional resistances are included.

The highest MP-pipeline voltage obtained over all the analysed terminal configurations was $V_{MP,max} = 121.303\ V_{rms}$.

It occurred for $L_S = 2000\ m$ and $L_E = 1000\ m$, with the MP ending-terminal arrester conducting and the sending terminal open. The maximum was not located at the joint bay. Its application to accessible components in the joint-bay area is therefore conservative.

The governing voltage, applicable limits and assessment outcome are summarised in Table 8.8.

Table 8.8: Touch-voltage assessment of accessible metallic components connected to the MP pipeline.

Quantity	***Value***
Fault-clearing time, t_F	0.35 s
Maximum MP-pipeline voltage, $V_{MP,max}$	121.303 V_{rms}
CEI EN 50443 limit for electrically instructed persons	1000 $\mathrm{V_{rms}}$
CEI EN 50522 permissible touch voltage, U_{Tp}	345.95 $\mathrm{V_{rms}}$
Ratio $V_{MP,max}/U_{Tp}$	35.1%
Assessment	Satisfied

The governing comparison is therefore

$$V_{\mathrm{MP,max}} = 121.303\ \mathrm{V_{rms}} < U_{Tp} = 345.95\ \mathrm{V_{rms}}.$$

The touch-voltage assessment is therefore satisfied without relying on footwear or other additional resistances. The assessment is deliberately conservative because it applies the maximum MP-pipeline voltage calculated over the entire analysed route to the joint-bay area, although this maximum occurs elsewhere, and compares it with the touch-voltage limit obtained without additional protective resistances. It therefore represents an upper-bound safety screening rather than the reconstruction of a specific local contact condition.

8.5.2 Conductive-coupling assessment at the joint bay

A separate THOR50Hz calculation was performed to assess the soil-potential rise produced by the current injected through the joint-bay earthing system and its possible conductive interaction with the MP pipeline.

The joint-bay earth current was obtained from the ATP-EMTP simulation results. Its magnitude decreased from $209\ \mathrm{A_{rms}}$ with one ECC to $158\ \mathrm{A_{rms}}$ with two ECCs, corresponding to a reduction of about 24%. The two-ECC configuration was retained because it represents the reference mitigation arrangement adopted for the subsequent assessments. The earthing geometry and the remaining electrical parameters were those already defined in Section 8.2.2.

The minimum distance between the long edge of the joint bay and the MP pipeline is 13 m. A distance of 10 m was conservatively adopted for the assessment. The adopted inputs and results are summarised in Table 8.9.

Table 8.9: Conductive-coupling assessment between the joint-bay earthing system and the MP pipeline.

Quantity	***Value***
Analysed ECC configuration	2 ECCs
Injected joint-bay earth current, $I_{E,JB}$	$158\ \mathrm{A_{rms}}$
Joint-bay equivalent earthing resistance	5.6 Ω
Soil resistivity, ρ_e	100 Ωm
Fault duration, t_F	0.35 s
Minimum MP-pipeline distance from the joint-bay edge	13.0 m
Adopted assessment distance	10.0 m
Maximum interpolated soil potential at the assessment distance	$221\ \mathrm{V_{rms}}$
CEI EN 50522 permissible touch voltage, U_{Tp}	$345.95\ \mathrm{V_{rms}}$
Ratio $U_{soil,max}/U_{Tp}$	63.9%
Assessment	Satisfied

The governing comparison is therefore

$$U_{\mathrm{soil,max}}(10\ \mathrm{m}) = 221\ \mathrm{V_{rms}} < U_{Tp} = 345.95\ \mathrm{V_{rms}}.$$

The permissible touch-voltage limit is satisfied at an assessment distance smaller than the actual minimum pipeline separation. The soil-potential rise generated by the joint-bay earthing system is therefore non-critical for the analysed configuration. On this basis, conductive coupling was not represented explicitly in the ATP-EMTP cable–pipeline model, which was developed to assess inductive interference, but was verified separately through the THOR50Hz calculation.

9. ANALYTICAL PIPELINE–EARTH MODELLING AND VERIFICATION USING CIGRÉ TECHNICAL BROCHURE 95

This chapter develops a sectional frequency-domain model of the LP and MP pipeline–earth circuits based on Appendix H of CIGRE Technical Brochure 95. The conductor-current phasors obtained from the ATP-EMTP simulations in Chapter 8 are used to reconstruct the distributed induced electromotive force and calculate the pipeline voltage and current profiles. The implementation is verified against ATP-EMTP for different terminal conditions, both with and without coating conductance.

9.1 Method based on Appendix H of CIGRÉ Technical Brochure 95

Appendix H represents the coated pipeline as a distributed electrical circuit characterised by its longitudinal impedance, transverse admittance and induced electromotive force. The following sections introduce the governing equations, the representative terminal conditions and the sectional extension required for the non-uniform La Spezia routes.

9.1.1 Governing equations of the pipeline–earth circuit

Let $\bar{V}(x)$ denote the complex pipeline-to-earth voltage and $\bar{I}(x)$ the longitudinal current flowing along the pipeline. Their spatial variation is governed by:

$$\frac{\mathrm{d}\bar{V}(x)}{\mathrm{d}x} + z\,\bar{I}(x) - \bar{E}(x) = 0 \tag{9.1}$$

$$\frac{\mathrm{d}\bar{I}(x)}{\mathrm{d}x} + y\,\bar{V}(x) = 0 \tag{9.2}$$

where:

- x is the longitudinal coordinate measured along the pipeline, [m];
- $\bar{V}(x)$ is the complex pipeline-to-earth voltage phasor at coordinate x, [V];
- $\bar{I}(x)$ is the complex longitudinal pipeline-current phasor at coordinate x, [A];
- z is the longitudinal impedance per unit length of the pipeline–earth circuit, [Ω/m];
- y is the transverse admittance per unit length between the pipeline and earth, [S/m];
- $\bar{E}(x)$ is the longitudinal induced electromotive force per unit length at coordinate x, [V/m].

The longitudinal impedance includes the internal impedance of the metallic pipe and the external earth-return contribution:

$$z = z_{\mathrm{int}} + z_{\mathrm{ext}} \tag{9.3}$$

where:

- z_{int} is the internal impedance per unit length of the metallic pipeline, [Ω/m];

- z_{ext} is the external earth-return impedance per unit length, $[\Omega/\text{m}]$.

The internal term depends on the geometry and electromagnetic properties of the pipeline, whereas the external term accounts for the surrounding electromagnetic field and the current return through the soil. The transverse admittance includes both conductive and capacitive contributions:

$$y = G + j\omega C \tag{9.4}$$

where:

- G is the coating conductance per unit length between the pipeline and earth, $[\text{S/m}]$;
- C is the pipeline-to-earth capacitance per unit length, $[\text{F/m}]$;
- $\omega = 2\pi f$ is the angular frequency, $[\text{rad/s}]$;
- f is the system frequency, [Hz];
- j is the imaginary unit, $[-]$.

Following the approximation adopted in Appendix H for a coated cylindrical pipeline, the transverse-admittance components are expressed as:

$$G = \frac{\pi D}{r_c}, \qquad C = \frac{\varepsilon_0 \varepsilon_r \pi D}{\delta_c} \tag{9.5}$$

where:

- D is the external diameter of the metallic pipeline, [m];
- r_c is the coating specific resistance, $[\Omega\ \text{m}^2]$;
- δ_c is the coating thickness, [m];
- ε_r is the relative permittivity of the coating, $[-]$;
- ε_0 is the vacuum permittivity, $[\text{F/m}]$.

The conductance G represents the resistive leakage through the coating, whereas $j\omega C$ accounts for the capacitive current exchanged between the pipeline and the surrounding soil. The distributed electromotive force $\bar{E}(x)$ represents the inducing action of the electrical system. It depends on the currents flowing in the interfering conductors and on their mutual impedances with the pipeline. Its value may vary along the route as a result of changes in conductor currents, relative geometry and soil properties.

9.1.2 Uniform exposure and terminal conditions

For a uniform parallel exposure, the quantities z, y and $\bar{E}$ may be assumed constant along the considered length. The governing equations then have the same mathematical structure as those of a distributed transmission line. The characteristic impedance of the pipeline–earth circuit is defined as:

$$Z_c = \sqrt{\frac{z}{y}} \tag{9.6}$$

where Z_c is the characteristic impedance of the uniform pipeline–earth circuit, [Ω].

The corresponding propagation constant is:

$$\gamma = \sqrt{zy} \tag{9.7}$$

where γ is the complex propagation constant, $[\mathrm{m}^{-1}]$.

The real and imaginary parts of γ describe the attenuation and phase variation of voltage and current along the pipeline, respectively. The characteristic impedance Z_c represents the impedance seen at the entrance of a sufficiently long and uniform continuation of the pipeline. The voltage and current distributions also depend on the terminal impedances Z_A and Z_B, where:

- Z_A is the impedance connected between the first end of the exposed pipeline section and earth, [Ω];
- Z_B is the impedance connected between the opposite end of the exposed pipeline section and earth, [Ω].

Appendix H considers three representative configurations [3]. For a pipeline continuing beyond the exposed section on both sides, hereafter denoted as the continuation–continuation configuration (CC):

$$Z_A = Z_B = Z_c \tag{9.8}$$

For a pipeline continuing on side A and open-circuited at side B, denoted as the continuation–open configuration (CO):

$$Z_A = Z_c, Z_B \to \infty \tag{9.9}$$

For a pipeline ideally grounded at side A and continuing beyond the exposed section at side B, denoted as the grounded–continuation configuration (GC):

$$Z_A = 0, Z_B = Z_c \tag{9.10}$$

The letters in each label refer to the boundary conditions applied at sides A and B, respectively. The two asymmetric configurations may be mirrored by exchanging Z_A and Z_B.

9.1.3 Extension to non-uniform routes

Actual interference configurations are generally characterised by variations in cable–pipeline separation, conductor arrangement and route orientation. Appendix H therefore extends the uniform-exposure formulation by dividing the overall zone of influence into consecutive sections within which the electrical and geometrical parameters may be considered approximately constant [3].

Each section is represented by an equivalent π-cell containing the longitudinal pipeline impedance, the transverse pipeline-to-earth admittance and the induced electromotive force. Connecting the cells in sequence provides the voltage and current distributions along non-uniform routes, including parallel sections, approaches, diverging sections and crossings. The numerical construction and solution of this sectional representation are described in Section 9.2.

9.2 Numerical implementation of the sectional model

The Appendix H formulation was implemented in GNU Python as a complex frequency-domain sectional model. The LP and MP pipelines were represented separately using the route discretisation adopted in Chapter 8. Each section was assigned a longitudinal impedance, a transverse admittance and an induced electromotive force.

The main calculation uses the physical pipeline–earth parameters defined by the CIGRE formulation. The same sectional structure is subsequently reproduced in ATP-EMTP using equivalent electrical parameters for the numerical verification.

9.2.1 Route discretisation and sectional parameters

Each pipeline route was divided into a sequence of N sections. The section boundaries coincide with the nodes introduced in the ATP model, so that the voltages calculated with the two approaches can be compared directly at corresponding positions. For each section i, of length L_i, the following quantities were defined:

$$Z_i = z_i L_i \tag{9.11}$$

$$Y_i = y_i L_i \tag{9.12}$$

$$\bar{e}_i = \bar{E}_i L_i \tag{9.13}$$

where:

- i is the section index, with $i = 1, \dots, N$, $[-]$;
- N is the total number of sections used to represent the considered pipeline route, $[-]$;
- L_i is the length of section i, $[\mathrm{m}]$;
- z_i is the longitudinal pipeline–earth impedance per unit length of section i, $[\Omega/\mathrm{m}]$;
- y_i is the transverse pipeline-to-earth admittance per unit length of section i, $[\mathrm{S/m}]$;

- $\bar{E}_i$ is the complex longitudinal electromotive force induced per unit length in section i, [V/m];
- Z_i is the longitudinal series impedance of section i, [Ω];
- Y_i is the total transverse admittance of section i, [S];
- $\bar{e}_i$ is the complex electromotive force induced over section i, [V].

Each section was represented by an equivalent π-cell. The longitudinal impedance Z_i and induced-voltage source $\underline{e}_i$were included in the series branch, whereas the total transverse admittance Y_i was divided equally between the two terminal nodes as $Y_i/2$.

In the main Appendix H application, z_i and y_i were calculated from the adopted physical properties of the pipeline, coating and soil. An electrically equivalent parameter set was subsequently imposed in ATP-EMTP solely for numerical verification.

The LP and MP pipelines were solved independently. Direct electromagnetic coupling between the two pipelines was not included as an additional mutual branch. Each pipeline was instead subjected to the electromotive force induced by the electrical conductors represented in the corresponding section.

9.2.2 Reconstruction of the distributed induced electromotive force

The longitudinal electromotive force acting on each pipeline section was reconstructed from the currents flowing in the conductors of the electrical system and from their mutual impedances with the pipeline. For section i, the induced electromotive force per unit length was calculated as:

$$\bar{E}_i = -\sum_{q \in \mathcal{C}_i} z_{pq,i}\, \bar{I}_{q,i} \tag{9.14}$$

where:

- p identifies the pipeline under consideration, corresponding to either the LP or MP pipeline, [pu];
- q is the index of an inducing conductor, [pu];
- $\mathcal{C}_i$ is the set of inducing conductors represented in section i, [pu];
- $z_{pq,i}$ is the mutual impedance per unit length between pipeline p and conductor q in section i, [Ω/m];
- $\bar{I}_{q,i}$ is the complex RMS current at 50 Hz flowing in conductor q within section i, [A];
- $\bar{E}_i$ is the resulting complex electromotive force induced per unit length in the considered pipeline section, [V/m].

Depending on the analysed section, the inducing conductors included the cable cores, metallic screens and earth-continuity conductors. In the Appendix H formulation, the current phasors of the interfering conductors are prescribed input quantities. In this work, they were obtained from the ATP-

EMTP simulations of the second temporary configuration defined in Chapter 8. The conductor-to-pipeline mutual impedances and the corresponding distributed electromotive-force profiles were then reconstructed analytically and used to solve the pipeline-to-earth voltage and longitudinal-current distributions.

Within each section, the geometry and conductor currents were assumed to be sufficiently uniform for $\underline{E}_i$ to be represented by a constant value. Spatial variations in cable–pipeline separation, conductor arrangement and current distribution were accounted for by assigning different induced electromotive forces to consecutive sections.

The negative sign in Equation (9.14) follows from the adopted voltage, current and longitudinal-coordinate reference directions. A consistent orientation was maintained along the complete pipeline route and checked through the comparison of the complex ATP-EMTP and sectional-model voltage profiles.

9.2.3 Assembly and solution of the nodal system

The N pipeline sections define $N + 1$ nodal positions. Section i connects node i to node $i + 1$, and its longitudinal current is assumed positive in the direction of increasing node index. Integration of the longitudinal pipeline equation over section i gives:

$$\bar{V}_{i+1} - \bar{V}_i + Z_i \bar{I}_i - \bar{e}_i = 0 \tag{9.15}$$

from which:

$$\bar{I}_i = \frac{\bar{V}_i - \bar{V}_{i+1} + \bar{e}_i}{Z_i} \tag{9.16}$$

where:

- $\bar{V}_i$ and $\bar{V}_{i+1}$ are the complex pipeline-to-earth voltages at the initial and final nodes of section i, respectively, [V];
- $\bar{I}_i$ is the complex longitudinal current flowing through section i from node i to node $i + 1$, [A];
- Z_i is the longitudinal series impedance of section i, [Ω];
- $\bar{e}_i$ is the complex electromotive force induced over section i, [V].

The current-balance equation was written at every pipeline node by combining the currents in the adjacent longitudinal branches, the shunt currents associated with the sectional admittances, any local grounding current and the contribution of the terminal conditions.

For an internal node n, shared by sections $n - 1$ and n, the pipeline-to-earth shunt admittance is:

$$Y_{\mathrm{sh},n} = \frac{Y_{n-1}}{2} + \frac{Y_n}{2}, \qquad n = 2, \dots, N \tag{9.17}$$

where:

- n is the pipeline-node index, $[-]$;
- Y_{n-1} and Y_n are the total transverse admittances of the two sections adjacent to node n, [S];
- $Y_{\mathrm{sh},n}$ is the resulting transverse admittance between internal node $n$and earth, [S].

If a local grounding impedance $Z_{g,n}$ is connected at the same node, the total nodal shunt admittance becomes:

$$Y_{\mathrm{node},n} = Y_{\mathrm{sh},n} + \frac{1}{Z_{g,n}} \tag{9.18}$$

where:

- $Z_{g,n}$ is the local grounding impedance connected between node n and earth, [Ω];
- $Y_{\mathrm{node},n}$ is the total shunt admittance connected to node n, including both the distributed pipeline admittance and the local grounding contribution, [S].

The complete set of nodal equations was assembled in matrix form as:

$$[Y]\,[\bar{V}] = [\mathrm{I_n}] \tag{9.19}$$

where:

- $[Y]$ is the complex nodal-admittance matrix of the sectional pipeline model, whose elements are expressed in [S];
- $[\bar{V}]$ is the column vector containing the unknown complex pipeline-to-earth nodal voltages, whose elements are expressed in [V];
- $[I_n]$ is the column vector containing the equivalent complex nodal-current injections associated with the distributed electromotive-force sources, whose elements are expressed in [A].

The system was solved directly in the complex domain at 50 Hz. Once the nodal voltages had been determined, the longitudinal current in each section was reconstructed using Equation (9.16).

The terminal conditions were imposed through the impedances Z_A and Z_B connected between the first and last pipeline nodes and earth. The three configurations defined in Section 9.1.2 were analysed: bilateral characteristic-impedance continuation, unilateral continuation with an open opposite end, and ideal grounding at one end with characteristic-impedance continuation at the other.

To isolate the influence of the terminal conditions, the same distributed induced-electromotive-force profile was applied to the CC, CO and GC configurations. Figure 9.1 shows the resulting pipeline-to-earth voltage-magnitude profiles calculated using the complete Appendix H model, including the coating conductance.

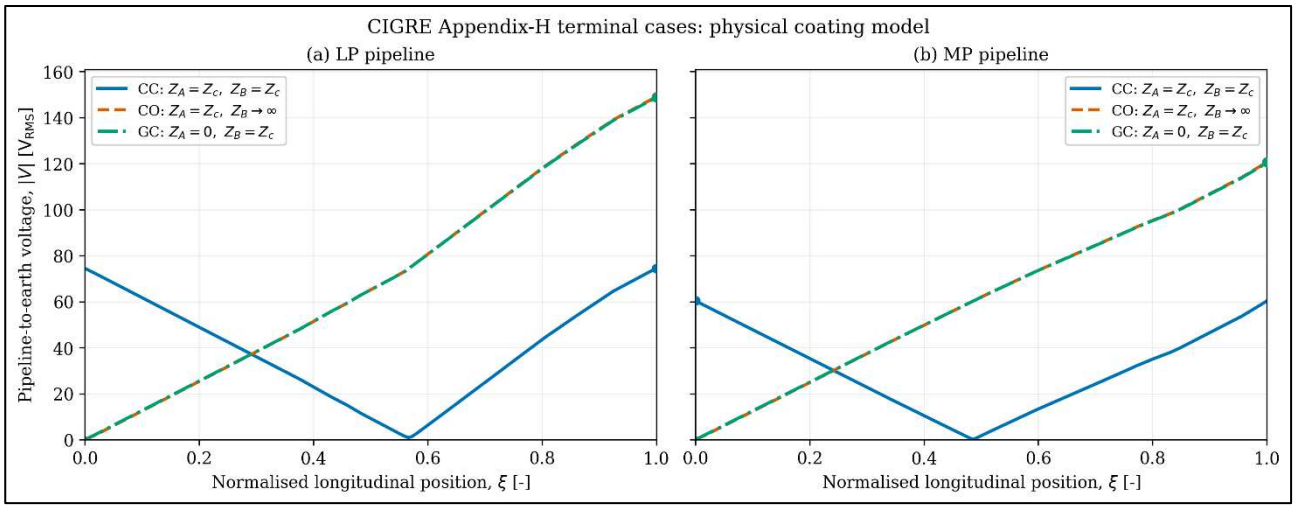


Figure 9.1: Pipeline-to-earth voltage-magnitude profiles calculated using the complete Appendix H model for the CC, CO and GC terminal configurations: (a) LP pipeline and (b) MP pipeline. The same distributed induced-electromotive-force profile is applied in all three cases, and the longitudinal coordinate is normalised over the reconstructed interference zone.

9.3 Numerical verification against ATP-EMTP

The Appendix H implementation was verified against ATP-EMTP for the CC, CO and GC terminal configurations defined in Section 9.1.2. For both the LP and MP pipelines, the RMS pipeline-to-earth voltage magnitudes were compared at observation nodes common to the two models.

The verification considered both the original ATP-EMTP representation and an extended formulation including coating conductance. For each configuration, the conductor-current phasors were independently extracted from ATP-EMTP and used as inputs to the corresponding analytical calculation. The verification setup, comparison criteria and resulting errors are presented in Sections 9.3.1 and 9.3.2.

9.3.1 Verification Setup and Comparison Criteria

The verification considered the CC, CO and GC configurations defined in Section 9.1.2, separately for the LP and MP pipelines. In ATP-EMTP, continuation, open-circuit and grounded terminal conditions were represented by the corresponding characteristic-impedance termination, open circuit and direct connection to ideal earth, respectively.

Two verification levels were examined. In the first, the original ATP-EMTP model, which includes coating capacitance but neglects coating conductance, was compared with the Appendix H formulation by setting $G = 0$. In the second, distributed pipeline-to-earth resistances were added at the ATP-EMTP pipeline nodes, while the complete transverse admittance was represented according to Eq. (9.4).

For each verification level, the characteristic impedance Z_c, expressed in Ω, was recalculated consistently and represented in ATP-EMTP by an equivalent series R-C or R-L branch at 50 Hz. The adopted components are reported in Table 9.1.

Table 9.1: Equivalent series components used in ATP-EMTP to reproduce the characteristic impedance Z_c at 50 Hz.

Admittance model	***Coating representation***	R_{series} ***[Ω]***	X_{series} ***[Ω]***
$G \neq 0$	Conductive and capacitive	12.5543	2.7837
$G = 0$	Capacitive only	14.3937	−1.6406

The positive reactance of the $G \neq 0$ model was represented by a series inductance, whereas the negative reactance of the $G = 0$ model was represented by a series capacitance.

For each of the six ATP-EMTP simulations, the conductor-current phasors were extracted independently and used as inputs to the corresponding Appendix H calculation. The voltage magnitudes were then compared at the common LP and MP observation nodes.

For node n, the absolute magnitude error was defined as

$$e_n = \left| \left| \underline{V}_{\mathrm{CIGRE,n}}' \right| - \left| \underline{V}_{\mathrm{ATP},n} \right| \right| \tag{9.20}$$

where:

- e_n is the absolute pipeline-to-earth voltage-magnitude error at node n, [V_{rms}];
- $\underline{V}_{\mathrm{CIGRE,n}}'$ is the complex RMS pipeline-to-earth voltage calculated using the Appendix H model at node n, [V_{rms}];
- $\underline{V}_{\mathrm{ATP},n}$ is the corresponding complex RMS pipeline-to-earth voltage obtained from ATP-EMTP, [V_{rms}];
- n is the observation-node index, with $n = 1, \ldots, N_{\mathrm{obs}}$, [−].

The maximum absolute error $e_{\max}$ is the maximum absolute pipeline-to-earth voltage-magnitude error over the common observation nodes, [V_{rms}]. It was calculated as

$$e_{\max} = \max_{n=1,\ldots,N_{\mathrm{obs}}} e_n \tag{9.21}$$

where N_{obs} is the total number of observation nodes common to the ATP-EMTP and Appendix H models, [−]. The maximum normalised error was defined as

$$\varepsilon_{\max} = 100 \frac{\max\limits_{n=1,\ldots,N_{\mathrm{obs}}} e_n}{\max\limits_{n=1,\ldots,N_{\mathrm{obs}}} \left| \underline{V}_{\mathrm{ATP},n} \right|} \tag{9.22}$$

where:

- $\varepsilon_{\max}$ is the maximum absolute error normalised by the maximum ATP-EMTP voltage, [%];

The maxima are evaluated over the N_{obs} observation nodes common to the two models.

9.3.2 Verification Results and Assessment

The numerical comparison is summarised in Table 9.2. Separate comparison plots were not included because the ATP-EMTP and Appendix H voltage profiles were virtually superimposed at the scale of the figures.

Table 9.2: Numerical verification of the Appendix H implementation against ATP-EMTP for the CC, CO and GC terminal configurations.

Admittance model	***Case***	***Pipeline***	$V_{max,ATP}$ $[V_{RMS}]$	$V_{max,CIGRE}$ $[V_{RMS}]$	e_{max} $[V_{RMS}]$	ε_{max} [%]
$G = 0$	CC	LP	74.64	74.59	0.058	0.078
		MP	60.60	60.45	0.145	0.239
	CO	LP	149.30	149.19	0.114	0.077
		MP	121.20	120.91	0.289	0.239
	GC	LP	149.20	149.09	0.114	0.076
		MP	121.12	120.83	0.289	0.238
$G \neq 0$	CC	LP	74.54	74.49	0.058	0.078
		MP	60.51	60.36	0.145	0.239
	CO	LP	149.09	148.98	0.115	0.077
		MP	121.01	120.72	0.290	0.240
	GC	LP	148.77	148.66	0.114	0.076
		MP	120.76	120.47	0.288	0.238

Across all twelve comparisons, the maximum absolute error did not exceed $0.290\ \text{V}_{\text{rms}}$, while the maximum normalised error did not exceed 0.240%. The agreement obtained for both $G = 0$ and $G \neq 0$ verifies the implementation of the coating admittance, terminal conditions and characteristic impedance Z_c. Including the coating conductance produced a slight reduction in the calculated voltages, with changes in the maximum values below approximately 0.30%. The original ATP-EMTP LCC representation includes the capacitive component of the coating admittance but does not represent its conductance explicitly. Although the latter was introduced through distributed pipeline-to-earth resistances, it did not materially affect the results. Neglecting the coating conductance is therefore acceptable for the analysed route and coating properties, although this conclusion should not be extended to pipelines with significantly lower coating resistance or degraded coatings.

The CC configuration produced approximately half the voltage obtained for CO and GC. With $G \neq 0$, the CC maximum exceeded the $70\ \text{V}_{\text{rms}}$ surge-arrester threshold only for the LP pipeline,

reaching $74.54\ V_{rms}$, while the MP maximum remained below the threshold at $60.51\ V_{rms}$. Both CO and GC exceeded the threshold on both pipelines. The CC condition represents an effective pipeline continuation and should not be interpreted as the operation of a protective device.

The LP pipeline remained the more critical of the two, and the maximum voltages occurred at the route extremities. A high pipeline-to-earth voltage does not alone establish a personnel hazard, which also depends on the accessibility of metallic components and the possible contact conditions.

The comparison verifies the numerical solution of the pipeline–earth circuit, but it does not constitute an experimental validation of the physical input data. The pipeline and coating properties remain assumed, while the conductor-current phasors are obtained from the ATP-EMTP model of the electrical system.

Once these phasors have been determined, retaining the complete representation of phase conductors, cable screens and ECCs provides no significant additional benefit for subsequent pipeline-only analyses. The residual inducing currents defined in Chapter 8 can be represented by equivalent sources located at the representative separation of each route section, consistently with the sectional approach of CIGRE Technical Brochure 95 [3].

This representation reduces the required segmentation of the cable connection and allows sensitivity analyses to be performed by modifying only the pipeline model. Its discretisation can be refined independently until the distances at the ends of each section become nearly equal, corresponding to d_1/d_2 approaching unity. In the adopted ATP-EMTP LCC model, the same refinement would require the corresponding subdivision and reparameterisation of the coupled cable–pipeline sections. The analytical formulation therefore provides a faster and more flexible approach for pipeline calculations and sensitivity analyses while retaining the inducing-current distribution obtained from the complete electrical-system model.

10. CONCLUSIONS

This thesis developed an integrated framework for assessing electromagnetic interference between high-voltage underground cable systems and nearby buried metallic pipelines. The work combined analytical earth-return formulations, preliminary screening methods, detailed ATP-EMTP simulations and an independent frequency-domain solution of the pipeline–earth circuit. Attention was given to earth-fault conditions, for which the current distribution among phase conductors, cable screens, earth-continuity conductors, earthing systems and soil governs both inductive and conductive interference.

The theoretical analysis showed that underground cable systems cannot be represented through the phase conductors alone. Cable screens and ECCs provide metallic return paths that modify the residual external magnetic field and the current injected into the soil. The pipeline response also depends strongly on its coating, electrical continuity and terminal conditions. Reliable interference calculations therefore require the electrical representation of both infrastructures, rather than only their geometrical separation.

The analytical study of mutual earth-return impedance supported the numerical approach adopted in the simulations. Pollaczek's formulation was used as the reference and compared with the Ametani/ATP, Wedepohl, CIGRÉ and ITU-T K.68 approximations. Over the complete 50 Hz parameter grid, the Ametani/ATP formulation produced a mean absolute percentage error of 0.1% and a maximum error of 0.56% in the mutual-impedance magnitude. The comparison confirms the consistency of the ATP-EMTP Line/Cable Constants routine with the analytical reference. The simplified formulations remain suitable for preliminary calculations, provided that their validity ranges are respected.

Two additional preliminary tools were developed for inductive- and conductive-interference screening. The first relates soil resistivity, cable–pipeline separation and normalised induced voltage, while the second estimates the ground-potential-rise influence distance through an equivalent hemispherical electrode. A compact interpolation model was also developed for the resistance of a representative 150 kV joint bay earthing system in two-layer soil. Its validation against an independent dataset produced a mean absolute percentage error of 1.3% and $R^2 = 0.996$. These tools provide initial order-of-magnitude assessments but do not replace the complete distributed model.

The main numerical application concerned the second temporary configuration of the 132 kV underground connection serving the La Spezia port area. The ATP-EMTP model included the upstream-network equivalent, phase conductors, metallic screens, ECCs, local earthing systems, non-uniform cable–pipeline geometry and the terminal conditions of the low- and medium-pressure gas

pipelines. Preliminary simulations identified the single phase to ground fault at the Mobile User Substation as the representative condition, with an adopted fault duration of 0.35 s.

The comparison between the documented one-ECC arrangement and the candidate two-ECC arrangement demonstrated the effectiveness of the additional metallic return path. The residual inducing current decreased by 28.11% in the La Pianta Primary Substation–joint bay section and by 28.44% in the Joint Bay–Mobile User Substation section. Under the fixed pipeline boundary conditions adopted for this comparison, the maximum pipeline-to-earth voltage decreased from 202 V_{rms} to 150 V_{rms} for the LP pipeline and from 172 V_{rms} to 121 V_{rms} for the MP pipeline. The corresponding reductions were 26% and 30%. The second ECC therefore provides effective mitigation of inductive coupling, although the assessed arrangement remains a proposed alternative rather than an approved project configuration.

The sensitivity analysis showed that the pipeline terminal conditions are among the most influential modelling parameters. Under the Open–Open condition, the terminal response was governed primarily by the asymmetry between the external continuation lengths. Operation of a single terminal surge arrester transferred the voltage maximum towards the opposite open terminal and could increase, rather than reduce, the maximum pipeline voltage. For the governing configuration, the LP maximum changed from 144 V_{rms} to 149 V_{rms} after the first operation and then decreased to 76 V_{rms} after both terminal arresters operated. The corresponding MP values were 116 V_{rms}, 121 V_{rms} and 62 V_{rms}. Bilateral arrester operation therefore reduced the governing maxima by approximately 49% relative to the intermediate state.

After arrester operation, the maximum voltages became only weakly dependent on the external continuation lengths and on the equivalent conducting-state resistance. Varying this resistance from 5 Ω to 15 Ω changed the final voltages by approximately 3.5%, although the terminal currents varied more significantly. The longitudinal surge arresters were not expected to operate, since their maximum voltage and current remained below the adopted operating and withstand limits.

The safety checks were satisfied under conservative assumptions. The highest MP-pipeline voltage obtained over all terminal configurations was 121 V_{rms}, below the CEI EN 50522 permissible touch voltage of 346 V_{rms}. Conductive coupling from the joint bay was verified separately using THOR50Hz. With two ECCs, the current injected through the local earthing system was 157.5 A_{rms}, compared with 208.6 A_{rms} for the one-ECC arrangement. At the conservative assessment distance of 10 m, the calculated soil potential was 221 V_{rms}, also below the permissible touch voltage. The actual minimum MP-pipeline distance is 13 m. Conductive coupling was therefore non-critical for the analysed configuration and was appropriately assessed separately from the inductive ATP-EMTP model.

The pipeline–earth solution was independently verified through the sectional model based on Appendix H of CIGRÉ Technical Brochure 95. Across the twelve comparisons involving both pipelines, three terminal configurations and two coating-admittance representations, the maximum absolute difference from ATP-EMTP was $0.290\ \mathrm{V_{RMS}}$, while the maximum normalised error was 0.240%. Including the coating conductance changed the maximum voltages by less than approximately 0.30%, confirming that its omission is acceptable for the investigated coating properties.

The analytical formulation also provides a practical advantage once the electrical-system current phasors have been determined. Pipeline discretisation and terminal conditions can be modified without reconstructing the complete coupled cable model, making the method suitable for rapid sensitivity analyses and more refined representation of non-uniform routes.

The results remain dependent on the available project data and modelling assumptions. The permanent network configuration was not analysed, and representative values were adopted for some pipeline, coating and terminal parameters. The soil was treated as homogeneous in the complete electromagnetic model, while surge-arrester operation was represented through successive steady-state conditions. The agreement between ATP-EMTP and the analytical model verifies the numerical implementation but does not constitute an experimental validation of the physical input data.

Future work should therefore focus on confirming the pipeline topology, coating properties, terminal devices, soil resistivity and earthing parameters through site data. Further developments may include analysis of the permanent network configuration, nonlinear time-domain modelling of the surge arresters, explicit representation of coating defects and comparison with field measurements.

Overall, the study demonstrates that interference in underground cable–pipeline corridors is governed mainly by the earth-fault return-current distribution and by the pipeline terminal conditions. The combined modelling procedure provides a consistent basis for identifying critical configurations, assessing mitigation measures and verifying the applicable safety criteria.

REFERENCES

[1] A. A. Hossam-Eldin and W. Mokhtar, “Electromagnetic interference between electrical power lines and neighboring pipelines,” in *Proc. 19th Int. Conf. Systems Engineering (ICSEng)*, Las Vegas, NV, USA, Aug. 2008, pp. 97–102.

[2] F. P. Dawalibi and R. D. Southey, “Analysis of electrical interference from power lines to gas pipelines—Part I: Computation methods,” *IEEE Trans. Power Deliv.*, vol. 4, no. 3, pp. 1840–1846, Jul. 1989.

[3] CIGRE Working Group 36.02, *Guide on the Influence of High Voltage AC Power Systems on Metallic Pipelines*, Technical Brochure 95. Paris, France: CIGRE, 1995.

[4] Comitato Elettrotecnico Italiano, *Effetti delle interferenze elettromagnetiche sulle tubazioni causate da sistemi di trazione elettrica ad alta tensione in corrente alternata e/o da sistemi di alimentazione ad alta tensione in corrente alternata*, CEI EN 50443. Milan, Italy: CEI, Dec. 2012.

[5] A. Ametani, T. Yoneda, Y. Baba, and N. Nagaoka, “An investigation of earth-return impedance between overhead and underground conductors and its approximation,” *IEEE Trans. Electromagn. Compat.*, vol. 51, no. 3, pp. 860–867, Aug. 2009.

[6] L. M. Wedepohl and D. J. Wilcox, “Transient analysis of underground power-transmission systems. System-model and wave-propagation characteristics,” *Proc. Inst. Electr. Eng.*, vol. 120, no. 2, pp. 253–260, 1973.

[7] International Telecommunication Union, *Management of Electromagnetic Interference on Telecommunication Systems due to Power Systems*, ITU-T Recommendation K.68. Geneva, Switzerland: ITU, Feb. 2006.

[8] Comitato Elettrotecnico Italiano, *Impianti di terra per impianti elettrici con tensione superiore a 1 kV in c.a.*, CEI EN 50522. Milan, Italy: CEI, Nov. 2022.

[9] G. C. Christoforidis, D. P. Labridis, and P. S. Dokopoulos, “A hybrid method for calculating the inductive interference caused by faulted power lines to nearby buried pipelines,” *IEEE Trans. Power Deliv.*, vol. 20, no. 2, pp. 1465–1473, Apr. 2005.

[10] R. Djekidel and D. Mahi, “Calculation and analysis of inductive coupling effects for HV transmission lines on aerial pipelines,” *Przegląd Elektrotechniczny*, vol. 90, no. 9, pp. 151–156, 2014.

[11] J. P. Nelson, “Power systems in close proximity to pipelines,” *IEEE Trans. Ind. Appl.*, vol. IA-22, no. 3, pp. 435–441, May 1986.

[12] A. Ametani, “A general formulation of impedance and admittance of cables,” *IEEE Trans. Power Appar. Syst.*, vol. PAS-99, no. 3, pp. 902–910, May 1980.

[13] M. M. Saied, “The capacitive coupling between EHV lines and nearby pipelines,” *IEEE Trans. Power Deliv.*, vol. 19, no. 3, pp. 1225–1231, Jul. 2004.

[14] R. Djekidel, D. Mahi, and A. Aissa, “Analysis of parameters affecting the capacitive interference between pipelines and power overhead line using genetic algorithms,” *Int. J. Electr. Eng. Inform.*, vol. 8, no. 2, pp. 315–330, Jun. 2016.

[15] R. Djekidel and D. Mahi, “Capacitive interferences modeling and optimization between HV power lines and aerial pipelines,” *Int. J. Electr. Comput. Eng.*, vol. 4, no. 4, pp. 486–497, Aug. 2014.

[16] C. A. Charalambous, A. Demetriou, A. L. Lazari, and A. I. Nikolaidis, “Effects of electromagnetic interference on underground pipelines caused by the operation of high voltage AC traction systems: The impact of harmonics,” *IEEE Trans. Power Deliv.*, vol. 33, no. 6, pp. 2664–2672, Dec. 2018.

[17] A. Gupta and M. J. Thomas, “Coupling of high voltage AC power line fields to metallic pipelines,” in *Proc. 9th Int. Conf. Electromagnetic Interference and Compatibility (INCEMIC)*, 2006.

[18] A. H. Al-Badi and H. M. Al-Rizzo, “Simulation of electromagnetic coupling on pipelines close to overhead transmission lines: A parametric study,” *J. Commun. Softw. Syst.*, vol. 1, no. 2, pp. 116–125, Dec. 2005.

[19] Y. Li, F. P. Dawalibi, and J. Ma, “Electromagnetic interference caused by a power system network and a neighboring pipeline,” in *Proc. 62nd Annual Meeting of the American Power Conference*, Chicago, IL, USA, Apr. 10–12, 2000, pp. 311–316.

[20] International Electrotechnical Commission, *Short-Circuit Currents in Three-Phase AC Systems—Part 3: Currents during Two Separate Simultaneous Line-to-Earth Short Circuits and Partial Short-Circuit Currents Flowing through Earth*, IEC 60909-3:2009. Geneva, Switzerland: IEC, 2009.

[21] L. Coelho, G. Sotelo, and A. C. S. Lima, “Detailed versus simplified representation of a pipeline for assessment of inductive and conductive couplings to an overhead transmission lines during steady-state and fault conditions,” *Int. J. Electr. Power Energy Syst.*, vol. 142, Art. no. 108350, Nov. 2022.

[22] F. Abaz, H. Bamalouk, and A. N. E. Ayad, “Study and simulation of the electric power cables degradation,” Master’s thesis, Université Kasdi Merbah Ouargla, Ouargla, Algeria, 2022.

[23] F. Ahmad, “Magnetic field management in underground cables,” Master’s thesis, King Fahd University of Petroleum and Minerals, 1996.

[24] I. O. Habiballah, A. S. Farag, M. M. Dawoud, and F. Ahmad, “Underground cable magnetic field simulation and management using new design configurations,” *Electr. Power Syst. Res.*, vol. 45, no. 2, pp. 141–148, May 1998.

[25] A. S. Farag, M. M. Dawoud, and I. O. Habiballah, “Implementation of shielding principles for magnetic field management of power cables,” *Electr. Power Syst. Res.*, vol. 48, no. 3, pp. 193–209, Jan. 1999.

[26] Terna Rete Italia S.p.A., “Relazione sulle situazioni di potenziale interferenza elettromagnetica con metanodotti e linee di telecomunicazione,” internal technical report, Italy, Oct. 28, 2020.

[27] Terna Rete Italia S.p.A., “Tavola per montaggio meccanico—Linee 220 kV semplice Terna, conduttore Ø 31,5 mm, sostegni tipo ‘N’,” unpublished internal document, Jun. 2012.

[28] Terna Rete Italia S.p.A., “Tavola per montaggio meccanico—Linee 132–150 kV semplice Terna a delta, conduttore Ø 31,50 mm, tiro pieno, sostegno tipo ‘N’,” unpublished internal document, Nov. 2023.

[29] Terna Rete Italia S.p.A., “Tavola per montaggio meccanico—Linee 380 kV semplice Terna, conduttore Ø 31,5 mm trinato, sostegni tipo ‘N’,” unpublished internal document, Jun. 2018.

[30] Terna Rete Italia S.p.A., “Tavola per montaggio meccanico—Strutture per linee elettriche ad alta tensione,” unpublished internal document, n.d.

[31] Terna Rete Italia S.p.A., “Tavola per montaggio meccanico—Linee 220 kV semplice Terna, conduttore Ø 31,5 mm, gruppi mensole per sostegni tipo ‘N’,” unpublished internal document, Jun. 2012.

[32] IEEE Power & Energy Society, *IEEE Guide for Planning and Designing Transition Facilities between Overhead and Underground Transmission Lines*, IEEE Std 1793-2012. New York, NY, USA: IEEE, 2012.

[33] CIGRE Task Force B1.26, *Earth Potential Rises in Specially Bonded Screen Systems*, Technical Brochure 347. Paris, France: CIGRE, 2008.

[34] ELEK Software, “Sheath bonding design guide for high voltage cables,” n.d.

[35] M. Dmitriev, “Screens grounding of 6–500 kV single-core cables: The distance from joints to link-boxes,” Voltplace, 2016.

[36] Brugg Cables, *High Voltage XLPE Cable Systems—Technical User Guide for 127–500 kV*, n.d.

[37] Terna Rete Italia S.p.A., “Interconnector frontiera Austria. Elettrodotto in cavo 220 kV Passo Resia–Val Venosta. Intervento B. Nuovo elettrodotto in cavo a 220 kV ‘S.E. Nauders–S.E. Glorenza’. Piano tecnico delle opere—Parte prima. Relazione tecnica illustrativa,” technical report, Italy, Dec. 5, 2014.

[38] Odra Energia S.r.l., “Progetto di fattibilità tecnico economica per la realizzazione del parco eolico offshore: ODRA—Relazione tecnica elettrodotto,” technical report, Milan, Italy, Oct. 15, 2023.

[39] S. Chinosi, *Sistemi terrestri ad Alta Tensione—Il progetto elettrico*. Prysmian Cables & Systems/Prysmian Italia, Italy, n.d.

[40] Terna S.p.A., “Tabella tecnica—Cavi unipolari isolati in XLPE per sistemi con tensione massima (U_m = 170) kV,” unpublished internal document, Dec. 2020.

[41] Terna S.p.A., “Tabella tecnica—Cavi unipolari isolati in XLPE per sistemi con tensione massima (U_m = 245) kV,” unpublished internal document, Sep. 2021.

[42] Terna S.p.A., “Tabella tecnica—Cavi unipolari isolati in XLPE per sistemi con tensione massima (U_m = 420) kV,” unpublished internal document, Aug. 2021.

[43] NKT, *High Voltage Cable Systems—Cables and Accessories up to 550 kV*, n.d.

[44] Comitato Elettrotecnico Italiano, *Impianti di produzione, trasmissione e distribuzione pubblica di energia elettrica—Linee in cavo*, CEI 11-17;CSV. Milan, Italy: CEI, Sep. 2025.

[45] Terna S.p.A.—Unificazione, “Typical trench cross-section for HV underground XLPE cable systems,” internal document, n.d.

[46] CIGRE Working Group C4.204, *Mitigation Techniques of Power-Frequency Magnetic Fields Originated from Electric Power Systems*, Technical Brochure 373. Paris, France: CIGRE, 2009.

[47] CIGRE Working Group B1.23, *Impact of EMF on Current Ratings and Cable Systems*, Technical Brochure 559. Paris, France: CIGRE, 2013.

[48] Comitato Elettrotecnico Italiano, *Protezione delle linee di telecomunicazione dagli effetti dell'induzione elettromagnetica provocata dalle linee elettriche vicine in caso di guasto*, CEI 103-6. Milan, Italy: CEI, Dec. 1997.

[49] Terna S.p.A., "HV underground-cable joint bay during installation," unpublished field photograph, Palermo, Italy, n.d.

[50] Prysmian Cables & Systems, "Cable-sheath link-box configurations," technical material, Milan, Italy, n.d.

[51] Terna Academy, "Training slides on HV cable sheath bonding and link-box configurations," unpublished internal training material, Rome, Italy, n.d.

[52] M. Riva, "Rete di trasporto del gas-metano di III^ specie tra Chiuro e Teglio (F.ne Tresenda). 1° lotto metanodotto DN 350 Chiuro-Tirano. 2.3 Descrizione lavori," Consorzio della Media Valtellina per il Trasporto del Gas, Sondrio, Italy, n.d.

[53] Snam S.p.A., "Metanodotto Sestino-Minerbio DN 1200 (48") DP 75 bar. Descrizione lavori. Lotto 1 Sestino–Badia Tedalda," technical report, Rome, Italy, Aug. 10, 2023.

[54] DEHN SE, "AC interference study and simulation," 2025.

[55] Snam Rete Gas S.p.A., "Analisi dell'interferenza elettromagnetica AC su gasdotti interrati in prossimità di linee elettriche ad alta tensione," unpublished technical report, Italy, n.d.

[56] Terna S.p.A., "Studio di interferenza elettromagnetica tra linee aeree di trasmissione a 380 kV e tubazioni metalliche interrate," unpublished technical report, Italy, n.d.

[57] Snam S.p.A., "Rifacimento metanodotto Livorno-Piombino DN 750 (30"), DP 75 bar e opere connesse. Descrizione lavori. Lotto 1 Collesalvetti–Cecina," technical report, Italy, Mar. 2024.

[58] A. Ametani, "Four-terminal parameter formulation of solving induced voltages and currents on a pipeline system," *IET Sci. Meas. Technol.*, vol. 2, no. 2, pp. 76–87, Mar. 2008.

[59] Snam Rete Gas S.p.A., "Caratteristiche tecniche della rete Snam Rete Gas—Rete Nazionale," San Donato Milanese, Italy, Jun. 30, 2021.

[60] S. McKelvey, D. Fingas, and R. Phillips, "Pipeline coating resistance estimation using influence from a CP rectifier," in Proc. AMPP Annual Conference + Expo, Nashville, TN, USA, Apr. 2025, Paper no. C2025-00347, pp. 1–15.

[61] International Telecommunication Union, Radiocommunication Sector, *World Atlas of Ground Conductivities*, ITU-R Recommendation P.832-3. Geneva, Switzerland: ITU, Feb. 2012.

[62] D. Antonelli, "Studio di impianti elettrici di protezione catodica nell'ambito del trasporto del gas metano in condotte metalliche interrate, sulla base di elementi normativi, norme, standards nazionali e internazionali," Bachelor's thesis, Università degli Studi di Padova, Padova, Italy, 2011.

[63] L. Paterlini, A. Marinelli, A. Brenna, and M. Ormellese, "Protection criteria of cathodically protected pipelines under AC interference," *Corros. Mater. Degrad.*, vol. 6, no. 1, p. 7, Feb. 2025.

[64] A. Junker Olesen, "AC corrosion of cathodically protected pipelines—A review," in *Proc. CEOCOR International Congress 2019*, Copenhagen, Denmark, May 2019, pp. 1–12.

[65] H. W. Dommel, *EMTP Theory Book*, ch. 5, "Underground cables." Vancouver, BC, Canada: Microtran Power System Analysis Corporation, 1992.

[66] Ministero dello Sviluppo Economico, "Regola tecnica per la progettazione, costruzione, collaudo, esercizio e sorveglianza delle opere e degli impianti di trasporto di gas naturale con densità non superiore a 0,8," Decreto 17 aprile 2008, *Gazzetta Ufficiale della Repubblica Italiana*, Serie Generale, no. 107, Suppl. Ordinario no. 115, May 8, 2008.

[67] Comitato Elettrotecnico Italiano, *Short-Circuit Currents in Three-Phase A.C. Systems—Part 0: Calculation of Currents*, CEI EN 60909-0 (CEI 11-25). Milan, Italy: CEI, Dec. 2016.

[68] UNI—Ente Italiano di Normazione, *Petroleum, Petrochemical and Natural Gas Industries—Cathodic Protection of Pipeline Systems—Part 1: On-Land Pipelines*, UNI EN ISO 15589-1:2017. Milan, Italy: UNI, 2017.

[69] UNI—Ente Italiano di Normazione, *General Principles of Cathodic Protection of Buried or Immersed Onshore Metallic Structures*, UNI EN 12954:2019. Milan, Italy: UNI, 2019.

[70] International Organization for Standardization, *Corrosion of Metals and Alloys—Determination of AC Corrosion—Protection Criteria*, ISO 18086:2019. Geneva, Switzerland: ISO, 2019.

[71] CIGRE/CIRED Joint Working Group C4.2.02, *AC Corrosion on Metallic Pipelines due to Interference from AC Power Lines: Phenomenon, Modelling and Countermeasures*, Technical Brochure 290. Paris, France: CIGRE, 2006.

[72] G. Lucca, “Electromagnetic interference from power lines on pipelines: Influence of pipe insulating coating degradation,” *Int. Trans. Electr. Energy Syst.*, vol. 26, no. 12, pp. 2699–2712, Dec. 2016.

[73] Terna S.p.A., “Relazione generale—Collegamento in cavo a 132 kV ‘CP La Pianta–SE Stagnoni’,” unpublished technical report, Rome, Italy, n.d.

[74] Comitato Elettrotecnico Italiano, *Electric Cables—Calculation of the Current Rating—Part 1-1: Current Rating Equations (100% Load Factor) and Calculation of Losses—General*, CEI 20-21/1-1. Milan, Italy: CEI, Oct. 2007.

[75] Terna S.p.A., “Correnti di corto circuito e tempo di eliminazione dei guasti negli impianti delle reti a tensione uguale o superiore a 120 kV,” Rome, Italy, Nov. 1, 2011.